energies

MDPI

Review

Mineral-Supported Photocatalysts: A Review of Materials, Mechanisms and Environmental Applications

Xue Li, Ulla Simon, Maged F. Bekheet * and Aleksander Gurlo *

Chair of Advanced Ceramic Materials, Institute of Material Science and Technology, Faculty III Process Sciences, Technische Universität Berlin, Straße des 17. Juni 135, 10623 Berlin, Germany; xue.li@ceramics.tu-berlin.de (X.L.); ulla.simon@ceramics.tu-berlin.de (U.S.)

* Correspondence: maged.bekheet@ceramics.tu-berlin.de (M.F.B.); gurlo@ceramics.tu-berlin.de (A.G.)

Abstract: Although they are of significant importance for environmental applications, the industrialization of photocatalytic techniques still faces many difficulties, and the most urgent concern is cost control. Natural minerals possess abundant chemical inertia and cost-efficiency, which is suitable for hybridizing with various effective photocatalysts. The use of natural minerals in photocatalytic systems can not only significantly decrease the pure photocatalyst dosage but can also produce a favorable synergistic effect between photocatalyst and mineral substrate. This review article discusses the current progress regarding the use of various mineral classes in photocatalytic applications. Owing to their unique structures, large surface area, and negatively charged surface, silicate minerals could enhance the adsorption capacity, reduce particle aggregation, and promote photogenerated electron-hole pair separation for hybrid photocatalysts. Moreover, controlling the morphology and structure properties of these materials could have a great influence on their light-harvesting ability and photocatalytic activity. Composed of silica and alumina or magnesia, some silicate minerals possess unique orderly organized porous or layered structures, which are proper templates to modify the photocatalyst framework. The non-silicate minerals (referred to carbonate and carbon-based minerals, sulfate, and sulfide minerals and other special minerals) can function not only as catalyst supports but also as photocatalysts after special modification due to their unique chemical formula and impurities. The dye-sensitized minerals, as another natural mineral application in photocatalysis, are proved to be superior photocatalysts for hydrogen evolution and wastewater treatment. This work aims to provide a complete research overview of the mineral-supported photocatalysts and summarizes the common synergistic effects between different mineral substrates and photocatalysts as well as to inspire more possibilities for natural mineral application in photocatalysis.

Keywords: photocatalysis; natural mineral support; synergistic effect; dye-sensitization

Citation: Li, X.; Simon, U.; Bekheet, M.F.; Gurlo, A. Mineral-Supported Photocatalysts: A Review of Materials, Mechanisms and Environmental Applications. *Energies* **2022**, *15*, 5607. https://doi.org/10.3390/en15155607

Academic Editors: Vincenzo Vaiano and Olga Sacco

Received: 30 June 2022
Accepted: 28 July 2022
Published: 2 August 2022

Publisher's Note: MDPI stays neutral with regard to jurisdictional claims in published maps and institutional affiliations.

Copyright: © 2022 by the authors. Licensee MDPI, Basel, Switzerland. This article is an open access article distributed under the terms and conditions of the Creative Commons Attribution (CC BY) license (https://creativecommons.org/licenses/by/4.0/).

1. Introduction

As environmental pollution issues have taken place more and more frequently in recent years, sustainable development has become the leading target of energy and environmental policy–making worldwide, determining the public concern for scientific research. Since the TiO_2-based water-splitting phenomenon was discovered by Fujishima and Honda in 1972, photocatalysis has stepped onto the solar energy conversion stage [1]. Many researchers have verified the extensive potential of TiO_2 in the photodegrading of different pollutants, such as bisphenol A [2], tetracycline [3], gaseous formaldehyde [4], S. aureus [5], etc. As a result, photocatalysis is widely regarded as the most promising route to solve both the energy and pollution crises. Several common photocatalysts have been found to possess excellent photocatalytic performance for the degradation of toxic dye and organic pollutants, including ZnO [6,7], In_2O_3 [8], g-C_3N_4 [9], BiOBr [10], etc.

However, large-scale industrial applications of pure photocatalysts often suffer several key issues: (1) small specific surface area and resultant poor adsorptive ability; (2) easy photo-generated electron-hole recombination and resultant low quantum efficiency; (3) difficult solid-liquid separation and photocatalyst recycling; and (4) high cost. For example, CdS has superior visible-light absorption and photocatalytic activity [11], while it suffers severe photo-corrosion issues and easily causes secondary pollution problems. Although TiO_2 has stable and superb photocatalytic performance, it is only UV-light responsive and hard to recycle [12]. Additionally, self-aggregation and high photogenerated electron-hole recombination rates are the other common issues that the purest photocatalysts encounter. Researchers have been trying many different modification strategies to address these problems. So far, several modification strategies have been developed to control the photocatalyst morphology and suppress photo-induced charge carrier recombination, including heterojunction design, noble-metal deposition, support composites, etc. [13–15]. Among these modification strategies, the support composite is the most promising method to overcome the photocatalyst recycling difficulty and thus realize the industrialization of photocatalysts. Common photocatalyst support materials are carbon nanotubes, mesoporous carbon, graphene graphite, zeolite, etc. While these carbon materials generally exhibit more regular morphology and better electrical properties, they are not the ideal support candidates for photocatalyst industrial development considering their cost and recycling issues. Natural minerals are generally defined as abundant natural resources on earth that are obtained directly from nature. Compared with other support materials, natural minerals are well known as suitable photocatalyst support candidates for the following reasons: (1) They are environmentally friendly, low cost, chemical resistant, mechanically stable, easily available, and do not cause secondary pollution to the environment; (2) natural minerals have the characteristics of a large specific surface area, providing more active centers and adsorbing pollutants to concentrate catalysis; (3) natural minerals are also excellent photocatalysts, such as ilmenite and pyrite, which play a good role in the degradation of water pollutants. More importantly, the combination of photocatalysts and natural minerals has become one of the most valuable modification strategies due to the vast availability and cost-effectiveness of natural minerals. Until now, many researchers have devoted enormous contributions to this field, as shown in Table 1.

Few reviews have been written about natural mineral supports. Liu et al. chose clay minerals and layered double hydroxides to study the synthesis methods of photocatalytic applications of various clay or LDH-based photocatalysts [16]. Szczepanik et al. found that clay/TiO_2 nanocomposites could achieve the photodegradation of several organic pollutants (organic dyes, herbicides, and aromatic aniline) through pseudo-first-order kinetics based on the Langmuir–Hinshelwood model [17]. Various synthesis methodologies of TiO_2/clay nanocomposites and the effects of clay support on the physical properties and photocatalytic activity of TiO_2/clay nanocomposites have been recently discussed [18]. In addition to synthetic strategy evolution, titanium/clay mineral composite applications in the environmental catalysis and photocatalysis fields were illustrated thoroughly by solid literature support [19]. Papoulis et al. elaborated on the application of halloysite-based nanocomposites in photodegrading inorganic air pollutants, volatile organic compounds, antibiotics, pesticides, azo dyes, and other organic pollutants [20]. More recently, Li et al. discussed the role of the three typical phyllosilicate minerals (kaolinite, montmorillonite, and rectorite) in improving the photocatalytic performance of several photocatalysts, such as TiO_2, g-C_3N_4, ZnO, and MoS_2 [21]. As one of the typical layered clay minerals, kaolinite was selected to analyze the preparation of common kaolinite-based photocatalysts and their environmental applications, such as gas and liquid phase pollutants and bacterial disinfection [22]. Photocatalytic mechanisms and kinetics were introduced in detail, as were kaolinite's structure and properties. Zou et al. focused on the aluminosilicate clay minerals in photocatalytic applications and divided them into type 1:1 and 2:1 aluminosilicate clay according to their specific layered structures [23]. Several typical 1:1 and 2:1 aluminosilicate clays, such as kaolinite and montmorillonite, were used to elucidate their

natural structure and surface activating and interlayered modification methods. However, they only focused on several specific clay minerals, failing to comprehensively overview and generalize valuable combination mechanisms between natural minerals and photocatalysts [24]. More recently, a review work came out to present the latest progress of natural minerals in the photocatalysis field based on their classification (silicate, oxide, sulfide, borate, and other minerals) [25]. However, the influence and reactive mechanisms of natural minerals in the photocatalyst–mineral composite system have not been completely covered in these review articles.

This paper represents a comprehensive review of natural mineral-supported photocatalysts. The purpose and contribution of this review are, first, to offer a comprehensive overview of mineral-supported photocatalysts development. We submitted the search query to the literature databases Web of Science (WOS) and Google Scholar in 2022. This work mainly focused on the research conducted in the last 15 years and initially selected 858 research papers. According to different research subjects of this literature, we categorize natural minerals into four groups: silicate minerals (799 papers, 93%), carbonate or carbon-based minerals (12 papers, 1%), sulfate or sulfide minerals (23 papers, 3%), and several special minerals (24 papers, 3%). As seen in Figure 1, natural silicate minerals are the main part that can be further classified into four groups according to their original mineral morphology, such as 1D (218 papers, 27%), 2D (309 papers, 39%), 3D (81 papers, 10%), and porous minerals (191 papers, 24%). Secondly, recent literature studies on the mineral application of photocatalysis are summarized; a brief introduction of photocatalyst modification methods and their merits are included in this work. Based on this, we summarize the recent research on each mineral application in photocatalysis. Thirdly, the key mechanisms for natural minerals to enhance photocatalytic properties are analyzed. We analyzed the modification mechanism based on its characteristics (i.e., morphology, chemical composition, light absorption ability, etc.). Fourth, the perspective of future work and research directions are mentioned.

Table 1. Photocatalysts prepared using different minerals as support materials.

Photocatalyst	Synthesis Method	Organic Pollutant	Light Source	Quantum Efficiency (%)	Refs.
Chrysotile/SnO_2	A direct precipitation process coupled with calcination treatment	MB	250 W 450 nm mercury lamp	99	[26]
Chrysotile @ZnO	Precipitation	MB	250 W 365 nm mercury lamp	99.50	[27]
TiO_2/micro-meso porous silica nanofibers	Sol-adhesion	RhB	25 W 254 nm ultraviolet light	95	[28]
Exfoliated kaolinite nanolayers	Intercalation and delamination	RhB	150 W 254 nm mercury lamp	over 95	[29]
g-C_3N_4/TiO_2/kaolinite	A mild sol-gel method associated with chemical stripping and self-assembly	CIP and S. aureus	500 W over 400 nm xenon lamp and 8 W fluorescent lamp	92	[5]
N-doped TiO_2/kaolinite	A modified two-step sol-gel method	CR	8 W lamp	99	[30]
Ti-Fe kaolinite composite	A simple precipitation method	Cr(VI)	300 W over 420 nm dysprosium lamp	87 at PH = 3.0	[31]
Ag/g-C_3N_4/kaolinite	A two-step assembly strategy by employing in situ impregnation-calcination and photo-deposition process	IBP	500 W over 400 nm xenon lamp	99.90	[32]
Kaolinite/TiO_2	Sol-gel method	MB	8 W 254 nm high-intensity UV-C radiation lamp	97	[33]
Mica/TiO_2/Fe_2O_3	A sol-gel assisted hydrothermal method	G-MeCHO	400 W xenon lamp	80	[34]
MoS_2/mica	Hydrothermal	TH	300 W xenon lamp	90.60	[35]
Ti-Fe-based alkaline muscovite	Impregnation	TBBPA	150 W xenon lamp	90	[36]
TiO_2/illite	Hydrothermal	MO	30 W UV light source	73.4	[37]
$KNbO_3$/vermiculite	In situ hydrothermal method	MB	300 W xenon lamp	81	[38]

AgI-Bi_2MoP_6/vermiculite	Sol-gel and precipitation methods	MG	65 W lamp	98.89	[39]
BiOBr/magnetic bentonite	In situ coprecipitation followed by microwave-assisted hydrothermal method	TC and CIP	500 W over 420 nm xenon lamp	85 and 95 for TC and CIP	[10]
Ag/AgCl/montmorillonite	Dispersion method	MB	100 W over 400 nm tungsten lamp	98	[40]
Calcite/TiO_2	Sol-gel method	TC	24 W 254 nm UV-lamp	90	[41]
ZnO-halloysite	Ultrasonic treatment	CIP	160 W mercury lamp	91	[42]
Fe(III)/montmorillonite	Simple adsorption	Cr(VI)	300 W xenon lamp	100	[43]
BiOBr/Ti_3C_2/exfoliated montmorillonite	In situ co-precipitation coupling with microwave hydrothermal	CIP	500 W over 400 nm xenon lamp	96	[44]
γ-Fe_2O_3/montmorillonite	Hydrothermal	RhB	40 W xenon lamp	99	[45]
CdS/MoS_2/montmorillonite	Direct coagulation casting	TC	50 W LED lamp	90.03	[46]
Coal-bearing strata aolinite/$MnFe_2O_4$	Hydrothermal	CTC•HCl	300 W over 420 nm xenon lamp	85.1	[47]
Cu_2O/ZnO/kaolinite	Co-precipitation	MB	150 W halogen lamp	93	[48]
ZnO-bentonite	Facile synthesis	MB and eriochrome black-T	Solar radiation	Over 95	[49]
ZnO/γ-Fe_2O_3/bentonite	Facile co-precipitation	CIP	Solar simulator	95	[50]

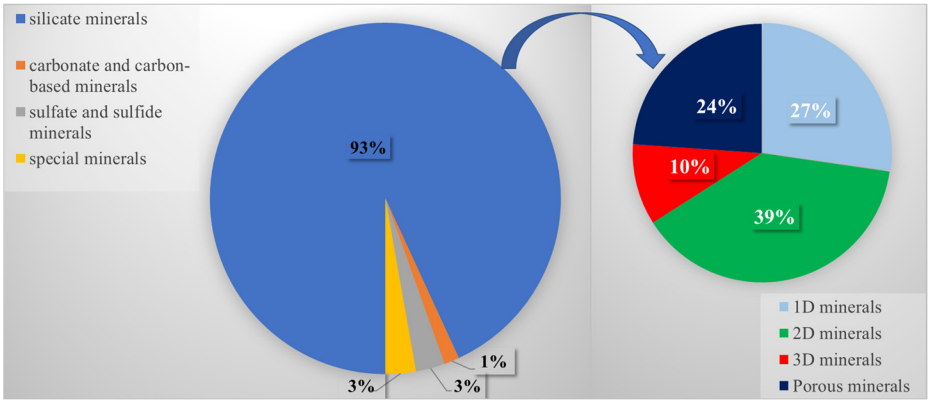

Figure 1. Representation of different natural minerals in photocatalysis.

2. Photocatalyst Modification Methods

Essentially, photocatalysis is a particular catalysis type involving light absorption by several specific active species [51]. For example, a novel inorganic–organic TiO_2-g-C_3N_4 composite could be excited under visible light ($\lambda \geq 400$ nm) irradiation, activating the electron (e^-) transfer from the valence band (VB) to the conduction band (CB) [52]. In this case, the photo-induced holes of TiO_2 could be attracted to the facet-coupled interface between TiO_2 and g-C_3N_4 due to the internal static electric fields of TiO_2, and then transferred to VB of g-C_3N_4, oxidizing RhB directly. Meanwhile, the photo-induced electrons of g-C_3N_4 transfer to TiO_2 due to the higher CB potential, reacting with the adsorbed O_2 into superoxide radicals ($\bullet O_2^{-1}$), as shown in Figure 2. However, the photocatalytic reaction can be easily prohibited due to fast photoexcited electron-hole recombination. In this part, TiO_2, as the most typical photocatalyst, is selected to present the common photocatalyst modification methods and their mechanism, including impurity doping, noble-metal deposition, alkali or alkaline earth modification, heterojunction design, and support combination.

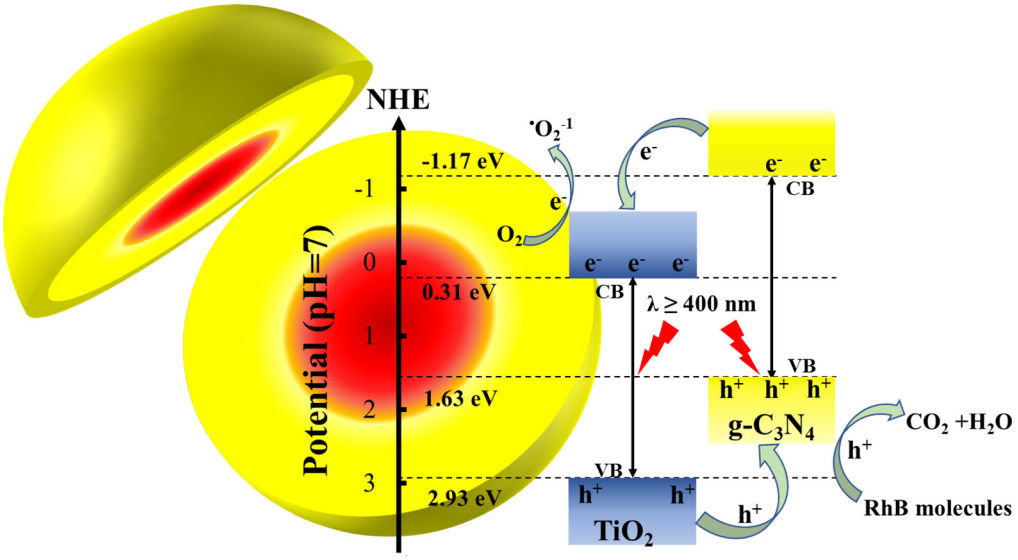

Figure 2. Photocatalytic mechanism scheme of TiO_2–g–C_3N_4 under visible light irradiation ($\lambda \geq 400$ nm).

2.1. Ion Doping

Doping is one of the most frequently applied methods to effectively extend the light absorption range of semiconductors via directly altering the bandgap structure [53]. Generally, TiO_2 photocatalysts could be doped with metal and non-metal dopants to enhance their photocatalytic activity [54–56]. For example, cobalt-doped TiO_2 samples synthesized via one-step hydrothermal method varied the cobalt dopant concentration from 0.1% to 3.0% to expand its optical response to the visible light region [57]. The photocatalytic phenol degradation reaction reached the highest degradation rate (81.72%) when the cobalt-doped amount was fixed at 0.3%. First principle calculation results indicate the density of the impurity state strengthens with increased dopant concentration, which is beneficial for the visible light absorption range extension and the enhancement of its photocatalytic efficiency. Additionally, the doped ions can also act as shallow traps to promote photoinduced electron-hole separation. However, when the doping concentration exceeds by too much, these doped ions are contrarily exchanged into photo-excited electron-hole recombination centers. Another work found that nitrogen ions could substitute the oxygen lattice of the TiO_2 matrix, therefore narrowing the band gap and shifting the absorption edge to the visible light region [58]. The BET surface areas of N–TiO_2 and N–TiO_2/C nanocomposite were calculated to be 101.4 and 131.6 m^2/g, higher than that of TiO_2 (87.7 m^2/g).

In order to process acidic gas pollution such as CO_2 and NO_x, special ions, namely alkali or alkaline earth metal ions, are incorporated into photocatalysts for better acidic gas adsorption capacity. For example, alkali (Na, K, Rb, and Cs) or alkaline earth metals (Mg, Ca, Sr, and Ba) were selected to modify anatase TiO_2 photocatalyst and investigate their effect on low-temperature NO_x trapping efficiency [59]. It was proved that the NO_x storage capacity is positively related to the amount of the modified metal species, and Cs-TiO_2 and Ba-TiO_2 have similar capacities (179 and 187 $\mu mol \cdot g^{-1}$, respectively), which is higher than that of conventional NO_x-trapping catalysts. According to in situ diffuse reflectance infrared Fourier transfer (DRIFT) spectra results, adsorbed NO_x species were trapped on the Ti sites of alkaline earth–doped TiO_2 and the alkali sites of alkali-doped TiO_2, while NO_x trapped on Ti sites was found to be more efficient than on other sites for its excellent photocatalytic oxidation ability.

2.2. Noble-Metal Deposition

Coupling with one or more noble metal nanoparticles, such as Pt, Au, Ag, and Pd, is another well-developed surface modification approach. First of all, the noble metal nanoparticles function as electron traps and realize the rapid electron migration from photocatalyst to metal nanoparticles through the Schottky barrier formed at the interface between the semiconductor and the noble metals. The surface plasma resonance properties of noble metals can promote photocatalyst excitation under visible light and thus facilitate interfacial electron transfer [60]. Furthermore, the Fermi levels of the noble metal nanoparticles are generally lower than the CB of TiO_2; therefore, the band gap structure could be modified. For instance, four noble metals (Pt, Pd, Ag, and Au) were loaded onto the TiO_2 surface, and it was found that photoactivity of the noble metal–deposited TiO_2 increased with the amount of noble metals [61]. Among these metals, 0.2 wt% Ag–deposited TiO_2 exhibited the highest phenol degradation rate (0.51 $\mu mol \cdot dm^{-3} \cdot min^{-1}$) under 60 min visible light irradiation, which is five times that of pure TiO_2. It is pointed out that Ag nanoparticles are deposited on the {101} crystal facet of anatase TiO_2 according to TEM analysis, which results in decreasing photoinduced electron-hole recombination and visible light absorption extension via acting as electron traps and the surface plasma resonance effect.

2.3. Heterojunction Design

Heterojunction construction is one of the most commonly applied and effective surface modification approaches, coming from the combination of two or more semiconductors with different VB and CB positions and the resultant narrower band gap structure. The referred heterojunction is the type-II heterojunction and could be classified into four types such as the conventional type-II heterojunction, P–N junction, surface heterojunction and direct Z-scheme heterojunction, depending on the charge carrier separation mechanism [62]. Generally, the photocatalytic activity of TiO_2 could be enhanced by designing a heterojunction structure with several oxides and non-oxide materials [63–65]. For example, g-C_3N_4/TiO_2 heterojunction composite was synthesized via the in situ hydrothermal method, and the obtained band gap energy was proved to be 2.8 eV compared with 3.0 eV of TiO_2 [66]. The g-C_3N_4/TiO_2 sample with a mass ratio of 1:4 exhibited the maximum hydrogen evolution rate (1041 μmol/(g·h)) under visible light irradiation, which could be attributed to the heterojunction formation and its spatial charge separation effect. The XPS valence spectra results confirm the interaction between g-C_3N_4 and TiO_2 as type-II heterojunction, and the mechanism for photocatalytic performance improvement is explained such that the electron migration from VB of g-C_3N_4 to CB of TiO_2 via C-O-Ti bonding can offer electrons more photocatalytic reaction time. TiO_2 is known as a typical n-type semiconductor and can be used to construct p–n heterojunctions by combining it with a p-type semiconductor. As a result, BiOI was selected to couple with TiO_2, and it was found that the 20% BiOI/TiO_2 heterostructure achieved the highest phenol conversion efficiency (13.5%) and the best selectivity (92.1%) [67]. The enhanced photocatalytic performance is ascribed to a narrower band gap and efficient photoinduced electron-hole separation due to the p–n heterojunction structure as well as more exposed reactive facets.

2.4. Support Material Combination

Over the past decade, loading the well-developed photocatalysts onto special supporting materials with unique chemical properties or morphology has become more popular. Compared with photocatalyst modification methods such as ion doping, support material combinations have different characteristics in promoting photocatalysts. Support material generally only influences the photocatalytic reaction rate instead of the reaction process. On the one hand, when deposited onto the surface of minerals, the aggregation of photocatalysts could be greatly meliorated, which considerably decreases the chance of

photo-generated electron-hole recombination [68,69]. For example, the addition of reduced graphene oxide into the titanium oxide matrix could hinder the agglomeration of photocatalyst nanoparticles and efficiently promote photoinduced electron-hole immigration [70]. On the other hand, the combination of minerals and photocatalysts could obtain better adsorptive ability, which is favorable for the concentration of pollutants near the photocatalysts and shortens the transfer route of photo-induced charge carriers. With high specific surface area and porosity, porous diatomite could cooperate with silver phosphate to harvest visible light and adsorb dye molecules [71]. In many cases, minerals have some active species that function differently in photocatalytic reaction systems. Some active species in minerals could be combined with photocatalysts and modify the crystalline and electronic structure of photocatalysts, similar to the mechanism of ion doping and heterojunction construction. While other active species could act as the separation center of photo-induced electron and hole pairs and vary the transfer route of the charge carriers. The most promising directions in recent decades are more postulates of mineral support influences and further elucidations of the known influences.

Generally, support materials are mainly divided into natural minerals and artificial minerals. Increasing research on mineral-supported photocatalysts has found that the natural minerals as photocatalyst supports could effectively achieve fast photocatalyst collection and recycling at a relatively low-cost level [21]. The natural minerals as supporting materials are introduced into the photocatalysis system to mainly improve the durability of photocatalysts and decrease the application cost, which could enable the industrialization of photocatalysts. For artificial minerals, there are few reports about them as photocatalyst support. Some studies have pointed out that although it is possible to synthesize specific minerals with better morphology and the same chemical composition in the lab, the cost and time of large-scale production is much higher than using natural minerals due to the strict method of laboratory mineral synthesis. Here, we focus on natural minerals. We take a more detailed look at the four natural mineral groups (silicate minerals, carbonate or carbon-based minerals, sulfate or sulfide minerals, and several special minerals) mentioned in the Introduction section.

3. Natural Silicate Mineral-Supported Photocatalyst

As the main part of natural minerals, silicate minerals have numerous members and abundant reserves. Many efforts have been devoted to exploring suitable clay supports to prepare photocatalyst-supported composites, mainly because of their specific structure, high surface area, and multiscale porosity, including the resultant adsorption properties and ability to be bound to reactive groups. It is promising to disperse photocatalyst particles onto the clay minerals under mild reaction conditions to deal with the universal aggregation problems.

According to the literature, natural clay minerals can be divided into four general types (porous, 1D, 2D, and 3D minerals).

3.1. 1D Mineral-Supported Photocatalyst

3.1.1. Attapulgite-Supported Photocatalyst

As a typical clay soil, attapulgite (ATP) is magnesium aluminium phyllosilicate with special lath or rod-like morphology that is abundant in Jiangsu Province, China. It is characterized as a porous crystalline structure containing tetrahedral layers arranged together along longitudinal sideline chains [72]. Due to its large specific surface area, substantial intrinsic nano-channels, and porous structure, attapulgite has rich hydroxyl groups on its surface and could incorporate many active species and transient metal ions to construct functionalized nanocomposites with superior adsorption ability [73].

Considering its high specific surface area and thermal and chemical stability, attapulgite is regarded as suitable support to compensate for catalyst selectivity and stability deficiency under different photocatalytic conditions. For instance, Bi_2MoO_6 deposited on

attapulgite support by a simple solvothermal method showed an improved photocatalytic oxidation rate of tetracycline (0.0109 min^{-1}) under visible light irradiation, which was about 1.70 times higher than that of pure Bi_2MoO_6 (0.00626 min^{-1}) [74]. The high specific surface area of attapulgite (216.4 m^2/g) was considered to speed up the adsorption and photocatalytic process, resulting in a better photocatalytic performance of the Bi_2MoO_6/attapulgite composite.

Although its superior visible light-responsive ability, g-C_3N_4 suffers serious agglomeration problems, which affect its photocatalytic performance. Many efforts have been dedicated to controlling its morphology and structure to improve its photocatalytic activity. Zhu et al. prepared a novel magnetic Fe_3O_4 quantum dots@g-C_3N_4/attapulgite (ATP) applying a eutectic method followed by water bath deposition [75]. The specific surface area was enhanced from 45.1 m^2/g to 60.9 m^2/g after g-C_3N_4 loading due to the formation of rich interior space between attapulgite and the g-C_3N_4 matrix, as shown in Figure 3a. Furthermore, the decay lifetime of Fe_3O_4 quantum dots@ g-C_3N_4/attapulgite ternary composite reached 7.1 ns, which was longer than that of g-C_3N_4/ATP (4.3 ns) and g-C_3N_4 (3.1 ns), confirming that attapulgite and Fe_3O_4 quantum dots in the intercalation structure could effectively promote the separation of photogenerated electron-hole pairs. The later Fe_3O_4@g-C_3N_4/attapulgite photocatalyst could degrade 90.6% of 20 mg/L 2-Mercaptobenzothiazole under 90 min visible light irradiation. Moreover, magnetic Fe_3O_4 particles in the composite could provide efficient magnetic separation of the photocatalyst after the photocatalytic experiments. Zuo et al. prepared attapulgite/Cu_2O/Cu/g-C_3N_4 with unique Z-scheme heterostructure through in situ reduction of ultra-fine CuO nanoparticles on the surface of rod-like attapulgite under NH_3 gas during melamine polycondensation [76]. The obtained photocatalyst exhibited a high BET surface area (79.5 m^2/g) and band gap energy of 1.9 eV, significantly improving the separation and immigration of photogenerated electron-hole pairs. This attapulgite/Cu_2O/Cu/g-C_3N_4 composited showed a higher degradation rate of chloramphenicol antibiotic (61%) under visible light irradiation for 120 min than that determined for attapulgite/g-C_3N_4 composite.

Recently, some photocatalysts have been successfully assembled onto the attapulgite surface for CO_2 reduction [77,78]. For instance, CeO_2/attapulgite composite showed CO and CH_4 yields of about 3 and 3.6 times higher than that of pure CeO_2, respectively, and the photocurrent intensity of CeO_2/attapulgite is nearly 2.2 times higher than that of the bare CeO_2 photocatalyst [77]. Adding In_2O_3 to the later composite to obtain In_2O_3/CeO_2/attapulgite ternary hybrid system exhibited even better CO and CH_4 yields, which are 6.11-fold and 6.78-fold higher than that of pure CeO_2 [78]. It is supposed that the introduction of attapulgite into binary or ternary hybrid systems can restrain the accumulation of CeO_2 and In_2O_3 particles and provide a large surface area with abundant active sites. Similarly, CeO_2/g-C_3N_4-hybrid photocatalyst deposited on attapulgite skeleton showed excellent electron immigration capability with the high adsorptive capacity of attapulgite matrix, and it was synergistically beneficial for the photocatalytic desulfurization [79]. However, an excessive attapulgite amount in the composite would minimize the light transmission and thus influence its photocatalytic activity.

Noble metals have many vital applications in the catalysis field, but it is unrealistic to put them into mass production due to the high cost. As a result, attapulgite can be used for photocatalyst support to reduce the usage amount of noble metals. Ma et al. could successfully distribute Ag_3PO_4 nanoparticles on attapulgite surface without apparent spherical particle aggregation [80]. With the improved adsorptive ability and stability, the silver content of Ag_3PO_4/attapulgite decreased from 77.3% to 18.87%. This work solidifies the possibility of reducing the cost of noble metal catalysis in practical production without reducing their photocatalytic performance.

Furthermore, the surface modification of attapulgite with hydrochloric acid could exhibit significantly improved water splitting ability in the presence of photosensitizers such as Eosin Y dye (EY) [81]. The treatment of attapulgite with relatively low concentra-

tion HCl solution (1 mol·L) and the use of EY-sensitizer yielded a maximal hydrogen generation rate of 210 μmol·h^{-1} with evident 28.6% quantum efficiency at 490 nm under visible light illumination [82]. It is proposed that electrons excited from sensitizer molecules adsorbed on the attapulgite surface could immigrate to attapulgite efficiently and therefore enhance the photocatalytic performance remarkably, as the process presented in Figure 3b.

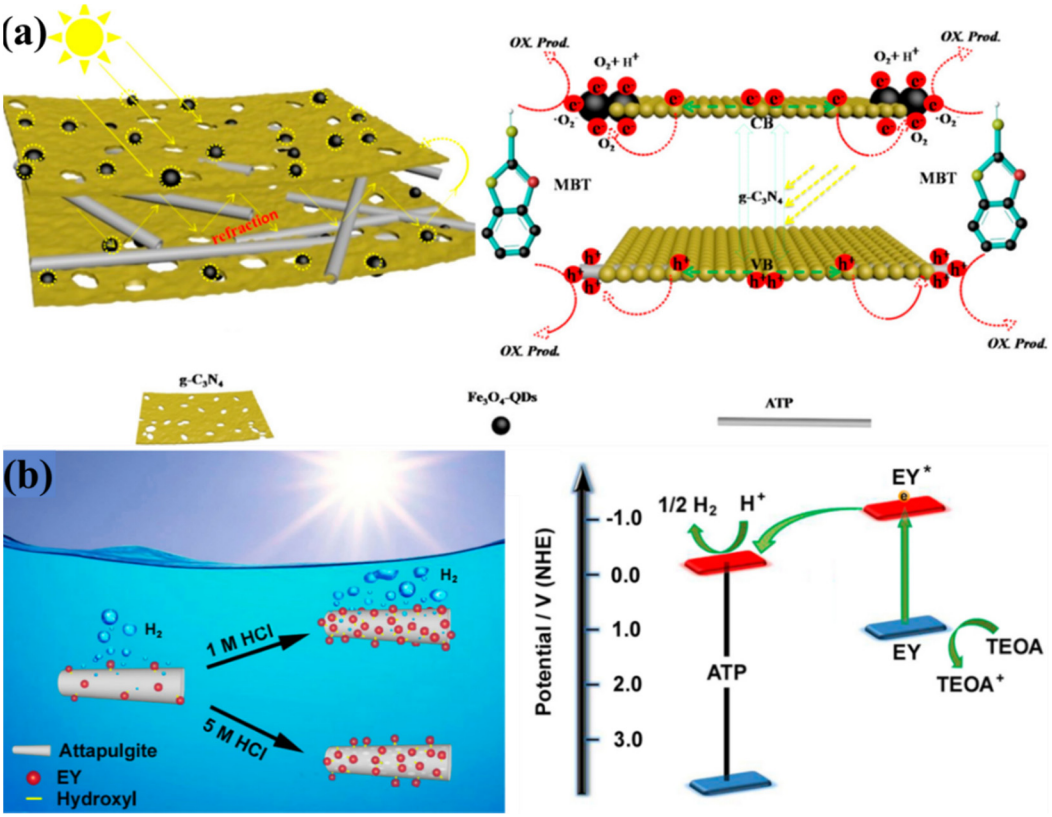

Figure 3. (**a**) Diagram of Fe_3O_4-QDs@g-C_3N_4/ATP and the mechanism for degradation of 2-mercaptobenzothiazole (MBT) under visible light irradiation; (**b**) schematic illustration of charge separation and transfer over EY-ATP photocatalysts and interface modified strategy of ATP we proposed under visible light ($\lambda \geq 420$ nm). Adapted with permission from Ref. [75]. Copyright 2017, American Chemical Society; Adapted with permission from Ref. [81]. Copyright 2016, American Chemical Society.

3.1.2. Palygorskite-Supported Photocatalyst

Similar to attapulgite, palygorskite is also a fibrous hydrated magnesium aluminum phyllosilicate with rich reactive hydroxyl species on the surface. It possesses a chain-lamellar structure composed of two silica tetrahedral sheets linked by a magnesium or aluminum octahedral sheet, where the mismatch between the tetrahedral and octahedral sheets induced non-inter-connected zeolite-like channels. Apart from fibrous morphology, high specific surface area and moderate cation exchange capacity, palygorskite has a negatively charged surface that could exert electrostatic attraction to adsorb cations [83].

Based on the aforementioned advantages, natural palygorskite clay has been used as a unique fibrous substrate for various photocatalysts. For instance, the nanometric size of TiO_2 particles immobilized on the palygorskite surface could prevent sintering-induced growth from exceeding the nucleus critical size required for the anatase–rutile phase transition [84]. E. Stathatos et al. prepared a porous TiO_2/palygorskite composite by applying nonionic surfactant molecules as a pore directing agent that could be removed by thermal treatment to generate the porosities in the composite [85]. The latter approach resulted in a homogeneous dispersion of TiO_2 on the surface of the palygorskite nanofibers with an

average crystallite size of 12–16 nm. Kuang et al. fabricated an Ag-deposited TiO_2/palygorskite composite via a solvothermal-chemical reduction route [86]. The optimized ternary Ag-TiO_2/palygorskite composite could degrade 95.27% of methylene blue under visible light illumination after 210 min compared with 54.11% of TiO_2/palygorskite and 9.85% of commercial TiO_2 after the same time. It is suggested that the improved photocatalytic activity of the composite under visible light was attributed to the positive synergistic effect between palygorskite support and TiO_2, including large specific surface area, evenly distribution, and more adsorption sites as well as the surface plasmon resonance effect of Ag ions responsible for efficient photogenerated electron-hole pair separation. Additionally, Zhang et al. revealed that the inorganic nanonetwork of palygorskite could be modified from rigid nanorods to multiporous structures and then combined with graphitic carbon nitride, resulting in superior photocatalytic activity for Cr(VI) reduction and methylene blue degradation under visible light [87]. The g-C_3N_4/palygorskite composite exhibited removal efficiency of 99.5% of Cr (VI) and 99.2% of MB after 100 min compared with about 14% and 10%, respectively, removed by pure g-C_3N_4. This remarkable improvement in photoactivity could be ascribed to the adsorption ability of the palygorskite matrix and the porous nanonetwork, including the macroporous structure of the as-synthesized composite that is beneficial for preventing the charge carrier recombination.

As a novel p-type bismuth-based semiconductor, bismuth oxyiodide has a suitable band gap and high stability and is available for application in the hydrogen generation and environmental purification fields. Luo et al. have recently assembled 3D flower-like palygorskite/bismuth oxyiodide composites via intercalating natural palygorskite clay into the microspheres [88]. The as-prepared composite was composed of two bismuth oxyiodide phases, Bi_5O_7I and $Bi_4O_5I_2$, loaded on a palygorskite surface, and it exhibited higher photoactivity with 88% greater degradation efficiency of tetracycline hydrochloride than that of pure $Bi_4O_5I_2$ (64%) and Bi_5O_7I (59%). This improvement in photocatalytic performance was mainly ascribed to the enlarged specific surface area of palygorskite, the evident absorption shift from UV to visible light, and the raised photogenerated charge carrier density due to type II heterojunction formation between $Bi_4O_5I_2$ and Bi_5O_7I. Owing to the remarkable effect in upconverting photoluminescent properties of rare-earth ions, He et al. have more recently investigated the doping effect of Yb^{3+} and Tm^{3+} in LaF_3 matrix and the hosting effect of acid-modified palygorskite [89]. On the one hand, they found that Yb^{3+} ions acted as the sensitizer for near-infrared light as energy source transfer to acceptor ions, while the Tm^{3+} ions acted as an activator in the co-doping system of Yb^{3+}, upconverting near-infrared light into UV and visible light and realizing full spectrum utilization. On the other hand, the acid treatment of the palygorskite skeleton resulted in a large specific surface area, abundant adsorption sites, and shortened band gap, facilitating rare-earth fluoride particle immobilization and constructing an indirect Z-scheme heterostructure. The formed Z-scheme heterostructure mediated by defective fluorine vacancy favors the separation of electron-hole pairs, preserves high reduction–oxidation potentials, and provides rich active sites beneficial for photocatalytic N_2 fixation. In the long run, the recycling problem of catalysts has become a common concern in the practical application of various catalysts. Yuan et al. revealed that Fe-octacarboxylic acid phthalocyanine supported on palygorskite/Fe_3O_4 nano-composites by the ultrasonic method presented high photocatalytic performance and could be magnetically recycled in an external magnetic field [90].

Furthermore, natural palygorskite could also be used to fabricate Maya blue-like organic–inorganic hybrids as photocatalyst. For instance, Zhang et al. prepared a novel photocatalyst hybrid in which palygorskite clay acted as a matrix, Eosin Y dye as photosensitizer, and triethanolamine as a sacrificial agent [91]. The hydrogen evolution rate of the optimal Eosin Y–sensitized palygorskite is approximately 3247.2 μmol/h under visible light irradiation, which is over 12 times better than that of the counterpart without

palygorskite. It was postulated that a negatively charged palygorskite surface could provide a driving force to control the photosensitized electron-transfer reaction via electrostatic attraction.

3.1.3. Halloysite-Supported Photocatalyst

As one kind of hydrothermal alteration or surface weathering of phyllosilicate minerals and a rare derivative of kaolin, halloysite is a two-layered clay mineral with a nanotubular structure formed by rolling layers composed of silica tetrahedral sheets as the outer surface and alumina octahedral sheets as the inner surface [92]. With the empirical chemical formula $Al_2Si_2O_5(OH)_4$ and a well-defined inherent hollow tubular framework, halloysite nanotubes have a positive octahedral Al–OH array on the internal surface and negative Si–O–Si groups on the external surface, facilitating the functionalization of their surface and composite fabrication, and compared with carbon nanotubes, natural halloysite is an environmentally benign, economically available, and highly stable with a large specific surface area with sufficient hydroxyl groups, making it a promising raw material in many application fields.

Halloysite nanotubes were commonly applied as photocatalyst support owing to their unique tubular network and superior adsorptive ability. For instance, Wang et al. prepared homogeneously dispersed TiO_2 particles on halloysite nanotubes (HNTs) via a one-step solvothermal method for photocatalytic application [93]. The as-synthesized TiO_2/HNTs composite showed pH sensibility during the methanol degradation process, and the CO_2 evolution rate reached about 1744.31 ± 7.63 $\mu mol \cdot h^{-1} \cdot g^{-1}$, which is much higher than that determined for pure TiO_2 (1053.12 ± 7.23 $\mu mol \cdot h^{-1} \cdot g^{-1}$) under the same reaction conditions. This superior photocatalytic performance was explained by the excellent adsorptive capacity of halloysite, enhancing the crystallization degree of TiO_2 and inhibiting TiO_2 agglomeration. As presented in Figure 4 b and c, the TiO_2 particles were distributed onto the tubular structure of HNTs. Based on the TiO_2/HNTs photocatalytic system, some modification methods have been applied to further improve photocatalytic activity. For example, Yu et al. investigated the modification of TiO_2/halloysite with several rare-earth metal ions as well as conductive polymers via the ion imprinting technique, and as a result, the Y-TiO_2/halloysite-Poly-o-phenylenediamine (POPD) composite exhibited high photodegradation efficiency (78.8%) of tetracycline [94]. The modification of natural halloysite by acid treatment and then loaded TiO_2 and Fe_2O_3 could also lead to high photocatalytic degradation of aniline and chloro-anilines due to the large surface area and homogeneous particle distribution on the composites [95]. Additionally, the loading of the TiO_2 photocatalyst on the surface of two different tubular halloysite clays, which originated from Limnos Island and Utah, via hydrothermal treatment resulted in slight differences between the two halloysite-supported TiO_2 photocatalysts due to the difference in the surface characteristics of halloysite clays [96].

In recent years, heterojunction construction has received more attention in the photocatalysis field, and therefore more work is concentrated on fabricating novel hierarchical ternary hybrid photocatalysts, including g-C_3N_4/TiO_2, g-C_3N_4/ZnO, CeO_2/AgBr, etc. For instance, ternary $Ni(OH)_2$@g-C_3N_4/halloysite composites with considerably improved photocatalytic activity could be synthesized from porous g-C_3N_4 that could accommodate $Ni(OH)_2$ nanoparticles, while abundant hydroxyl groups and Si–O groups present on the halloysite surface strongly interacted with nickel ions, resulting in high particle dispersion [97]. The latter study showed that 1wt% $Ni(OH)_2$@g-C_3N_4/halloysite exhibited a higher photocatalytic hydrogen evolution rate (18.42 $\mu mol \cdot h^{-1}$) in comparison with that of $Ni(OH)_2$@g-C_3N_4 (9.12 $\mu mol \cdot h^{-1}$), which was explained by the negatively charged surface of halloysite that efficiently traps photogenerated holes, decreases the electron-hole recombination rate, and prolongs the electron lifetime. Similarly, g-C_3N_4/TiO_2/halloysite heterojunction, prepared via the sol-gel and calcination method, possessed a decreased band gap of 2.5 eV attributed to the interfacial synergistic interaction between halloysites

and semiconductors and more efficient separation of photogenerated charge carriers [98]. As shown in Figure 4d, the TiO_2 nanoparticles were firmly attached to the halloysite surface and then evenly inserted into the interlayer space of g-C_3N_4. At the interface of the ternary components, a heterojunction structure is formed by band gap overlapping. Furthermore, Pt–Cu bimetallic nanoparticles have been loaded on the halloysite surface by trapping negative species $[PtCl_6]^{2-}$ inside the halloysite and complexing Cu(II) electrostatically with Pt(IV) to realize photocatalytic performance improvement [99]. The existence of the active species $[PtCl_6]^{2-}$ could help Cu ions to enter the channels of natural halloysite nanotubes via the formation of the heterometallic double complex between Cu(II) cations and Pt(IV) anions. Additionally, the special tubular structure of natural halloysite can protect Pt–Cu bimetallic nanoparticles from size alteration after heat treatment.

By virtue of its unique structure and characteristic surface chemistry, halloysite could be used to modify semiconductor arrangement and structure. For example, MnO_2 nanocomposites could be prepared and placed onto the surface of the hierarchical flower-like architecture of natural halloysite [100]. Xu et al. creatively designed a core-shell fluorescence Ag/HNTs composite by selectively modifying the external tubular walls of halloysite with citrate–europium (Cit-Eu) complex and firmly attaching Ag nanoparticles into the interior surface of natural halloysite nanotubes to achieve the efficient degradation and ultrasensitive detection of tetracycline (TC), as depicted in Figure 4a. It is asserted that these thick halloysite tubular walls can provide natural defense and promote metal-enhanced fluorescence effects, subsequently accelerating TC detection efficiency, while the attached Ag nanoparticles can induce the faster separation of photoexcited electrons and holes and thereby enhancing its photocatalytic activity [101]. It is worthy to note that a novel hybrid photocatalyst, fabricated by incorporating Rose Bengal dye into the halloysite matrix, showed improved photodecomposition ability with zero-order kinetics in the 4-n-nonylphenol photooxidation process [102]. The latter hybrid composite could efficiently adsorb hydrophobic compounds and promote singlet oxygen production.

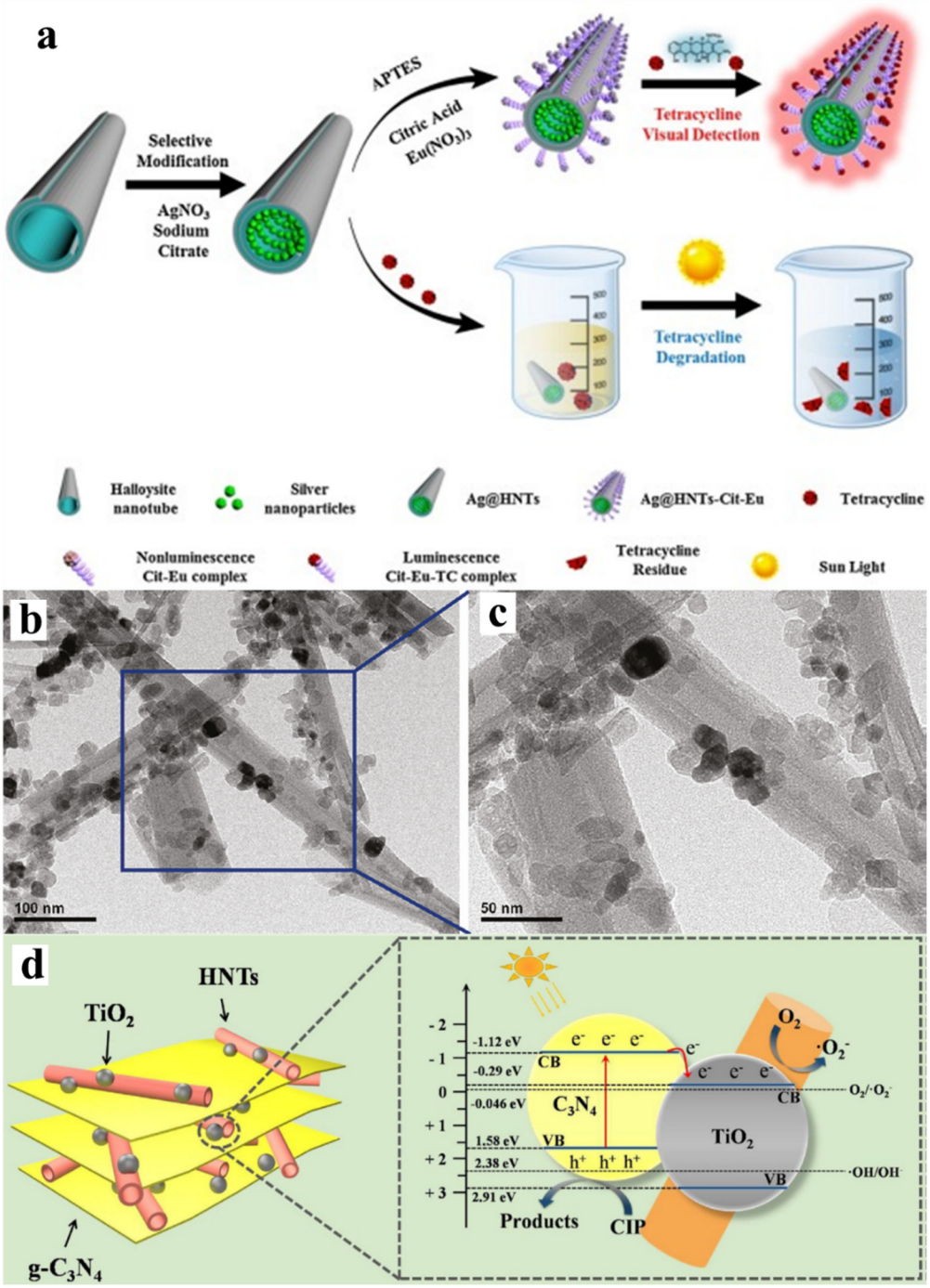

Figure 4. (**a**) Fabrication strategy of the Ag@HNTs−Cit−Eu nanocomposite and the detection and degradation of tetracycline (TC); (**b**) TEM and (**c**) corresponding magnified TEM images of TiO_2/HNTs; (**d**) schematic of a possible mechanism for photodegradation of ciprofloxacin (CIP) over g−C_3N_4/TiO_2/HNTs heterojunction composites. Adapted with permission from Ref. [93]. Copyright 2011, American Chemical Society; Adapted with permission from Ref. [98]. Copyright 2018, Elsevier B.V; Adapted with permission from Ref. [101]. Copyright 2019, Elsevier B.V.

3.1.4. Sepiolite-Supported Photocatalyst

As a typical hydrated magnesium silicate in the phyllosilicate mineral group, sepiolite consists of alternating blocks and intracrystalline channels that crystallize in the direction of fibers belonging to a chain-type clay. Each structural block is constructed by an octahedral magnesium sheet intercalating between two tetrahedral silica layers. Differing from other 2:1 type silicate clays, discontinuity of the octahedral silica sheets leads to the

formation of structural channels and tunnels. Owing to the peculiar pore structure with interior zeolite-like channels, natural fibrous sepiolite has a high specific surface area and strong adsorption ability [103]. Therefore, sepiolite has been widely applied in the catalysis and environmental purification fields.

Considering its abundance and low cost, Karamanis et al. deposited TiO_2 onto sepiolite to construct a multi-functional photo-responsive catalyst for building applications [104]. In this TiO_2/sepiolite nanocomposite, TiO_2 provides certain photocatalytic activity for pollutant degradation, while natural sepiolite, as adsorbent, retains hydrophilicity even in the presence of hydrophobic TiO_2. TiO_2/sepiolite nanocomposite possesses type II adsorption isotherm and achieves the maximum water vapor adsorption capacity of 30% at 93.6% relative humidity. Papoulis et al. recently modified natural sepiolite by substituting first the exchangeable cations with Zn and Cu ions and then incorporating anatase TiO_2 particles into the composite [105]. They found that Zn-exchanged sepiolite-based nanocomposites could exhibit high photocatalytic performance for NO_x gas oxidation. The difference in photoactivity was explained by the synergistic effect of porous sepiolite support and the ZnO formation in the anatase TiO_2 matrix. In order to eliminate the volatile organic compounds in the air, Hu et al. more recently prepared BiOCl/TiO_2/sepiolite (T-B-S-500D) heterogeneous ternary photocatalyst via a facile hydrolysis–precipitation method followed by the calcination and crystallization processes [106]. The photocatalytic activity of the as-prepared composites was evaluated by the decomposition rate of gaseous formaldehyde according to the Langmuir–Hinshelwood model. The BiOCl/TiO_2/sepiolite composite calcined at 500 °C showed a high reaction rate constant of 0.00728 min^{-1} under visible light, which is approximately 6.62 and 7.43 times higher than that of TiO_2 and BiOCl, respectively, under the same conditions. They suggested that sepiolite in the composite functions as a superior adsorbent to capture and enrich the pollutant concentration near the photocatalyst surface, and the synergistic effect between sepiolite and formed BiOCl–TiO_2 heterojunction enhances the light-responsive ability as well as the separation efficiency of electron-hole pairs as the reaction route, as shown in Figure 5a. Moreover, a hollow PVP/sepiolite/BiOBr hierarchical microsphere, synthesized from acidized sepiolite (AS) and polyvinyl pyrrolidone (PVP) as the treatments, shown in Figure 5b, could possess slightly improved photodegradation efficiency of diclofenac sodium (80%) under visible light irradiation [107]. The increased activity of PVP/sepiolite/BiOBr composite was explained by the unique hollow network, as presented in Figure 5c,d, which improved visible light absorption and efficient charge carrier separation. Acid treatment of sepiolite could also enhance the dispersion of Cu and Cu_2O photocatalysts in the ternary sepiolite/Cu_2O/Cu composite, leading to a redshift of the band gap and enhancing the visible light utilization as well as Cu ions functioning as electron mediator [108]. This composite showed superior photodegradation efficiency of Congo Red dye with approximately 95.1%, which is much higher than that determined for Cu_2O/Cu (71.2%). Anchoring ZnO/Fe_3O_4 dual nanoparticles onto surfactant-modified sepiolite surfaces could not only improve the photocatalytic removal efficiency of ZnO/Fe_3O_4-sepiolite composite for the degradation of pharmaceuticals and organic dyes but also solve its recycling problems [109,110]. Other than enlarged surface area and improved adsorption ability, the ZnO/Fe_3O_4/sepiolite composite exhibits a superparamagnetic property and thus can be easily recovered.

Furthermore, photosensitized sepiolite could be applied for the photodegradation of several organic dyes. Owing to its negatively charged surface, sepiolite is characterized as having an obviously higher adsorption capacity of cationic dyes, such as Rhodamine B, than of anionic dyes, such as trypan blue [111]. The spent sepiolite after Rhodamine B could be reused to degrade trypan blue under visible light illumination, and its photocatalytic performance of trypan blue degradation increases to approximately twice as much as the original sepiolite. These works solidify a compromising route to realize multiple applications of natural sepiolite in a low-cost and environmentally benign method.

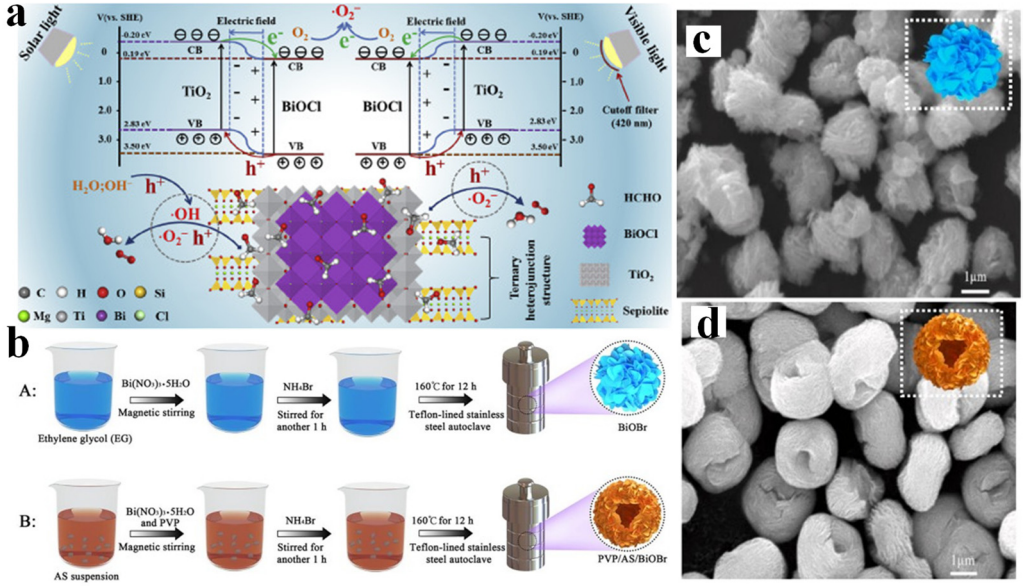

Figure 5. (**a**) Possible mechanisms for photocatalytic removal process of formaldehyde (HCHO) under solar and visible light irradiation on the BiOCl/TiO_2/sepiolite (T–B–S–500D) composite; (**b**) schematic illustration of the synthesis pathway and the structure schematic model of the composites; SEM images of (**c**) pure BiOBr and (**d**) PVP/AS/BiOBr (6%). Adapted with permission from Ref. [106]. Copyright 2019, Elsevier Ltd; Adapted with permission from Ref. [107]. Copyright 2019, Elsevier B.V.

3.1.5. Imogolite-Supported Photocatalyst

As a naturally occurring weathered volcanic glassy ash soil, imogolite is a kind of hydrous aluminosilicate, single-walled nanotube clay with a basic unit arrangement of an external curved octahedral $Al(OH)_3$ sheet on which separated internal $SiO_3(OH)$ tetrahedron units are linked upright to the octahedral vacancy via a covalent chemical bond between three mutual oxygen atoms [112]. With its empirical chemical composition $Al_2SiO_3(OH)_4$ and unique tubular structure, imogolite is regarded as a promising absorbent, catalyst, and catalyst support in various fields and can be easily synthesized by the low-temperature sol-gel method.

Due to the specific tubular structure and chemical properties, Bottero et al. could successfully introduce $SiCH_3$ groups to replace the SiOH groups at the inner surface of imogolite and create a hydrophilic outer Al(OH)Al surface with hydrophobic groups inside the nanotubes [113]. The modified imogolite reached a high specific surface area of about 800 m^2/g, showing an almost 2.5 times higher adsorption capacity of methane than that exhibited by unmodified imogolite. The organic/inorganic hybrid, composed of Fe-doped methyl-imogolite nanotubes with isomorphic substitution of Fe^{3+} ions for octahedral Al^{3+} ions, possessed lower band gap energy of 2.4 eV compared to 4.9 eV of bare methyl-imogolite nanotubes [114]. In the presence of H_2O_2, bare methyl-imogolite could mineralize 65% tartrazine under UV light illumination for 2 h, which was explained by the reactive -AlOOH group that is favorable to HO· radical generation. On the other hand, Fe-doped methyl-imogolite could mineralize 80% tartrazine under the same conditions because the isomorphic substitution of Al^{3+} by Fe^{3+} was beneficial for HO· radical production. Additionally, the silicon in imogolite could also be substituted by germanium, improving the catalytic performance and selectivity of glucose isomerization to fructose [115].

Furthermore, Kuroda et al. could prepare a novel functionalized Au/imogolite photocatalyst with morphologically controlled Au nanoparticles on the imogolite surface [116]. The particle size of Au was decreased from 20–50 nm to about 2–4 nm after loading on the imogolite surface. The synthesized imogolite via the hydrothermal method could

also be used as support for Cu(II)-grafted TiO_2 photocatalyst that could catalyze acetaldehyde photodegradation [117]. The as-prepared imogolite possesses a high specific surface area of 245 m^2/g, and the resultant imogolite-Cu(II)-grafted TiO_2 composite exhibits better photocatalytic activity for acetaldehyde degradation under visible light.

3.1.6. Wollastonite-Supported Photocatalyst

Wollastonite is a naturally forming calcium inosilicate mineral and sometimes contains a minor amount of Fe, Mg, and Mn substitution for calcium. It consists of an infinite chain unit arrangement of a pair of corner-sharing tetrahedrals alternating with a single tetrahedron with one edge parallel to the chain direction and Ca atom layers in octahedral coordination alternate with Si atom layers [118]. Consequently, it has attracted noticeable attention in the ceramic and cement industries due to its abundance, thermal, chemical, and mechanical stability as well as its outstanding biocompatibility. Early in 2009, wollastonite was used to prepare mesoporous TiO_2/SiO_2 nanocomposites with high specific surface areas (around 308 m^2/g), large pore volumes, and narrow distributions of pore size range in the absence of any surfactants [119]. Furthermore, a unique core-shell wollastonite@TiO_2 composite synthesized by a mechanochemical method could efficiently improve the dispersion of TiO_2 and reduce the TiO_2 dosage [120]. These wollastonite@TiO_2 particles are composed of the combination of van der Waals force, electrostatic attraction, and chemical bond. The as-prepared composite has superior characteristics in the white painting aspect, such as 96.9% of whiteness, 17.97 g/m^2 of hiding power, and 22.72 g/100 g of oil absorption.

Moreover, wollastonite is commonly regarded as promising support for immobilizing various semiconductors. For instance, Yao et al. prepared wollastonite/g-C_3N_4 by the facial calcination and acid leaching process with excellent durability and reusability [118]. The wollastonite/g-C_3N_4 photocatalyst exhibited high photodegradation efficiency of Rhodamine B, with a reaction rate constant that was 6.5 times better than that of pure g-C_3N_4, which could be ascribed to not only high surface area and porosity but also to the synergistic effect between g-C_3N_4 and wollastonite, and resultantly promoted the separation of photogenerated electron-hole pairs.

3.1.7. Basalt-Supported Photocatalyst

According to the definition of the International Union of Geological Sciences (IUGS) classification scheme, basalt is a dark-colored, fine-grained aphanitic igneous rock with major compositions of plagioclase and pyroxene minerals. Generally, it forms as an extrusive rock originating from the rapid cooling of magnesium-rich and iron-rich lava flows. As one of the most common rock types in the world, basalt contains rich MgO, CaO, and low amounts of SiO_2 and alkali oxides, which could be used as CO_2 adsorbents [121]. Early in 2012, natural basalt tuff could be modified by HNO_3 to construct Pd(II)-Cu(II)/basalt composite through the impregnating method [122]. This study showed the water contents of catalyst samples were negatively correlated to their reaction activity of low-temperature CO oxidation in a specific range of 1.6–7.2 wt%. Additionally, Qiu et al. used HF solution to modify basalt fibers and combine them with TiO_2 through microwave thermal treatment at 200 °C for 30 min [123], and after 5 h of ultraviolet light irradiation, the basalt fiber/TiO_2 could degrade 94% of Rhodamine B and exhibit excellent recyclability with a photocatalytic degradation rate still maintained at 86% in the fifth cycling test. The basalt fiber@perovskite $PbTiO_3$ (BF@ $PbTiO_3$) composite with three-dimensional core-shell nanostructure could be prepared via a sol-gel dip-coating technique yielding 290 $\mu mol \cdot gcat^{-1} \cdot L^{-1}$ CH_4 from adsorbed CO_2 after 6 h of reaction, as the basalt fiber surface could preferentially adsorb CO_2 molecules [124]. The photocatalytic CO_2 hydrogenation process was confirmed as below:

Basalt fiber: More CO_2 adsorption
$PbTiO_3$: Easy electron transfer and water adsorption (1)
Reduction: $CO_2 + e^- \rightarrow \cdot CO_2^-$

Oxidation: $H_2O + h^+ \rightarrow \cdot OH + H^+ \rightarrow H^+ + O_2$

CH_4 production: $H^+ + e^- \rightarrow \cdot H$

$CO_2^- + \cdot H \rightarrow \cdot CH \rightarrow \cdot CH_2 \rightarrow \cdot CH_3 \rightarrow CH_4$

Equations of CH_4 production from photoreduction of CO_2 with H_2O vapor over the BF@$PbTiO_3$ core-shell composite.

The 3% Ag/Ce^{4+}/La^{3+}-TiO_2@basalt fibers composite, prepared by sol-gel and coating routes, represented the best activity in the degradation of ammonia nitrogen in wastewater [125]. Moreover, the aggregation problem of TiO_2 particles was hindered, and the hydrophobicity of TiO_2 powder was significantly improved after being coated on basalt fibers. Compared with 93.9% and 70.7% of 3% Ag/Ce^{4+}/La^{3+}-TiO_2 photocatalyst, the ammonia and nitrogen degradation rate of 3% Ag/Ce^{4+}/La^{3+}-TiO_2/basalt fiber achieved 95.3%, and nearly 74% of total nitrogen was removed after a 6 h degradation process. At the same time, Kwak et al. prepared 3D core/shell microstructure by coating $Zn_{1-x}Mg_xO$ on basalt fibers with specific morphology through a modified sol-gel process [121]. The basalt fiber@$Zn_{0.75}Mg_{0.25}O$ presented superior photocatalytic activity and selectively for the photoreduction of adsorbed CO_2 to produce 5.0 μmol·$gcat^{-1}$·L^{-1} of CO gas after an 8 h reaction. This special core@ shell structure could effectively prolong the charge lifetime by restraining electron-hole recombination and thereby improve the photocatalytic efficiency for CO_2 reduction. Basalt fibers could be used as mineral core support to extend the adsorption of reactive species and the incident light properties. The synergistic effect between basalt fibers and Mg-incorporated ZnO shells would contribute to higher CO_2 absorption capacity and reduction efficiency for CO production.

3.1.8. Tourmaline-Supported Photocatalyst

Being classified as a semi-precious stone, tourmaline is a crystalline boron silicate mineral and has a unique trigonal crystal space group of *R*3*m*. Its special crystal structure is able to produce a spontaneous and permanent electric field in which electrons can be driven to flow continually from the negative to the positive pole. This electrostatic field on the tourmaline surface arises from its silicon–oxygen octahedral distortion. This polarization equips tourmaline with pyroelectric and piezoelectric properties with an electronic field strength of 106–107 V/m [126]. Aside from the natural electrical polarity, thermoelectricity, and piezoelectricity, tourmaline also possesses an infrared radiation function and negative ion release ability; thus, it is considered as a prospective material in the field of environmental protection.

The incorporation of tourmaline into a mixture of TiO_2 phases could effectively reduce the band gap energy of the as-prepared TiO_2/tourmaline composite to 2.9 eV and increase its specific surface area, exhibiting photocatalytic decomposition efficiency of gaseous formaldehyde approximately 6 times better than that of pure TiO_2 [127]. Fu et al. prepared CDs/tourmaline@ZnO composite by introducing a tourmaline core into a hierarchical ZnO nano-flower matrix decorated with carbon dots (CDs) as an active light sensitizer [6]. The photocatalytic efficiency of CDs/tourmaline@ZnO composite increased by 54% under visible light, where carbon dots broadened the visible light response ability and tourmaline prohibited photo-generated e^-/h^+ pair recombination to enhance the photocatalytic oxidization potential via spontaneous polarization and surface electric fields. The modification of the tourmaline surface with nitrogen-doped TiO_2 showed good activity for ethylene photo-oxidation [128]. The optimal percentage of tourmaline in the tourmaline/N–TiO_2 composite was calculated to be 4%, and the spontaneous electric field of tourmaline was applied to mediate the photogenerated electrons from N–TiO_2 to react with ethylene. Baeissa et al. studied the hybridization effect between tourmaline and mesoporous graphene/TiO_2 heterojunction on its photoactivity for CO_2 reduction under visible light [129]. The as-prepared composite had a high surface area of 340 m^2/g m and a relatively narrow band gap of 2.28 eV due to the existence of tourmaline. The surface polarization of tourmaline induced spatially varied energy levels and changed band bending

of TiO_2, therefore lowering the calculated band gap and restraining electron-hole pair recombination. Li et al. have more recently loaded tourmaline powder into g-C_3N_4/$BiVO_4$ heterojunction to enhance its automobile exhaust gas purification performance [130]. They found that the presence of tourmaline in the composite could increase the physical adsorption capacity via releasing negative ions, thereby increasing CO and NO decomposition efficiency by factors of 1.74 and 2.52 times, respectively. On the other hand, Bian et al. applied modified tourmaline as a novel photocatalyst to degrade methyl blue dye through a·OH^-mediated system [131].

3.1.9. Chrysotile-Supported Photocatalyst

As the most common asbestos form on the earth, chrysotile is a 1:1 layered hydrated magnesium silicate and belongs to the phyllosilicate kaolinite–serpentine mineral group with the idealized chemical formula $Mg_3Si_2O_5(OH)_4$ [27]. Generally, the chrysotile basic unit has trigonal symmetry and consists of a SiO_4 tetrahedral sheet layered with a magnesium octahedral sheet. The cation substitution in the chrysotile unit can modify its morphology and chemical or physical properties. Tang et al. fabricated TiO_2/micro-meso porous silica nanofibers (TiO_2/MMPSNF) based on the natural chrysotile via an innovative sol-adhesion synthesis strategy [28]. The Ti-O-Si chemical bond in this TiO_2/MMPSNF system could efficiently hinder the TiO_2 phase transition from anatase to rutile and control crystallite size growth. This TiO_2/MMPSNF composite exhibited higher specific surface area (197.1 m^2/g) and pore volume (0.46 cm^3/g) than those of the bare TiO_2 (39.4 m^2/g and 0.07 cm^3/g), which proves that TiO_2 nanoparticles are uniformly distributed on the chrysotile-based silica surface. Additionally, the TiO_2/MMPSNF composite obtained at 800 °C showed a higher degradation efficiency for Rhodamine B (RhB) with about 95% after 90 min compared with commercial TiO_2 (77.29%) and naked TiO_2 (17.6%) under the same conditions. Similar to other generally accepted TiO_2/SiO_2 photocatalyst systems, the hydroxyl groups on the chrysotile support surface could efficiently capture the photo-induced electrons and inhibit electron-hole recombination, which eventually enhanced its photocatalytic activity. Furthermore, this kind of monolayer dispersion structure could also provide a synergistic effect of nano-scale pore structure and adsorption ability [132]. Zhang et al. could successfully immobilize 0D Ag nanoparticles onto the modified 1D chrysotile nanowire surface to achieve an effective framework arrangement and better properties [133]. It was found that the BET surface area of Ag/SiO_2 composite reached 210 m^2/g and thus exhibited excellent photocatalytic performance for 4-nitrophenol reduction.

3.1.10. Talc-Supported Photocatalyst

As the softest mineral, talc is generally presented by the chemical formula of $Mg_3(OH)_2Si_4O_{10}$ and is naturally hydrophobic. As a result, natural talc hardly gets wet in water without surfactant. The surface property of talc can be altered after being coated by TiO_2 particles, and thereby its wettability is evidently improved [134]. It is also considered that talc has an outstanding activity for adsorbing small organic molecules, promoting the photocatalytic reaction of the as-prepared TiO_2/talc composite. Ai et al. intercalated TiO_2 nanoparticles into talc interlayers to increase the specific surface area and reduce average pore diameters [135]. As a photocatalyst carrier, talc has a strong adsorption ability and intensifies the photoabsorption capability. Thus, the talc/TiO_2 nanocomposite could degrade more than 99.5% of 2,4-dichlorophenol after 1 h and maintain this photocatalytic efficiency even after recycling 20 times. Actually, owing to its low hardness, talc is mainly used as a thickening agent and lubricant ingredient in ceramics, paint, and cosmetics products. Consequently, its application in the photocatalysis field is finite.

3.2. 2D Mineral-Supported Photocatalyst

3.2.1. Smectite-Supported Photocatalyst

Smectite is defined as a clay mineral group consisting of a 2:1 layer silicate structure that could expand and contract depending on water content. The basic structural unit is composed of an alumina octahedral sheet sandwiched between two inward-pointing tetrahedral sheets, and the layers extend in the a and b directions but are weakly bonded by a negative charge which is easy to replace with various cations and allows water and other molecules to enter between the layers, causing expansion in the c direction. Due to ion substitution, the members of the smectite group are divided into dioctahedral minerals such as montmorillonite, beidellite, and nontronite and trioctahedral minerals such as hectorite (Li-rich), saponite (Mg-rich), and sauconite (Zn-rich). These subgroup minerals possess orderly stacked lamellar structures and excellent adsorption ability and therefore are regarded as one of the most promising photocatalyst support materials. Here, TiO_2 is taken as a photocatalyst example to introduce some common synthesis methods in Table 2.

Table 2. Synthesis methods using natural smectite minerals as TiO_2 support.

Photocatalyst	TiO_2 Precursor	Method	Synthesis Temperature	Specific Surface Area (m^2/g)	Application	Refs.
F-doped TiO_2/exfoliated bentonite	Tetrabutyl titanate	A liquid exfoliation and facile sol–gel method	400 °C	49	Gaseous toluene	[136]
Ag/TiO_2/bentonite	Titanium isopropoxide	A facile thermal decomposition method	500 °C	80	S. aureus, E. coli and human embryonic kidney cell line	[137]
Au–TiO_2/bentonite	Tetra-n-butyl titanate	Deposition–precipitation and calcination method	400 °C	178	Sulforhodamine B photodegradation	[138]
F, V and Mn co-doped TiO_2-pillared bentonite	Butyl titanate	A sol-gel method	500 °C	86	NO photocatalytic denitration	[139]
g-C_3N_4/TiO_2/bentonite	Titanium butoxide	A wet impregnation process	60 °C	70	Reactive brilliant red dye	[140]
TiO_2 pillared montmorillonite	Tetrabutyl titanate	An intra-gallery template method	500 °C	392	MB	[141]
Montmorillonite Modified TiO_2	Tetra-isopropyl orthotitanate	A single sol-gel method	500 °C	83	CO_2 reduction	[142]
Ni/montmorillonite supported TiO_2	Tetraisopropyl orthotitanate	Sol-gel method	500 °C	58	CO_2 reforming of methane	[143]
Montmorillonite dispersed single wall carbon nanotubes (SWCNTs)/TiO_2	Tetraisopropyl orthotitanate	A simple sol-gel assisted wet-impregnation method	180 °C	--	H_2 production	[144]
Ag@AgCl-TiO_2/organic rectorite/quaternized chitosan	Titanium tetraisopropoxide	Sol–gel combing calcination technique, precipitation and photoreduction combined with emulsification/chemical cross-linking method	80 °C	89	MO	[145]
Ag-AgCl-TiO_2/rectorite	Titanium tetraisopropoxide	A facile deposition–photoreduction method	Room temperature	--	Acid orange and 4-NP	[146]
Bi-crystalline TiO_2/rectorite	Titanium tetraisopropoxide	A facile sol–gel method	80 °C	100	Acid red G and 4-NP	[147]
TiO_2-pillared saponite	Titanium tetraisopropoxide	Intercalation, neutralization and calcination process	400 °C	154	BPB	[12]
TiO_2-montmorillonite	Tetrabutyl titanate	Hydrothermal	160 °C	77	MB	[148]
TiO_2/pillared clays	Titanium isopropoxid	Wet impregnation through stirring followed by calcination	500	29±5	TCS, 2,6-DCP and BPA	[149]
TiO_2/sepiolite	Titanyl sulfate	Structural assembly and thermal treatment	400	135	HCHO removal and H_2 evolution	[150]
Bi_2MoO_6/TiO_2/sepiolitte	Titanyl sulfate	A facile hydrolysis precipitation and calcination crystallization route	500	100	HCHO	[151]
TiO_2-BiOBr-bentonite	Tetrabutyl titanate	Solvothermal	160	125	Phenol	[152]

Bentonite-TiO_2	Titanium isopropoxide	Sol-gel	500	124	TC	[153]
Fe_3O_4 @TiO_2/silica aerogel	Tetraethyl orthotitanate	Sol-gel and ultrasound assisted reflux technique	400	347	TC	[154]

Bentonite-Supported Photocatalyst

As a mineralogy term to define naturally occurring sedimentary mud-rocks that are composed mainly of swelling smectite clay, bentonite is an aluminium phyllosilicate mineral containing over 70% montmorillonite, a small amount of beidellite, and impurities from other mineral phases such as kaolinite, quartz, and calcite. Its basic structural unit generally consists of one octahedrally coordinated alumina sheet placed between two tetrahedrally coordinated silica sheets. It has net negative charges due to the isomorphous substitution of Al^{3+} for Si^{4+} in the tetrahedral site and Mg^{2+} for Al^{3+} in the octahedral site and can be balanced by the presence of exchangeable cations in the lattice structure [136,155]. Owing to its abundant availability, large specific surface area, high cation exchange capacity, and resultant strong adsorption/desorption capacity of ionic or polar compounds, bentonite is widely regarded as the eco-friendly adsorbent and catalyst substrate in wastewater treatment, such as for organic dyes and heavy metals. For instance, Nguyen et al. could disperse Ag-modified TiO_2 onto bentonite surfaces to enhance the phenol removal efficiency from 23.25% to 98.94% due to the inhibiting effect of anatase-to-rutile phase transformation [156]. According to the dominant exchangeable cations, bentonite can also be named as Na, Ca, and K bentonite. Among them, Na bentonite has a remarkable swelling property that can absorb water as much as several times its dry mass to be expanded. The incorporation of Ag/TiO_2 nanoparticles into Na bentonite layers could increase its specific surface area to 80 $m^2 \cdot g^{-1}$ via the cation exchange process, as shown in Figure 6a [137]. The synthetic Ag/TiO_2/bentonite composite exhibited considerable antibacterial effect and biochemical applications for its small particle size, enabling easy penetration through bacterial walls. The composite showed a redshift in absorption wavelength, which might be related to the charge transfer transition of interlayer tetrahedral and octahedral ions in bentonite clay. Due to the bentonite structure modification effect, Ag/TiO_2/bentonite nanocomposite is proved to be an effective nontoxic antibacterial material for human health. Moreover, the exfoliation process could increase the specific surface area of bentonite, thereby improving its adsorption ability. For instance, Ma et al. synthesized exfoliated bentonite/g-C_3N_4/Ag_3PO_4 composite with increased specific surface area and adsorption properties [157]. The adsorption capacity of g-C_3N_4/Ag_3PO_4 photocatalyst for RhB dye increased by more than two times after anchoring the photocatalyst onto the exfoliated bentonite clay surface. Because the negatively charged surface of exfoliated bentonite has more electrostatic attraction to dye molecules, and its enhanced photocatalytic activity is ascribed to the fact that exfoliated bentonite has a restrained effect on Ag_3PO_4 decomposition and synergistic effect between bentonite structure and semiconductors.

Additionally, bentonite can also be utilized as special loading material to fabricate a bifunctional catalyst for pharmaceutical photodegradation and methanol electrooxidation. Thiruppathi et al. found that 6% bentonite/$CuWO_4$ nanoparticles could degrade 98.8% of a diclofenac sodium solution under visible light irradiation with superior reusability up to 6 cycles [158]. It was revealed that 6% bentonite/$CuWO_4$ shows an increased active surface area of 21.7 nm and thereby reduced photogenerated electron-hole pairs recombination rate as well as increased electrical conductivity. The metal ions originating from bentonite could make the absorption edge of $CuWO_4$ shift to higher wavelengths, while the electrostatic attraction between $CuWO_4$ and negatively charged bentonite could control the colonization of excited charge carriers of $CuWO_4$. Furthermore, a 2D bentonite nanosheet was employed to couple with Z-scheme WO_3/g-C_3N_4 heterojunction for selective photocatalytic reduction of CO_2 under visible light illumination [159]. The WO_3/bentonite/g-C_3N_4 composite displayed the highest photocatalytic activity for CH_4 production, which is 6.01 times higher than that produced using WO_3/g-C_3N_4 composite. Moreover,

bentonite clay enhanced the selectivity of photocatalysts during the CO_2 reduction process to produce 76.07% methane compared with 36.66% for the WO_3/g-C_3N_4 composite. As the electron mediator, bentonite could promote photoinduced charge carrier separation and is favorable for trapping electrons, resulting in efficient CO and CH_4 evolution. To further facilitate the photocatalyst separation and recycling process under an external magnetic field, Liu et al. prepared magnetic Fe_3O_4/bentonite and grew flower-like BiOBr onto its surface via sodium dodecyl sulfate modification (SDS) through the procedure drawn in Figure 6b,c [10]. According to the obvious redshift and increased intensity of light absorbance and decreased band gap energy, it is deemed that bentonite acts as a negatively-charged photocatalyst substrate that could capture electrons, inhibit recombination of photoexcited e^-/h^+ pairs, and enhance light absorption ability, as the mechanism is shown in Figure 6d. In addition, the remarkably improved adsorption capacity of tetracycline and ciprofloxacin is achieved by bentonite introduction via physical adsorption force and enlarged surface area. Moreover, Riaz et al. applied polymer poly-naphthylamine (PNA) to modify bentonite clay, obtaining bentonite/PNA nanohybrids with core-shell morphology and better electroactivity [160]. It was revealed that PNA existed in clay shells and the as-prepared bentonite/PNA nanohybrid exhibited higher degradation efficiency of orange G dye, which is two times more than that determined for pure bentonite.

On the other hand, organophilic bentonite is fabricated by intercalating 1,10-phenanthrolinium cation into its interlayer space and proved to be an efficient photocatalyst for the photodegradation of indigo carmine [161].

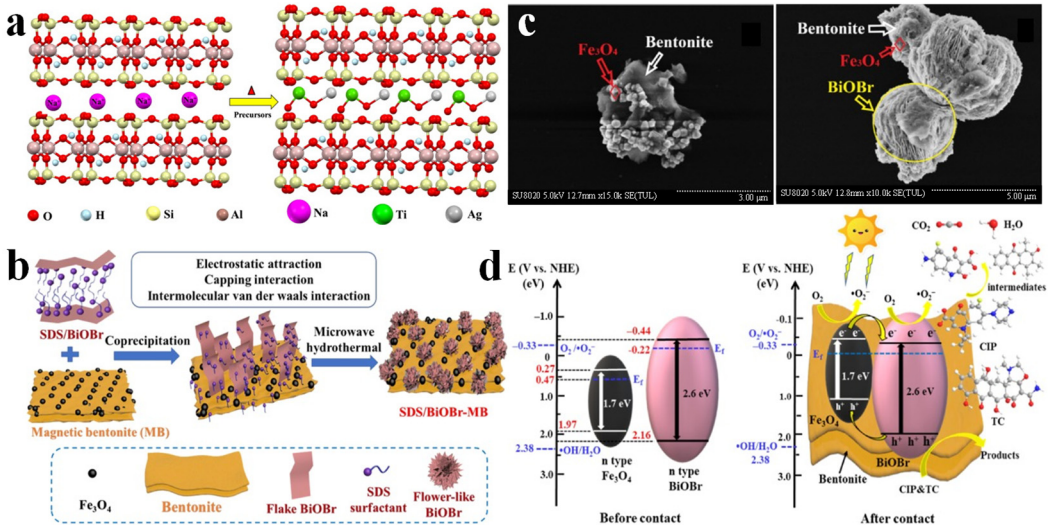

Figure 6. (**a**) Schematic illustration of the reaction mechanism of Ag/TiO_2 nanoparticles and its intercalation processes into the bentonite clay; (**b**) scheme of SDS/BiOBr−MB synthesis; (**c**) FE−SEM images of magnetic bentonite (MB) and BiOBr−MB at 15 k and 10 k magnification; (**d**) schematic representation of the mechanism of enhanced photodegradation of tetracycline (TC) and ciprofloxacin (CIP) by SDS/BiOBr−MB. Adapted with permission from Ref. [10]. Copyright 2020, Elsevier B.V; Adapted with permission from Ref. [137]. Copyright 2017, Elsevier B.V.

Montmorillonite-Supported Photocatalyst

Montmorillonite (MMT) is widely considered as a representative 2D sheet-like clay mineral of the phyllosilicate–smectite group and consists of three-layer structural units (TOTs) in which one octahedral alumina sheet is sandwiched between two tetrahedral silica sheets and the silicate layers stack by relatively weak forces. The montmorillonite surface is negatively charged due to the isomorphic substitution of Mg ions on the Al octahedral sites and balanced by cations via strong electrostatic force, resulting in the formation of the interlayer space [40,141]. Owing to its large specific surface area, swelling nature, high cationic exchange capacity, and adsorption capability, montmorillonite is commonly recognized as a promising material as an adsorbent and catalyst host, and it

can accept and donate electrons due to the occurrence of Lewis acids and bases. As the most common semiconductor, TiO_2 has excellent photocatalytic efficiency but severe recycling problems. Huang et al. fabricated TiO_2/carbon-montmorillonite composites with superior separability via a bio-mimetic coating method followed by a carbonization process [162]. Although its photocatalytic efficiency remains unchanged after immobilizing onto montmorillonite, the as-obtained photocatalyst could be easily settled by simple gravity sedimentation without any apparent photoactivity reduction. Another early study investigated the montmorillonite modification effect on TiO_2 for photocatalytic reduction of CO_2 with water vapor and achieved high CH_4 and CO yield rates of 441.5 and 103 $\mu mol \cdot gcatal^{-1} \cdot h^{-1}$, respectively [142]. The study showed that montmorillonite loading could reduce the particle size from 18.73 to 13.87 nm and increase the surface area from 46.98 to 82.62 $m^2 \cdot g^{-1}$. When intercalated with TiO_2 particles, montmorillonite functions as a barrier to inhibit agglomeration and controls the crystal phase formation as well as enhances hydrophilicity of the as-prepared photocatalyst. Later, Tahir et al. reported that Na-montmorillonite/TiO_2 composite could exhibit considerably improved CO conversion efficiency (750 $\mu mol \cdot h^{-1} \cdot g^{-1}$) and selectivity [143]. During the photocatalytic dry reforming of methane process, montmorillonite acts as a mediator to transport electrons and promotes TiO_2 dispersion on its surface with better stability and large surface area, while nickel ions serve as an electron sink to efficiently prevent charge carrier recombination. Umer et al. designed a simple sol-gel-assisted wet-impregnation strategy to prepare montmorillonite-dispersed single-walled carbon nanotubes (Mt-SWCNTs)/TiO_2 ternary heterojunction composites [144]. They reported that the maximum H_2 yield rate over Mt-SWCNTs/TiO_2 reaches 9780 $ppm \cdot h^{-1} \cdot g^{-1}$ under visible light illumination, which is 2.05 and 1.33 times higher than that of Mt/TiO_2 and SWCNTs/TiO_2 composites, respectively. The SWCNTs in the composite work as a photosensitizer, which induces a slight reduction in band gap energy level from 3.12 to 2.78 eV, and its synergism effect with montmorillonite increases the absorption in the visible light region, promotes the photogenerated electron-hole pairs separation, and improves photocatalyst stability. Peng et al. assembled layered MoS_2 nanosheets uniformly onto montmorillonite surfaces via hydrogen bonds, and the as-obtained composite could degrade methyl orange completely after 2 h due to its larger surface area, more reactive sites, and synergistic adsorption capacity, as depicted in Figure 7 [163]. Obalová et al. deposited ZnS nanoparticles onto montmorillonite after cetyltrimethylammonium bromide stabilization and achieved photodegradation efficiency of 79% for N_2O under 24 h illumination [164]. Additionally, Cu_2O nanoparticles, which can easily aggregate, could be homogeneously distributed in montmorillonite clay support, yielding preferable adsorption-flocculation capacity of Microcystis aeruginosa [165]. It is stated that 26.31% Cu_2O-montmorillonite can remove 90.4% of Microcystis aeruginosa under visible light irradiation after 3 h and effectively reduce its mass and photoactivity loss to ensure environmental safety. Similarly, Zhang et al. incorporated AgCl nanoparticles into montmorillonite interlayers in the presence of HCl vapor to produce AgCl/montmorillonite with high photocatalytic azo-dye degradation efficiency [166]. Montmorillonite could tailor AgCl morphology, mediate the electron transfer via the contained electrochemically active iron species, and provide a larger surface area for pollutant adsorption. Therefore, the more active {100} crystal planes in the as-synthesized cube-like AgCl/montmorillonite composite might further increase the photocatalytic activity and stability. Owing to the net negative charges on its surface, montmorillonite is used to hybridize with g-C_3N_4 /NiCoP cocatalyst to achieve a high photocatalytic hydrogen evolution rate (12.50 $mmol \cdot g^{-1} \cdot h^{-1}$) with Eosin Y–sensitization under visible light irradiation [167]. The maximum quantum yield of 40.3% is thought to be related to the better distribution of g-C_3N_4 sheets and the electrostatic repulsion originating from negatively-charged surfaces. Furthermore, other studies reported that g-C_3N_4/montmorillonite composite is also a prospective candidate as a photoelectrochemical sensor for a small concentration of Cu^{2+} [9]. The specific surface area increased from 8.45 m^2/g of g-C_3N_4 to 61.63 m^2/g of g-C_3N_4/montmorillonite composite, and the photogenerated electron-hole pairs recombination rate was

obviously lower after being combined with montmorillonite according to BET and PL analysis.

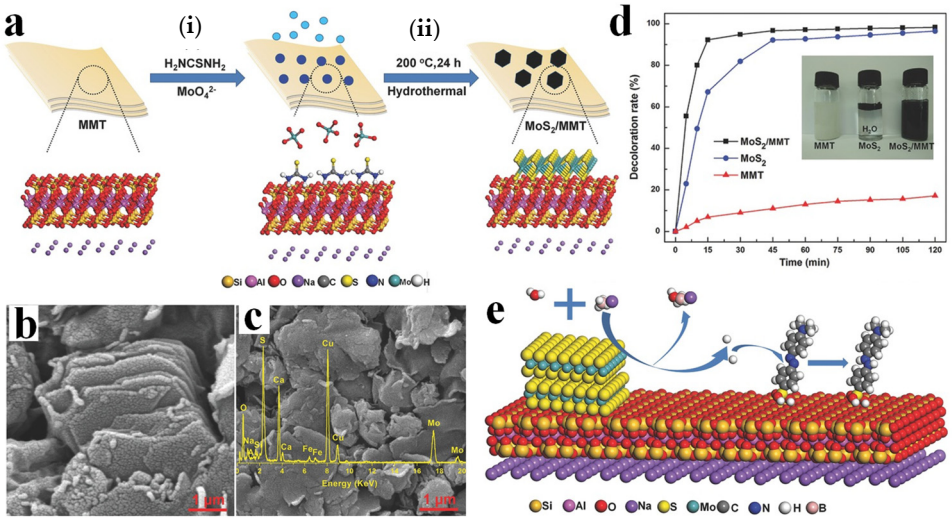

Figure 7. (**a**) Illustration of synthesis strategy for molybdenum disulfide/montmorillonite (MoS_2/MMT) composite: (**i**) adsorption of thiourea on the surface of MMT; (**ii**) hydrothermal synthesis of MoS_2/MMT at 200 °C for 24 h; SEM images of (**b**) MMT and (**c**) MoS_2/MMT, the inset shows the EDS spectrum of MoS_2/MMT; (**d**) decoloration of methyl orange (MO) with MMT, MoS_2 and MoS_2/MMT, and the inset shows digital photograph of the samples dispersed in water; (**e**) schematic illustration for the catalytic reaction mechanism. Adapted with permission from Ref. [163]. Copyright 2016, WILEY-VCH Verlag GmbH & Co. KGaA, Weinheim.

Nontronite Catalysis

Deriving from the weathering process of biotite and basalts, nontronite belongs to a small group of smectite clays and contains over 30% Fe_2O_3 and a little Al_2O_3, which obtains brownish or dull greenish appearance due to high iron content. It is generally composed of two tetrahedral silica layers and one octahedral sheet in which the octahedrons are only occupied by Fe^{3+}, unlike montmorillonite. The net negative charges on the nontronite surface mainly originate from ion substitution in the tetrahedral layers [168]. Liu et al. reduced the iron species in nontronite clay to Fe(II) and achieved efficient Cr(VI) reduction with the assistance of organic ligands [169]. Additionally, the reduced nontronite was investigated to be effective for *E. coli* degradation as the soluble metal ions released from clays can be antibacterial under non-neutral pH conditions. The dissolved Al^{3+} compromises the outer membrane of bacteria and further facilitates the soluble Fe^{2+} diffusion into the cell. To decrease the repulsion between the negatively charged bacteria and the catalyst surface, positively charged chitosan was intercalated into the reduced nontronite to acquire more persistent and stable antibacterial activity [170]. Unlike pure reduced nontronite, chitosan-reduced nontronite still exhibits antibacterial capabilities at pH 7 and 8 conditions.

Rectorite-Supported Photocatalyst

Consisting of regular 1:1 alternate stacking of non-expansible dioctahedral mica-like layers and expansible dioctahedral smectite-like layers, rectorite is a natural interstratified layered silicate mineral and exhibits high thermal and chemical stability, large specific surface area, as well as high cation exchange capacity. These remarkable properties could enable rectorite to adsorb and stabilize organic substances both on its external surface and within its interlaminar space via interaction or substitution, making it a promising catalyst carrier [171].

The ultrasonic process was early applied to expand rectorite's interlayer space and then embedded Bi species onto its lamellar layers via ion exchange, which could enhance the specific surface area of Bi-modified rectorite composites and achieve closer contact between the photocatalyst and pollutant [172]. Later, Guo et al. substituted the exchangeable Ca^{2+} or Mg^{2+} ions of rectorite with Ag^{+} and therefore loaded Ag_3PO_4 onto lamellar rectorite layers via the ultrasound-assisted precipitation method [173]. Ag_3PO_4/rectorite calcinated at 400 °C showed photocatalytic degradation efficiency of methyl orange with 6.6 times higher than that determined for pure Ag_3PO_4, which was explained by the higher specific surface (13.6 m^2/g) compared with that of bare Ag_3PO_4 (3.3 m^2/g) and better visible light adsorption capacity. Additionally, the presence of rectorite could increase the stability of photocatalysts by inhibiting Ag_3PO_4 from photochemical decomposition. Rectorite could capture electrons to generate O^{2-} radicals with the adsorbed oxygen molecules and thereby prohibit electron-hole recombination and Ag_3PO_4 photo-corrosion. As a photosensitizer with adjustive wide spectrum responsive ability, Ag_2O was incorporated into rectorite clay to obtain Ag_2O/rectorite nanocomposites with high efficiency under broader spectrum light, especially near-infrared light irradiation [174]. The Nyquist curve comparison of different Ag_2O/rectorite samples indicated that the existence of rectorite clay could provide more active sites to detach photoinduced electron-hole pairs and effectively improve photocatalyst stability. The RhB dye degradation experimental results showed that the 70% Ag_2O/rectorite nanocomposite exhibits a clear redshift, a strong visible and near-infrared light absorption in the spectrum range of 220–2200 nm, and the highest photocatalytic activity if compared to pure Ag_2O and rectorite. Additionally, the $\cdot O^{2-}$ radical was proved to be the primary active species during the photocatalytic degradation process of RhB dye under visible and near-infrared light irradiation. Similarly, in the ternary Ag/AgI/BiOI-rectorite nanocomposite, rectorite, as support, plays an outstanding role in adsorbing the organic pollutants and facilitating the photogenerated charge carrier separation [175]. Bu et al. incorporated In_2O_3 particles into rectorite clay matrices to acquire visible-light photoactivity of In_2O_3/rectorite composite and to achieve a remarkable surface area improvement from 13.5 m^2/g of In_2O_3 to 198.51 m^2/g of In_2O_3/rectorite composite [8]. The composite showed a noticeable redshift of the absorption edge from 460 nm to 355 nm and improved photocatalytic efficiency, which was explained by the doping effect of some ions that exist in rectorite and the synergetic effect between the ordered rectorite structure and In_2O_3 particles. According to previous reports, the rectorite could influence the TiO_2 growth process and stabilize the anatase phase. For instance, during the synthesis of porous lamellar sulfur-doped TiO_2/rectorite composites, rectorite could stabilize a higher amount of anatase TiO_2. Moreover, rectorite as a disperser and carrier could increase the specific surface area from 57.2 to 187.5 m^2/g [176]. The substitution of lattice Ti^{4+} by S^{6+} creates an impurity energy level that could also reduce the band gap from 3.2 to 2.8 eV. Thus, the intercalation effects of rectorite could improve metronidazole removal efficiency from 71.8% to 93.8% under visible light irradiation. Moreover, iron-modified rectorite prepared via ultrasonic-assisted ion exchange and in situ hydrolysis could show excellent bifunctional adsorbent and photocatalyst properties [177]. It was assumed that iron modification could increase layer-to-layer spacing and specific surface area, which increases the maximum adsorption capacity of Rhodamine B by 11 times. The electron spin resonance spectroscopy (ESR) results showed that it substantiates ·OH radical produced by iron-modified rectorite functions as primary reactive oxygen species in the presence of H_2O_2 under visible light illumination during the photo-Fenton process. Later, similar iron-modified rectorite could be successfully fabricated via the degradation of Rhodamine B and exhibit excellent simultaneous removal efficiency of tetracycline hydrochloride and Cr(VI) in a Fenton-like process [178]. It was proved that the existence of tetracycline hydrochloride enhanced the Cr(VI) reduction rate by 47.4-fold, which was ascribed to its favorable effect on Cr(VI) reduction and its suppressing effect on Cr(III) reoxidation, while involving RhB dye could increase the interlayer spacing of the rectorite and induce

more iron ions into its interlayers, thus facilitating pollutant molecular diffusion, inhibiting iron leaching, and strengthening its electrical conductivity.

Saponite-Supported Photocatalyst

Saponite has a general chemical formula of $Ca_{0.25}(Mg, Fe)_3((Si, Al)_4O_{10})(OH)_2 \cdot n(H_2O)$ and refers to a trioctahedral group of smectite minerals. Its charge originates from Al substitution for Si in the tetrahedral sheet, which greatly influences its acidity. Generally, saponite is more thermally stable than montmorillonite. The pillarization process is the common technique to prepare semi-synthesized materials by inserting or immobilizing metal oxide into the interlayer space of clay minerals. The swelling ability and exchangeable cations of smectite minerals enable this modification method to obtain unique photocatalytic properties of specific metal oxides. Nikolopoulou et al. could incorporate TiO_2 onto saponite clay via solvothermal reaction, and the obtained TiO_2/saponite composite exhibited the highest photocatalytic NO_x gas degradation activity when the titania/saponite mass ratio reached 0.2 [179]. Moreover, these TiO_2/saponite photocatalysts showed mesoporous structure with improved pore volume (from 0.19 to 0.83 mL/g) and specific surface area (from 125 to 346 m^2/g) compared to pure saponite. Additionally, its enhanced photocatalytic efficiency could be ascribed to a better distribution of titania onto saponite surface as well. Later, Fatimah et al. could load TiO_2 onto the pillared saponite followed by applying tris(2,2′-bipyridyl) di-chlororuthenium (II) complex as a photosensitizer for bromophenol blue photodegradation [12]. This pillarization process increased the basal spacing of saponite from 14.95 Å to 16.27 Å and the specific surface area from 110 m^2/g to 154 m^2/g. Meanwhile, the photosensitization produces an obvious absorption spectra shift to the visible light range. Saponite as titania support could achieve slight catalytic activity improvement and better catalyst reusability.

3.2.2. Kaolinite-Supported Photocatalyst

Kaolinite ($Al_2Si_2O_5(OH)_4$) is a 1:1-type planar hydrate phyllosilicate clay mineral, in which the basic block consists of octahedral aluminium hydroxide sheets and tetrahedral silica sheets bridged through a co-sharing oxygen atom. The adjoining lamellae are linked to one another via hydrogen and covalent bonds [180], and the strong interaction forces make kaolinite chemically stable and a suitable support for immobilizing the other components. Generally, rocks rich in kaolinite are known as kaolin or China clay and have low swelling and cation-exchange capacity, which are widely used in various industries such as paper filling, ceramic production, painting, and wastewater treatment.

Due to its low cost, high efficiency, and non-toxicity, there are numerous works related to loading TiO_2 onto various substrates for various applications such as wastewater treatment and heavy metal removal. For instance, Kočí et al. compared the pure TiO_2 and kaolinite/TiO_2 composite in terms of CO_2 photocatalytic reduction efficiency [181]. They found that kaolinite could decrease anatase crystallite size, change surface acid–base properties and inhibit electron-hole pair recombination. Later, Sia et al. prepared N-doped TiO_2/kaolinite composite for photodegradation of Congo red in a semi-continuous reactor system [30]. This work showed that the as-prepared N-doped TiO_2/kaolinite composite exhibited higher photocatalytic performance, which was explained by the fact that kaolinite as a TiO_2 support provides excellent adsorption ability, enhanced photocatalytic oxidation ability, and easy recovery. Additionally, a new 0D/2D hierarchical C-doped TiO_2/kaolinite was assembled to promote the generation of Ti(III) species through the synthesis process, shown in Figure 8a, and thus obtain excellent photoactivity under visible light [182]. The latter composite showed high removal efficiency of ciprofloxacin following the pseudo-first-order kinetic model. The simulated reaction rate constant of the as-prepared C-doped TiO_2/kaolinite composite is 0.00597 min^{-1}, which was approximately 3.24 and 24.88 times higher than that of C-doped TiO_2 and pure TiO_2, respectively. The morphology changes before and after modifying kaolinite are shown in Figure 8b,c. The

accumulated net charge originating from negative hydroxyl groups on the kaolinite surface could produce a built-in electric field at the interface between the kaolinite and TiO_2 favorable for the fast separation of photogenerated carriers, and lamellar kaolinite as substrate could prompt bare TiO_2 dispersion and enable efficient photocatalyst recovery by virtue of its large crystallite size and high specific gravity. However, the efficiency of these TiO_2/kaolinite photocatalysts under visible light was still relatively low even after modification. Therefore, Li et al. designed a highly efficient self-assembly g-C_3N_4/TiO_2/kaolinite composite to advance visible light-harvesting ability [5]. As illustrated in Figure 8d, the small crystalline TiO_2 particles and more exposed g-C_3N_4 sheets are well disposed on the negatively charged kaolinite surface for more effective electron-hole separation. Furthermore, natural kaolinite clay has a unique sandwich structure that can limit crystallite growth and alter the framework. Zhang et al. showed that g-C_3N_4 loaded on a porous kaolinite-derived template could significantly enhance the photocatalytic hydrogen evolution rate under visible light, approaching 1917 $\mu mol \cdot g^{-1} \cdot h^{-1}$ compared with 810 $\mu mol \cdot g^{-1} \cdot h^{-1}$ of unmodified g-C_3N_4 [183]. The natural kaolinite functioned as a morphology template, providing a large specific surface area and more defect active sites to mediate hole reactivity towards interfacial oxidation. In order to explore the interfacial electronic property of heterostructures, a density functional theory (DFT) calculation was utilized to depict the possible electron transfer direction of the Kaol/Degussa P25 composite [184]. This DFT computation revealed an interlayer electron transfer from kaolinite to TiO_2, increasing the electron density of the TiO_2 space charge regions and decreasing the electron density of the kaolinite surface. Thus, Kaol/P25 composite could be a traditional type II heterostructure, and its interfacial Al–O–Ti bonds were efficient charge transfer channels.

On the other hand, natural kaolinite is generally regarded as an excellent adsorbent material, which could also show good photocatalytic activity after doping or modification. For instance, Fida et al. developed a new bifunctional Ti–Fe kaolinite composite via precipitating a certain amount of Ti and Fe species [31]. They reported that the specific surface area of the as-prepared Ti–Fe kaolinite composite was 5.5 times as much as that of the pristine kaolinite, and a low pH value can promote its Cr(VI) removal process. Later, Shawky et al. reported that exfoliated kaolinite nanolayers obtained by the intercalation technique could exhibit outstanding degradation efficiency of Rhodamine B dye that increased slightly with decreasing solution pH [29]. These results were explained by the electrostatic interactions between the siloxane surface of kaolinite and the carboxylic group of RhB molecules that would increase at lower pH, therefore promoting RhB discoloration. Additionally, the exfoliation process exposed more metal oxide impurities on kaolinite nanolayers and thus prompted its photocatalytic properties. The ongoing research will open an auspicious door for extensive applications of natural kaolinite clay in the environmental purification and remediation fields.

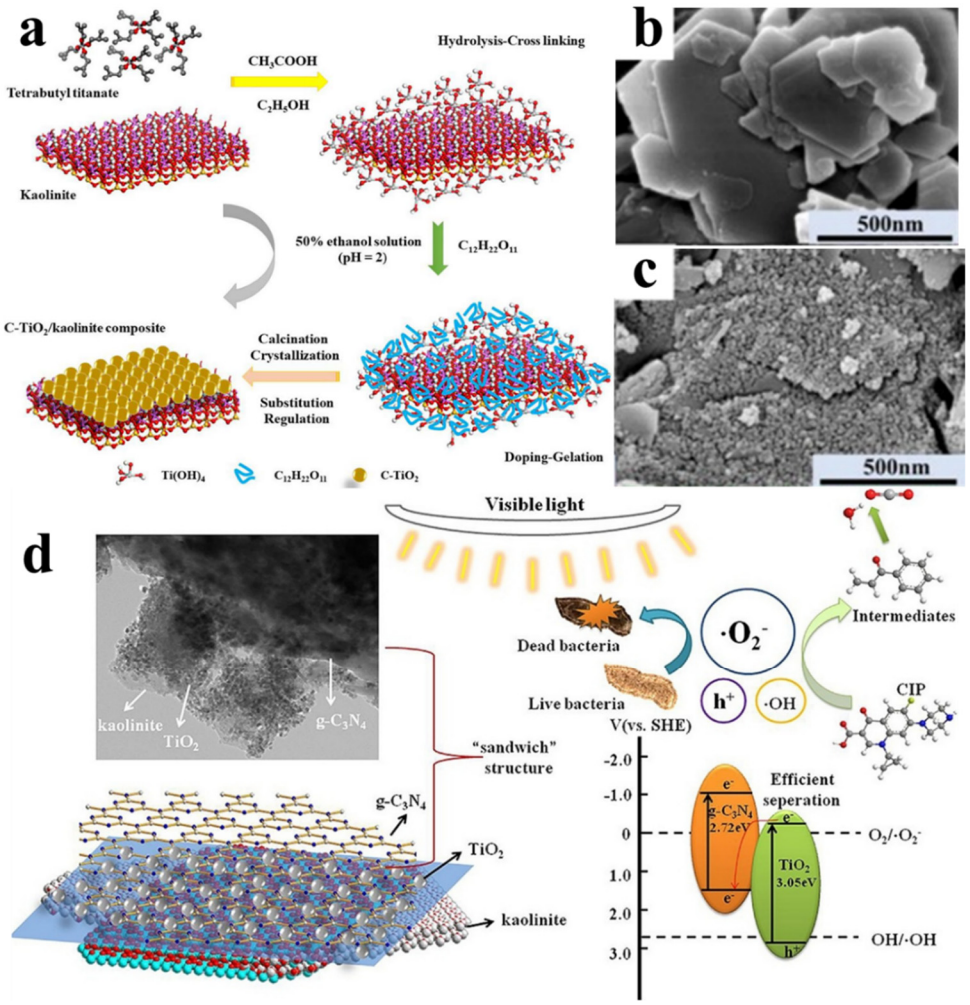

Figure 8. (**a**) The schematic diagram of the synthesis strategy of the prepared C-doped TiO_2/kaolinite composite; field emission scanning electron microscope (FESEM) images of (**b**) kaolinite and (**c**) C-doped TiO_2/kaolinite; (**d**) schematic diagram of the enhancement mechanism for the degradation process under visible light towards g–C_3N_4/TiO_2/kaolinite composite. Adapted with permission from Ref. [5]. Copyright 2020, Elsevier B.V; Adapted with permission from Ref. [182]. Copyright 2017, Elsevier B.V.

3.2.3. Dickite-Supported Photocatalyst

Dickite is a phyllosilicate clay mineral belonging to the kaolin–serpentine group, with kaolinite-type composition but a different polymorph crystal structure. Dickite consists of double 1:1 layered SiO_4 tetrahedral and AlO_6 octahedral sheets within a monoclinic symmetry, distinguished from natrite by different stacking sequences of two 1:1 silicate layers. Expanded dickite layers were obtained via rapid heating of the mixture of the dickite–urea intercalation complex and $KClO_3$ and the deposited TiO_2 particles on the surface by thermal hydrolysis of the expanded dickite and $TiOSO_4$ suspension [185]. It was revealed that the addition of $KClO_3$ could trigger an explosive reaction to produce large amounts of gases in a short time. The results from XRD, EDS, and FTIR showed expanded dickite came from the combination of the edge expansion of layers caused by 'tiny bombs' exploded on the cross-section of layered particles and a synergistic effect on expanding the inside of the layers because of the internal urea decomposition.

It was confirmed by XRD patterns that the dickite carrier could exert an obvious inhibition effect on the crystallization and crystal growth of TiO_2, and the inhibition effect differences between raw dickite and expanded dickite were related to the different specific surface areas. Additionally, expanded dickite, with nearly 10 times larger specific surface area, could apparently provide many more active adsorption sites. The enhanced

photocatalytic ability for the removal of methyl orange of TiO_2-impregnated expanded dickite was also attributed to the higher specific surface area and the size effect of the dickite carrier.

3.2.4. Mica- and Muscovite-Supported Photocatalysts

As a naturally occurring lamellar silicate mineral group, mica has distinctive perfect cleavage planes parallel to the (001) plane and a characteristic unit consisting of two tetrahedral silica sheets held together by one octahedral alumina sheet via electrostatic forces [186]. In general, mica mineral is hydrophilic due to the hydrogen-bonding character of the surface hydroxyl groups. After substituting most OH^- ions present at the hexagonal cavities of mica surface by F^- ions, the modified fluorine mica is formed, which is less hydrophilic than other clays and shares similar expandable properties with montmorillonite. Previous studies showed that the photocatalytic efficiency was highly dependent on the ability to concentrate the target pollutants near the vicinity of photocatalysts. The common toxic organic pollutants are highly hydrophobic and thus restrain the performance of many efficient photocatalysts. On this basis, it was desired to design TiO_2 pillared fluorine mica composite via conventional thermal treatment [187]. Several composites consisting of TiO_2 and different mineral supports were tested to clarify the support effect on the photocatalytic degradation activity of hydrophobic persistent organochlorines and found the structures of TiO_2 species on different composites were almost the same. According to the characterization results, it was reasonable to assume that the interaction between the hydrophobic reactant and the rather hydrophobic interlayer surface of fluorine mica was more favored in aqueous solutions. Furthermore, not only the hydrophobicity of the modified support but also the high surface area and relatively small pore size of layered silicate minerals were all significant factors in improving photocatalytic efficiency. Additionally, mica could serve as a highly reflective core of a novel ternary mica-titania@reduced graphene oxide (MT@rGO) composite to improve its light-harvesting capability [188]. As a result, the obtained MT@rGO-0.1 composite exhibited the best photocatalytic degradation performance of gaseous acetaldehyde, which is 2.5 times higher than that of the bare TiO_2 nanoparticles.

In addition, muscovite is a representative hydrated potassium-rich silicate mineral in the mica family and features highly perfect basal cleavage allowing it to split into thin transparent laminae. Zhou et al. synthesized N-doped nano-TiO_2/muscovite composites using urea as nitrogen dopant via the hydrolysis–precipitation method [189]. It was proved by XPS results that TiO_2 particles were coated uniformly on the muscovite surface by forming the Si–O–Ti and O–Ti–N bonds and interfacial Coulomb's force. The specific lamellar structure of muscovite endowed the composite with excellent dispersion in the aqueous solution of methyl orange, resulting in higher light absorption ability and improving the recycling efficiency of TiO_2 remarkably. Recently, Y. Li et al. applied a liquid precipitation method followed by thermal treatment to prepare TiO_2/muscovite composites and analyzed the effects of muscovite matrix on the crystal phase [190]. Their XRD results revealed that the muscovite matrix exerted a retarding effect on the growth and phase transformation of TiO_2. Moreover, the solid UV-vis diffuse reflectance spectrophotometry (UV-DRS) showed that muscovite matrix loading could reduce the band gap of TiO_2 and enhance light absorption ability. The synergistic adsorption effect between the muscovite matrix and TiO_2 could also promote h+ to oxidize adsorbed H_2O molecules into ·OH radicals, thus improving the photocatalytic efficiency of TiO_2/muscovite composites. A. Senthilnathan et al. could also design thin films of rice-like akaganeite deposited on the muscovite surface by the facile urea-assisted controlled self-assembly technique and investigate their photocatalytic activity under solar irradiation [191]. This study suggested that the adsorbed water molecules on muscovite surfaces had a major influence on the formation of hydroxyl radicals through their reaction with photo-excited holes or superoxide radicals on akaganeite/muscovite composite surfaces. Peng et al. integrated musco-

vite sheet/SnO_2 structure with g-C_3N_4-based photocatalytic cement and achieved improved photocatalytic performance [192]. They alleged that SnO_2 as an electron acceptor layer could promote interfacial charge transfer and prevent electron-hole recombination, while the muscovite sheets could assist in eliminating the mutual influence between the photocatalytic reaction and cement blocks as well as enhancing its stability. Recently, Bao et al. reported the synthesis of nano zerovalent iron-loaded muscovite composites via the liquid-phase reduction method and optimized its catalytic activity for P-chlorophenol decomposition under different reaction conditions [193]. They found that muscovite could significantly reduce the agglomeration degree of iron particles, increasing their dispersibility and catalytic activity of the composite. Aenthilnathan et al. prepared ZnO/muscovite composite using the surficial attractive forces of mica, and the presence of muscovite might promote the photodegradation efficiency by its adsorptive ability, enriching the pollutant concentration near the photocatalyst composite [194]. Moreover, muscovite modification could change the ZnO morphology from an oval shape to a flower-like structure and expose more reactive sites.

3.2.5. Illite-Supported Photocatalyst

As one of the most abundant natural clays contained in sedimentary rocks, illite belongs to the mica–phyllosilicates group and has a unique 2:1 sandwich framework of silica tetrahedron (T)–alumina octahedron (O)–silica tetrahedron (T) layers with rich hydrophilic aluminum hydroxyls. The hydrated potassium cations are generally localized in the space between the T-O-T layer sequence, which is responsible for its non-swelling property [195]. As a consequence, the cation-exchange capacity of illite is around 20–30 meq/100 g and lower than that of smectite.

Due to its specific structure and outstanding properties, illite has been widely used as support for various applications. It is reported that natural illite clay is usually applied as catalyst support for autothermal dry reforming of methane (DRM)-like nickel-containing Ce- or La-promoted catalysts, which is different from some common methods to improve DRM efficiency of Ni-containing catalysts [196–198]. Although iron impurity in natural illite tends to form $FeNi_3$ alloy, the formation of the britholite phase from the migration of lanthanum into the bulk could inhibit this alloy formation, preserving more active Ni particles available for methane activation. Additionally, a novel self-assembly Co_3O_4@illite composite has been successfully prepared by encapsulating the aggregation of Co_3O_4 nanospheres onto natural illite micro-sheets with abundant oxygen vacancies [199]. The catalytic performance of these composites was evaluated by decomposition of Atrazine(2-chloro-4-ethylamino-6-isopropylamino-1,3,5-triazine) via activation of peroxymonosulfate (PMS). The reaction rate constant determined according to the pseudo-first-order kinetic model of the Co_3O_4@illite composite was about 1.7 times better than that of bare Co_3O_4. The natural illite could not only promote Co_3O_4 nanosphere distribution but also regulate the grain size and crystallinity of Co_3O_4 nanospheres as well as the oxygen vacancies which originated from illite clay as the electron reservoir accelerates electron immigration from PMS to the catalyst surface. Additionally, Dong et al. could synthesize TiO_2/illite composites to explore the influence of pH value on this reaction system [37]. They found that TiO_2 particles were connected onto the illite surface via Si–O–Ti and Al–O–Ti bonding; thus, illite could effectively hinder the phase transition from anatase to rutile at high temperatures. Consequently, the catalytic activity of TiO_2/illite was slightly better than commercial TiO_2 at the optimal pH value of 1.5. On the other hand, the presence of illite in TiO_2/illite composites could evidently reduce the production cost without compromising any physical and chemical properties when applied in the pigment industry [200].

Due to its chemical composition and electronic structure, illite could be firmly dispersed on g-C_3N_4 surface via coordination bonds with bridging Si or Al ions of illite with N ions in g-C_3N_4 [201]. By virtue of its large specific surface area, abundant Lewis acid sites, and high electronegativity induced by ion substitution, the existence of illite could

introduce defects at the interface between g-C_3N_4 and illite and make the g-C_3N_4 sheets peel and roll up, increasing oxygen adsorption to generate more reactive oxygen species. The resultant self-built electric field in the composite could efficiently promote the separation of photogenerated charge carriers. Therefore, the removal efficiency of NO by g-C_3N_4/illite composite was 1.8 times higher than that determined for the pure g-C_3N_4.

3.2.6. Vermiculite-Supported Photocatalyst

Forming from the weathering or hydrothermal alteration of biotite or phlogopite, vermiculite is classified as a 2:1 type layered hydrous phyllosilicate mineral constituting two silica tetrahedral sheets which are bonded together with an alumina or magnesia octahedral layer. Therefore, it has abundant deposition, a large surface area, and good thermal and chemical stability, which makes it eligible to be an excellent adsorbent and catalyst carrier. Zhang et al. utilized natural paper-like vermiculite as a host photocatalyst to load CdS quantum dots and evaluated the photocatalytic hydrogen evolution activity of the as-prepared composite using Na_2S and Na_2SO_3 as sacrificial reagents under visible light irradiation [202]. The CdS/vermiculite composite with the optimal ratio of 5% exhibited the highest hydrogen generation rate of 92 μmol/h and the best apparent quantum efficiency of 17.7% at 420 nm. The improved photocatalytic activity and stability accounted for the synergistic effect between vermiculite and CdS induced by the well-matched overlapping band structure and thus accelerating charge carrier separation. Later, Wang et al. could successfully construct a three-dimensional $KNbO_3$/vermiculite composite via an in situ hydrothermal procedure [38]. They found that $KNbO_3$ nanoneedles were grown on the outer and inner surface of layered vermiculite and abundant active sites in the 3D framework are favorable for photocatalytic activity. Additionally, Zhu et al. could fabricate an efficient ternary AgI-Bi_2MoO_6/vermiculite adsorption-photocatalyst with superior photoactivity under visible light [39]. This composite showed high photodegradation efficiency of malachite green of about 98.89%, which was much better than that of Bi_2MoO_6 (54.89%) and Bi_2MoO_6/vermiculite (80.74%). These results were explained by the homogeneous distribution of AgI/Bi_2MoO_6 on the vermiculite surface, which increased adsorption ability and effective electron-hole separation. Moreover, vermiculite and bentonite have been used as photocatalysts to degrade sulfamethoxazole (SMX) and trimethoprim (TMP) under UV and solar illumination, and the photodegradation efficiency of SMX and TMP was enhanced by 11.4 and 46.4 times, respectively, after adding vermiculite [203]. These results were explained by the higher percentage of doping ions, such as Fe, Mn, and Ti, in the vermiculite than in the bentonite.

3.3. 3D Mineral-Supported Photocatalysts

3.3.1. Allophane-Supported Photocatalyst

As a natural clay mineral, allophane is a kind of amorphous or poorly-crystallized hydrous aluminosilicate belonging to the kaolin–serpentine group and varies remarkably in morphology from fine-rounded particles to irregular agglomeration. Generally, this mineral shares a 3.5–5 nm sized hollow spherical structure on which 0.3–0.5 nm sized defects are distributed [204]. It is reported that the hollow sphere walls consist of inner silica and outer alumina layers with a hydroxylated or hydrated surface, which is suggested to endow allophane with a significant ability to adsorb ionic or polar pollutants from the gaseous and aqueous phases due to its amphoteric ion-exchange activity and large specific surface area. Allophane's structure is convenient for even dispersion in host photocatalyst materials and efficient electron transport on the surface [205].

In 2011, highly-adsorptive allophane/TiO_2 composite synthesized by the sol-gel method achieved even distribution of small clay particles on TiO_2, inhibited the emission of intermediate products efficiently, and then degraded gradually during the degradation of trichloroethylene [206]. Compared with the mechanical mixing sample of allophane/

TiO_2, the final product's CO_2 concentration produced from the allophane/TiO_2 nanocomposite was three times higher due to the homogeneous dispersion of allophane into TiO_2. As an amorphous silica source, allophane was selectively dissolved by acid treatment and mixed with TiO_2 at various mass ratios [207]. It was found that the photocatalytic activity evaluated by gaseous acetaldehyde degradation was improved with over 5 mass% mixing ratio of allophane despite the specific surface area decrease. When the mixing ratio of allophane reached 20 mass%, its photocatalytic activity calculated by the CO_2 generation rate increased to 1.8 times higher than non-treated TiO_2. Additionally, the selective leaching of alumina from allophane could leave microporous or mesoporous silica structures, which evidently increase the adsorption capacity and accelerate the photocatalytic acetaldehyde decomposition of the as-prepared TiO_2/silica composite. Recently, allophane was applied as support for heterojunction Bi_2WO_6/$CeVO_4$ photocatalyst via hydrothermal synthesis combined with mechanical mixing [208]. As illustrated in Figure 9b,c, SEM results suggest that Bi_2WO_6/$CeVO_4$/allophane composites consist of flake-spherule allophane particles and $CeVO_4$ nanocrystals dispersed on the hierarchical flower-like Bi_2WO_6 microspheres. According to its photocatalytic performance, the Bi_2WO_6/$CeVO_4$/ allophane composite with the 1:1 mass ratio of Bi_2WO_6: $CeVO_4$ showed the highest photocatalytic activity, and the $CeVO_4$ worked as a photosensitizer to absorb more photons from visible light in this reactant system. The enhancement in the photocatalytic activity of the Bi_2WO_6/$CeVO_4$/allophane composite was presumed to result from a certain extended light absorption range, and the construction of heterojunction, as well as the mineral support, could separate photogenerated electron-hole pairs more efficiently.

3.3.2. Pyrophyllite-Supported Photocatalyst

As a relatively rare clay, pyrophyllite is a layered hydroxy aluminosilicate with a dioctahedral 2:1 structure, as shown in Figure 9a. Its crystal structure is described as being composed of Al-O(OH) octahedral sheets sandwiched between two tetrahedral SiO_4 sheets, with each octahedral Al bonded with a tetrahedral Si by an apical O and with an adjacent Al by two OH groups [209]. Generally, pyrophyllite exhibits excellent physicochemical characteristics, such as low thermal expansion and high reheating stability. Some studies utilize modified pyrophyllite clay as an efficient catalyst for the catalytic wet peroxide oxidation technique, which is an important technique in advanced oxidation processes. Taking phenol as target pollutant, pyrophyllite is impregnated by 2.5 wt% copper content to achieve total phenol degradation and 80% total organic carbon reduction in the presence of H_2O_2 during 4 h at optimized conditions [210]. The as-obtained Cu-supported pyrophyllite was proved to have better stability and detoxification properties with an obvious low copper leaching concentration. Additionally, pyrophyllite/TiO_2 heterostructures could also degrade over 89% of a phenol solution after 2 h with obviously improved stability [51]. The latter study showed that the methanol washing process could reduce the defect sites and raise the specific surface area from 16.58 $m^2 \cdot g^{-1}$ to 56.39 $m^2 \cdot g^{-1}$, which effectively decreases the photoexcited e^-/h^+ recombination rate. However, there are just limited works on pyrophyllite clay in the photocatalysis field due to its rarity.

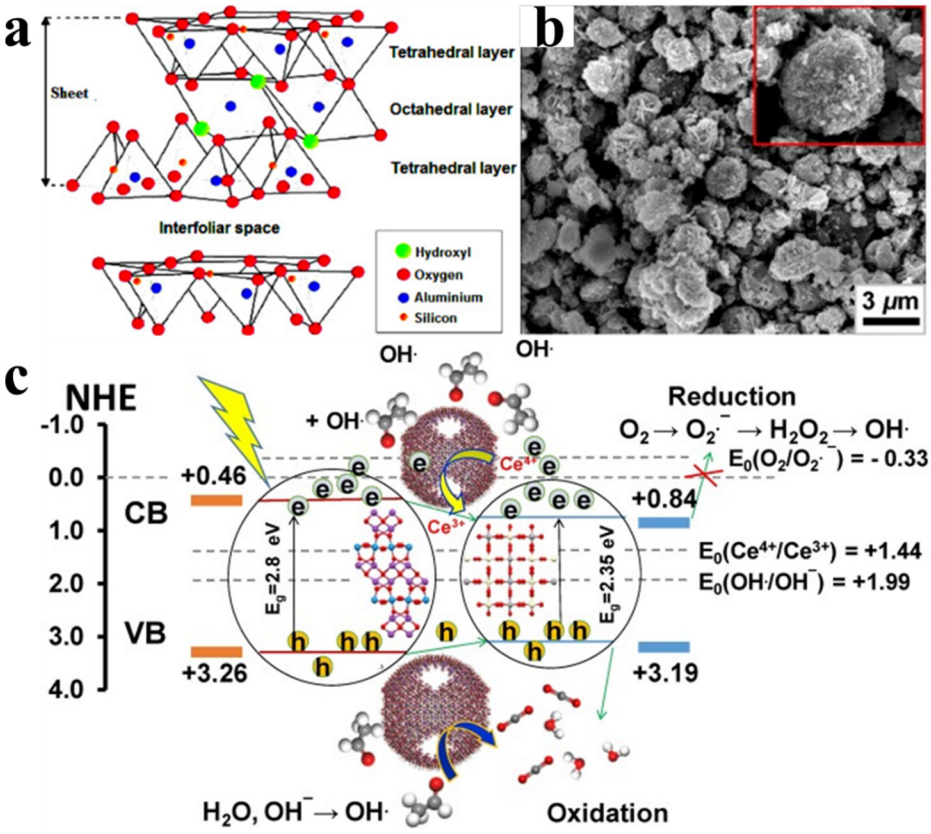

Figure 9. (**a**) Structure of pyrophyllite; (**b**) SEM images of the $Bi_2WO_6/CeVO_4$/allophane composite photocatalysts synthesized with 1:3 of Bi_2WO_6:$CeVO_4$; (**c**) schematic representation of the possible mechanisms of acetaldehyde photodegradation over the $Bi_2WO_6/CeVO_4$/allophane composite under visible–light irradiation. Adapted with permission from Ref. [51]. Copyright 2018, Elsevier B.V; Adapted with permission from Ref. [208]. Copyright 2017, Elsevier B.V.

3.3.3. Perlite-Supported Photocatalyst

With main components as alumina and silica, perlite is an amorphous volcanic vitreous rock lava containing crystal water and has porosities of over 95% as well as a density of 64–144 kg/m^3. When heated at the temperature range of 700–1200 °C, perlite has a volume expansion of up to 20-fold of the original one, which induces largely reduced density and porous structure, allowing it to stay afloat on the solution surface. As a result, this modified perlite, also named expanded perlite, is considered an excellent adsorbent and support material for immobilization of photocatalysts owing to its chemical inertia and adequate light transparency to provide the passage of photons [211]. M. Długosz et al. coated TiO_2 particles onto perlite granule surfaces to obtain a floating photocatalyst composite [212]. This TiO_2/perlite composite possessed a better solar light adsorptive ability and excellent photocatalytic degradation efficiency for phenol. Xue et al. prepared B-N co-doped TiO_2/expanded perlite composite with a mesoporous structure and high specific surface area (99.23 m^2/g), exhibiting more efficient photocatalytic activity that was five times higher than TiO_2/expanded perlite [213]. Song et al. loaded expanded perlite with amorphous Al_2O_3 as a porous floating carrier for g-C_3N_4, and they found that this floating photocatalyst composite could not only inactivate algal cells but also decompose the released organic matter as well as achieve 74.4% of the photocatalytic Microcystis aeruginosa inactivation efficiency [214]. It was elucidated that Al_2O_3 could promote the adsorption process and improve the photogenerated charge carrier separation efficiency of g-C_3N_4. The existence of perlite was proved to effectively suppress g-C_3N_4 agglomeration in solution so that there are more dissolved oxygen molecules for g-C_3N_4 to produce radicals. Khan et al. could successfully construct a floating cabbage-like Bi-Bi_2S_3-Bi_2WO_6@ex-

panded perlite photocatalyst composite which could decompose methyl orange and Rhodamine B completely in 25 min [215]. The expanded perlite furnishes the Bi-Bi_2S_3-Bi_2WO_6@expanded perlite photocatalyst with a mesoporous framework to promote the efficient adsorption of aqueous contaminant solutions. Considering the remarkable properties of $CuFeO_2$ semiconductor, Darkhosh et al. decorated $CuFeO_2$ onto expanded perlite to optimize its electronic structure and narrow the band gap energy to 1.81 eV [216]. They found that the combination of $CuFeO_2$ and perlite could increase the surface area of perlite from 2.302 $m^2 \cdot g^{-1}$ to 142.32 $m^2 \cdot g^{-1}$ and the pore volume from 0.0044 $cm^3 \cdot g^{-1}$ to 0.214 $cm^3 \cdot g^{-1}$. In this binary system, expanded perlite works as an electron sink that could attract the photogenerated electrons from $CuFeO_2$ to reduce the electron-hole recombination rate. The floating property of expanded perlite provides $CuFeO_2$/expanded perlite composites with better stability and organic dye mineralization efficiency. The oil spill problem is detrimental to aquatic wildlife and the ecological environment. As a result, Qiu et al. designed a honeycomb-like BiOI/expanded perlite photocatalyst nanocomposite to treat diesel wastewater using its outstanding adsorptive and photocatalytic performance [217]. This excellent BiOI/expanded perlite composite could achieve a diesel removal efficiency of 85% after 2 h under sunlight irradiation, and it could be reused at least five times. Moreover, the presence of expanded perlite could decrease the toxicity of BiOI and facilitate the recollection of the photocatalyst composite after application.

As low-cost and sustainable support, the silanol hydroxyl groups on perlite surfaces are favorable for bonding with other photocatalytic materials. Perlite could easily suppress the aggregation problem of photocatalysts and advance the floating property of the designed photocatalyst.

3.3.4. Quartz-Supported Photocatalyst

As the second most abundant mineral in Earth's continental crust, quartz belongs to weathering rock, with the chemical formula of SiO_2 [218]. Silicon and oxygen atoms in quartz are linked in a continuous framework of SiO_4 tetrahedra, with each oxygen shared between two tetrahedra. Unlike other clay minerals, most photocatalysts are deposited onto quartz substrate to avoid separation step by centrifugation. Generally, quartz support could not modify the properties and crystalline structure of photocatalysts themselves. Additionally, UV-transparent quartz is beneficial for assisting the light absorption process of photocatalysts. A. Okemoto et al. could load a 50 nm picene thin film onto quartz to acquire very high hydrogen production activity using sacrificial agents under light irradiation [219]. The TiO_2 support quartz fiber filter could efficiently degrade atmospheric fine particulate matter (PM2.5) under UV irradiation and provide a significant increase in CO_2 production [220]. The as-prepared fiber exhibits an obvious capillarity effect beneficial for photocatalytic reaction. Moreover, Zhang et al. synthesized $Gd_2Ti_2O_7$ supported on quartz spheres and realized remarkable enhancement of photocatalytic ofloxacin degradation efficiency, which could be attributed to the smaller crystallite size and larger specific surface area [221]. Furthermore, although quartz is an insulator, Li et al. found H_2 produced from CH_3OH-H_2O aqueous solution at the quartz surface under light [222]. They suggested that the surface states of quartz located between the band gap might act as electron acceptors and hence successfully produce H_2 from the CH_3OH-H_2O solution. Additionally, quartz is also regarded as an SiO_2 source to prepare target photocatalyst composites [223]. However, quartz as photocatalyst support still has limited research interest and a long way to go.

3.3.5. Bauxite-Supported Photocatalyst

As the main aluminium and gallium source worldwide, bauxite belongs to a lateritic sedimentary rock with a relatively high aluminium content. It is considered as a naturally reddish heterogeneous material mostly consisting of the gibbsite boehmite and diaspore minerals mixed with goethite and hematite, kaolinite, and small amounts of anatase TiO_2

and ilmenite. In 2010, a novel low-cost photocatalyst was synthesized for hydrogen production from water-based bauxite residue material [224]. According to this work, this catalyst reached a 20.85 μmol/h/g hydrogen generation amount under visible light and exhibited excellent physical and chemical stability. Later, Ismail et al. used Malaysian bauxite to explore the calcinating temperature effect on its composition and resultant photocatalytic activity [225]. They found that heat-treated bauxite catalysts had low band gap energy (2.04 eV), and the sample processed under 800 °C could exhibit the best photocatalytic performance, degrading 75% of Reactive Black 5 dye after 6 h of UV and visible light exposure, due to its smaller particle size. It was concluded that bauxite, after heat treatment, possessed a heterostructure photocatalyst allowing fast electron transport and an electron-hole recombination rate decrease.

3.4. Porous Mineral-Supported Photocatalysts

3.4.1. Diatomite-Supported Photocatalyst

Diatomite, also named kieselguhr, is a naturally occurring soft and porous siliceous sedimentary rock and mainly consists of amorphous silica and small quantities of alumina and iron oxide [226]. Diatomaceous earth is originated from the skeleton fossils of dead microscopic single-celled algae known as diatoms. Generally, as depicted in Figure 10a, natural diatomite has a unique, highly ordered porous structure and many superior characteristics, such as high porosity, low density, high adsorption capacity, etc. Accordingly, it has been widely used as a filtration aid, adsorbent, and catalyst support. Up to now, natural diatomite is still widely used as a support material for various photocatalysts for different applications, which can be seen in Table 3. For instance, S. K. Padmanabhan et al. could deposit TiO_2 nanoparticles on diatomite surfaces, which showed good photocatalytic degradation of Rhodamine B, following pseudo-first-order kinetics [227]. Due to its higher surface area and mesoporous structure, diatomite worked as a host matrix for TiO_2 particles to realize uniform distribution and smaller TiO_2 crystalline size. Xia et al. also found that the anatase-to-rutile phase transition temperature was retarded to nearly 900 °C after loading onto the diatomite surface [228]. The pre-treatment of diatomite in phosphoric acid could modify its surface features and further increase the Si–O–Ti bonding strength between TiO_2 and diatomite, suppressing TiO_2 grain growth via remaining P species. As a result, it is favorable for the thermal-stable meso-porous structure formation at the granular spaces level, which could effectively promote the charge and mass transfer efficiency. Later, Zhang et al. applied TiO_2/diatomite composite to degrade volatile organic compounds and optimized its relative humidity level and reaction atmosphere for different ketone and alcohol degradation processes [229]. The optimal relative humidity is reported to be positively related to the carbon chain length of volatile organic compounds with the presence of oxygen. Additionally, Wu et al. utilized a TiO_2/diatomite catalyst to solve the serious secondary pollution problem of non-thermal plasma technology in reducing the polycyclic aromatic hydrocarbons emission process [230]. They stated that the TiO_2/diatomite composite works as the catalyst packing of dielectric barrier discharge reactor and improves naphthalene conversion up to 40% and CO_x selectivity up to 92%, and the aerosol and secondary volatile organic compound formation are substantially reduced by nearly 90% and 100%, respectively. They suggested that the synergetic effect between the TiO_2/diatomite catalyst and plasma could intensify the electron energy in the dielectric barrier discharge reactor and activate the deep oxidation of polycyclic aromatic hydrocarbons without external heating. Moreover, the Al_2O_3 component in diatomite support could exert a considerable effect on decomposing O_3 into O for naphthalene conversion and CO_x formation. Then, Barbosa et al. introduced Fe_2O_3 into heterogeneous diatomite/TiO_2 composite to achieve easy recovery without any significant activity loss under an external magnetic field [231]. It is known that the self-aggregation of g-C_3N_4 severely inhibits its photocatalytic performance. As a result, porous micro-disk-like diat-

omite could effectively suppress its self-aggregation process by acting as a low-cost photocatalyst carrier via the treatment presented in Figure 10b [232]. The g-C_3N_4/diatomite composite could display excellent selective adsorption ability, and photocatalytic activity for methylene B removal in mixed dyes, where the multi-interface produced between diatomite and g-C_3N_4 could dramatically accelerate electron migration. In 2020, Liu et al. decorated diatomite with Ni/NiO nanoparticles for the photoreduction of malachite green dye and Cr(VI) under visible light irradiation [233]. The synthesized composite was characterized as having a higher surface area of 400 m^2/g and lower band gap energy of 1.71 eV, as well as the improvement of malachite green dye and Cr(VI) photodegradation percentages by 56.5% and 53%, respectively, compared with Ni/NiO nanoparticles. These could be ascribed to the fact that diatomite provides high exposed surface area for the incident photons, and Ni integration reduces the band gap energy. S. Tajmiri et al. could incorporate cadmium sulfide onto diatomite substrate to solve its recycling problem and obtain better adsorptive ability [234]. They found that the methylene B and Cr(VI) reduction process could be better simulated by the pseudo-first-order kinetic model, which means the adsorption and photodegradation process are controlled by diffusion and chemical reaction, respectively. Furthermore, Hua et al. combined $BiVO_4$@diatomite composite with microcrystalline cellulose and PVB ethanol solution to prepare the visible-light responsive photocatalytic paper by electrospinning [235]. The optimal $BiVO_4$@diatomite/MCC/PVBCFs (3:3:4) fibers are reported to be able to degrade 66.8% and 56.8% of methylene B and HCHO after 4 h visible light illumination as well as have excellent physical properties, such as tightness of 0.482 g/cm^3 and tensile index of 11.28 $N{\cdot}m{\cdot}g^{-1}$. More recently, several diatomite-based photocatalysts have been developed that showed high photocatalytic efficiencies for the degradation and reduction of different pollutants, shown in Table 3.

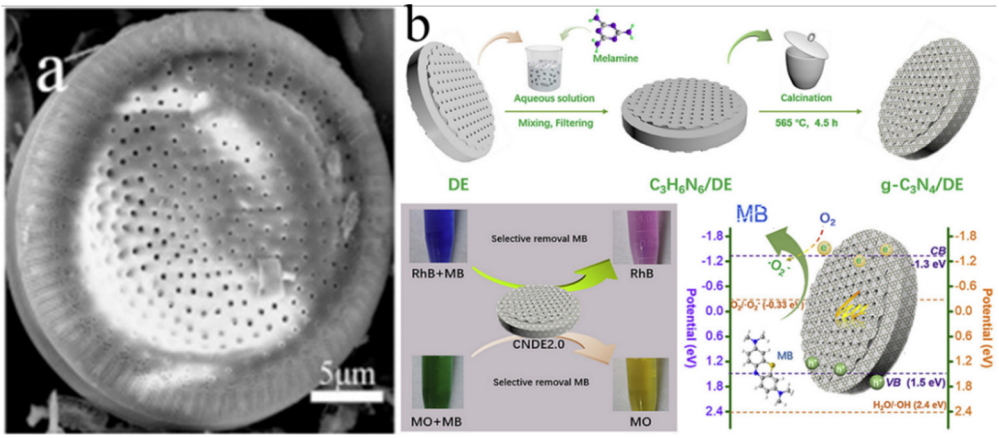

Figure 10. (**a**) SEM images of raw diatomite sample; (**b**) schematic of the fabrication of g−C_3N_4/diatomite composites. Photos of selective removal of various dyes. Proposed reaction mechanism for methylene blue (MB) decomposition over g−C_3N_4/diatomite−2.0 photocatalyst. Adapted with permission from Ref. [226]. Copyright 2018, Elsevier B.V; Adapted with permission from Ref. [232]. Copyright 2019, Elsevier B.V.

In summary, natural diatomite clay exhibits great potential in the photocatalysis field due to its outstanding properties and abundant availability and might play a different role in future industrial applications.

Table 3. Applications of various photocatalysts using natural diatomite as support material.

Photocatalyst	Method	Application	Light Source	Photocatalytic Efficiency (%)	Refs.
Nb_2O_5@diatomite	Hydrothermal	Photoreduction of Cr(VI)	500 W mercury lamp	94.50	[226]
TiO_2-diatomite	Thermal hydrolysis and annealing method	RhB	300 W UV lamp	--	[227]
TiO_2-diatomite	Sol-gel and calcination or phosphoric acid pre-treatment	MO	250 W mercury lamp and 300 W white light lamp	90 and 60	[228]
Diatomite/Fe_2O_3/TiO_2	Co-precipitation and impregnation method	MB	300 W xenon lamp	99	[231]
g-C_3N_4/diatomite	Calcination	MB	350 W xenon lamp	90	[232]
Diatomite @Ni/NiO	Acid leaching and in situ reduction method	MG and Cr(VI) photoreduction	400 W metal halide lamp	almost 100	[233]
CdS @diatomite	Biological synthesis using Bacillus licheniformis	MB and Cr(VI) photoreduction	360–450 nm UVA lamp	over 90	[234]
$BiVO_4$ @diatomite/microcrystalline cellulose/PVB composite fibers	Hydrothermal and electrospinning method	MB and HCHO)	250 W high pressure mercury lamp	66.80 and 56.80 for MB and HCHO	[235]
BiOCl/diatomite	Hydrothermal	TH and gaseous HCHO	300 W over 420 nm xenon lamp	91.02 and 63.01 for TC and HCHO	[236]
BiOCl/diatomite	Hydrolysis	CIP	300 W 320–780 nm xenon lamp	94	[237]
Magnetic g-C_3N_4/diatomite/Fe_3O_4	An electrostatic self-assembly method	RhB	500 W over 420 nm xenon lamp	98	[238]
Ag_3PO_4/Fe_3O_4/diatomite	Hydrothermal	*E. coli* and RhB	500 W xenon lamp	100 and 98 for *E. coli* and RhB	[239]
TiO_2/ZnO/diatomite	Two-step precipitation	MB	30 W xenon lamp	80.34	[240]
Bi_2MoO_6 modified TiO_2/diatomite	Hydrothermal	HCHO	300 W over 400 nm xenon lamp	96.32	[241]
ZnO/$ZnFe_2O_4$/diatomite	Hydrothermal-precipitation	OTC	300 W xenon lamp	95	[242]
Fe_2O_3/TiO_2/diatomite	Chemical precipitation-calcination	CIP	300 W over 420 nm xenon lamp	88	[243]
Fe-g-C_3N_4/diatomite	Thermal polymerization	TC	500 W xenon lamp	98.3	[244]
Ag_3VO_4/g-C_3N_4/diatomite	Annealing-precipitation	Cr(VI)	500 W over 420 nm xenon lamp	70	[245]
Fe_3O_4@TiO_2/diatomite	Sol-gel and ultrasound assisted reflux technique	TC	500 W high-pressure mercury-vapor lamp	97	[154]
TiO_2/recycled diatomite	Acid leaching and alkaline treatment	HCHO	300 W xenon lamp	95.59	[246]

3.4.2. Zeolite-Supported Photocatalyst

As a microporous hydrated aluminosilicate mineral commonly used as a commercial adsorbent and catalyst, natural zeolite is believed to be a mixture of volcanic rocks and ash layers reacting with alkaline groundwater [247,248]. Generally, it consists of silicon and aluminum, which are arranged in tetrahedral coordination with oxygen atoms. However, some Si^{4+} in the SiO_2 network could be replaced by Al^{3+}, which leads to a negatively charged surface. As a result, various cations can be accommodated into the zeolite framework and loosely held, resulting in easy ion exchange. Early in 2012, M. Takeuchi et al. utilized Y-zeolite, faujasite zeolite with a structural silica-to-alumina ratio over 3, to construct a TiO_2/zeolite hybrid photocatalyst to achieve efficient gaseous toluene and benzene

removal [249]. They found that these aromatic compounds were concentrated within the hydrophobic zeolite cavities due to the weak interaction with silanol groups on the zeolite surface, which enabled their better distribution onto TiO_2 surface. Zhang et al. modified zeolite by acid leaching and hybridized it with TiO_2 via hydrolysis deposition [186]. It was found that the anatase titania nanoparticles with a crystallite size of about 16 nm could be stabilized by the acid leaching of the zeolite surface. Moreover, acid leaching of zeolite surface could increase surface area, generate more surface hydroxyl groups, and provide a better dispersion effect. Later, Kovalevskiy et al. prepared a TiO_2/zeolite composite from a $TiOSO_4$ precursor for photocatalytic oxidization of volatile organic compounds [250]. They reported that zeolite, as TiO_2 support, could evidently enhance the adsorption capacity of the composite and effectively decrease the concentration of intermediates by suppressing their desorption on the photocatalyst surface during the heterogeneous photocatalytic oxidation process. Combining FeS with Fe_2O_3 to form a heterojunction semiconductor onto the surface of clinoptilolite nanoparticles could also show good photocatalytic activity [251]. The optimum ratio of FeS/Fe_2S_3 synthesized from 0.1 mol/L Fe(II) and 0.15 mol/L Fe(III) solution exhibited the best performance for ciprofloxacin photodegradation, where the electric field of the zeolite framework played an important role in photogenerated electron-hole separation, and hence, obviously improved photocatalytic activity. Additionally, Rajabi et al. took magnetic F_3O_4 as a core and coated it with a mordenite zeolite shell and CuO shell [252]. It was shown that the presence of mordenite zeolite could broaden the visible light absorption ability and enable stability in photocatalytic activity. Moreover, this magnetic core could realize easy separation and recycling of the as-prepared photocatalyst under an external magnetic field. In addition to natural zeolite, Nassar et al. prepared a zeolite nanostructure hydrothermally and modified its morphology and crystallite size by using different aluminum sources [248]. It was exhibited that the produced zeolite using aluminum isopropoxide possessed the optical energy band of 3.29 eV and BET surface area of 20.18 m^2/g. This composite could degrade 85% of methylene B after 180 min under UV light irradiation, which followed the pseudo-first-order model. Owing to ion-exchange capacity and surface and structure properties, zeolite is gaining more and more attention in various industrial applications.

3.4.3. Pumice-Supported Photocatalyst

Originating from violent eruptions from volcanos under high temperature and pressure, pumice appears as porous silica rock and consists of highly vesicular rough-textured volcanic glass. Due to the existence of abundant hydroxyl groups on the surface and unique porous structure, pumice has been mainly applied as a support for various photocatalysts. For instance, Yusuff et al. prepared ZnO/pumice composite that was used as a photocatalyst to treat dye-containing textile industry wastewater [253]. It was ascertained that the degradation reaction kinetics of the as-prepared ZnO/pumice composite agree well with the pseudo-first-order approximation of the Langmuir–Hinshelwood model. Additionally, the ternary Fe_3O_4/ZnO@pumice composite showed good photocatalytic activity for methylene blue degradation under different conditions [254]. The intrinsically magnetic property of natural pumice with Fe_3O_4 nanoparticles facilitates the convenient recovery of the composite, and the metallic particles are well integrated into the porous pumice laminates. As a result, the specific surface area of Fe_3O_4/ZnO@ pumice composite decreases from 41.7 to 32.3 m^2/g due to the partial loading of Fe_3O_4 and ZnO particles onto pumice pores. Through these works, natural pumice presents numerous promising possibilities in industrial applications.

4. Natural Carbonate or Carbon-Based Mineral-Supported Photocatalysts

4.1. Calcite-Supported Photocatalyst

As the most stable polymorph of calcium carbonate, calcite is extremely common in sedimentary, metamorphic, and igneous rocks throughout the world and is thus considered a rock-forming carbonate mineral. In 2019, Belhouchet et al. made full use of the natural Algerian shale abundantly existing in northeastern Algeria and North Africa to search for highly efficient photocatalytic material [41]. The study results revealed that the natural mineral mainly consisted of calcite coated with TiO_2 by the sol-gel method, and the composite CAL30 sample, had the largest pore volume, higher specific surface area, and, therefore, the best photocatalytic activity. It was analyzed that this calcite/TiO_2 system followed a pseudo-first-order kinetic model from the photocatalytic experiment results. The introduction of the mineral into CAL30 sample could suppress the electron-hole recombination and reach a close tetracycline degradation performance (the rate constant $k = 2 \times 10^{-2}$ min^{-1}) of pure TiO_2, saving 70% of the TiO_2 amount.

Additionally, limestone and marble generally make up the Earth's crust, a significant part with primary constituent as calcite, and serve as one of the largest carbon storages on this planet. Generally speaking, limestone as sedimentary carbonate rock is often formed by the skeletal fragments of marine organisms and the chemical precipitation of calcium carbonate. Because of the water solubility, weak acid properties, and wide distribution, limestone is usually used as a building material, white pigment, and product filler [255]. However, regardless of whether it is a building material or wall painting material, limestone always encounters a cleaning problem. As a result, self-cleaning technology design is put forward to solve this issue economically and efficiently. In 2017, N. Fadhilah could successfully synthesize super-hydrophilic self-cleaning limestone coating paint with TiO_2 nanoparticles modified by dispersant polyethylene glycol 6000 (PEG6000) [256]. This new paint with the composition of TiO_2:PEG600 as 1:6 could achieve the highest self-cleaning ability (83.1%) with water contact angles of 7°. Up to 2019, Mohsen et al. prepared $CaCO_3$/TiO_2 nanostructures with high surface area, mesoporous structure, and lower bang gap energy of 2.05 eV by the precipitation method [257]. Thus, the $CaCO_3$/TiO_2 nanocomposite showed photocatalytic desulfurization of 95% dibenzothiophene under 550 Watt linear halogen lamp illumination and in the presence of H_2O_2 and acetic acid.

Often referred to as magnesium-rich limestone, dolomite is known as an anhydrous carbonate mineral composed of calcium magnesium carbonate and crystallizes in the trigonal-rhombohedral system. With the ideal formula $CaMg(CO_3)_2$, dolomite has double carbonate-containing alternating planes of Ca^{2+} and Mg^{2+} ions. In 2019, Belarbi et al. calcined dolomite under 800 °C and then modified it by $Ca(NO_3)_2$ to obtain the dolomite-based catalyst CaD800, which could degrade 95% pentachlorophenol under UV light irradiation after only 1 h [258].

4.2. Other Carbon Material-Supported Photocatalyst

Apart from graphene, other carbon materials with specific morphology are also excellent candidates for photocatalyst support, such as carbon quantum dots, carbon nanotubes, carbon nanofibers, etc. [259]. Similar to graphene, these carbon nanomaterials also possess superior mechanical and electrical properties. In one benzene mineralization study, carbon nanotubes were combined with TiO_2 by the wet impregnation method. Carbon nanotubes as support could provide a stable electron reservoir and efficient electron transfer route. Moreover, the existence of carbon nanotubes effectively suppresses the agglomeration of TiO_2 particles, and thus more reactive sites could be exposed. Compared with the bare TiO_2, the enhanced photocatalytic performance of TiO_2/CNT composite was proved to come from tight interfacial contact between carbon nanotubes and TiO_2. Due to all these factors, the conversion efficiency from benzene to CO_2 over TiO_2/CNT is much higher than P25, a kind of commercial TiO_2 [260].

5. Natural Sulfate or Sulfide Mineral—Supported Photocatalyst

5.1. Gypsum-Supported Photocatalyst

As the most common sulfate mineral, gypsum is a soft calcium sulfate dihydrate compound that is often used as a fertilizer and as the main constituent in many forms of plaster, blackboard, and drywall. Generally, gypsum deposited from lake, sea, and hot springs crystallizes as a translucent crystal of selenite and forms as an evaporite mineral and hydration product of anhydrite. The previous research mainly focuses on assembling efficient photocatalytic additives with commercial gypsum to develop self-cleaning building materials and exploring their photodegradation efficiency on various pollutants. A novel $BiOCl_xBr_{1-x}$@gypsum heterojunction composite was constructed as a self-cleaning surface for building material [261]. The photocatalytic activity results showed that the as-obtained hybrid material could mineralize RhB in 4 min and the recalcitrant Naphthalene contamination in 20 min under visible light irradiation. Additionally, it could maintain superior photocatalytic activity and efficiency for at least 7 months. Janus et al. incorporated N, C co-modified TiO_2 into commercial gypsum to obtain a self-cleaning property and exhibit obvious dye removal capacity [262]. They found that N, C-TiO_2 photocatalyst functioned as the void space fillers in gypsum matrix could reduce gypsum particle size and over 10% mass content of N, C-TiO_2 additive into gypsum causes a considerable decrease of the compressive strength value, pore volume, and specific surface area. The obtained N, C-TiO_2/gypsum sample treated at 300 °C exhibited 85% and 70% degradation of azo dye Remazol red 198 after 15 h of UV and visible light irradiation, respectively. V. Binas et al. fabricated photocatalytic cement-based coating mixed with Mn-doped TiO_2 and compared the influence of different supporting materials on the photocatalytic activity against NO air pollutants [263]. The substrate materials displayed a slight difference in photocatalytic degradation efficiency, and the mixture of Mn-doped TiO_2 composite coating influenced its surface area and porosity.

5.2. Pyrite-Supported Photocatalyst

As a naturally n-type semiconductor material, pyrite is a brass-yellow sulfide mineral with metallic luster and chemical formula of FeS_2. Considering its broad existence in igneous, metamorphic, and sedimentary rocks worldwide, pyrite is widely regarded as a promising candidate for wastewater treatment. Diao et al. employed pyrite as a photocatalyst for the degradation of malachite green (MG) and Cr(VI) reduction [264]. Pyrite photocatalysts showed removal efficiency of MG and Cr(VI) reached 96.2% and 53.1%, respectively, from their mixture solution after 120 min UV light irradiation, which is better than that determined for individual separated solutions. They suggested that the presence of malachite green could accelerate Cr(VI) reduction and vice versa, which is attributed to the synergistic effect in the MG and Cr(VI) coexistence system. They also found that the dissolved oxygen could remarkably promote MG degradation efficiency and Cr(VI) reduction that is mainly controlled by direct electrons of pyrite. Furthermore, natural pyrite could be applied to inactivate Escherichia coli in the presence of citrate and EDTA as chelating agents [265]. These chelating agents would increase the iron solubility and reduce the oxidation of the pyrite surface, which promotes the photo-Fenton process and the E. coli inactivation rate. Additionally, natural pyrite could be transformed structurally into a Z-scheme FeS_2/Fe_2O_3 composite via the heat treatment method, and the synergistic effects between FeS_2 and Fe_2O_3 have a remarkable positive influence on its photocatalytic activity [266]. It was proved that the as-obtained composite exhibits increased photocatalytic degradation efficiency from 36% to 65% with the presence of 30 mg/L Cr(VI), and the addition of Cr(VI) ions can also be almost reduced. That is related to the fact that Cr(VI) could capture the electrons and thus improve photo-induced electron-hole pair separation efficiency. These findings make natural pyrite suitable for designing a low-cost and efficient photocatalyst for wastewater treatment and environmental applications.

6. Natural Special Mineral-Based Photocatalysts

6.1. Ilmenite-Based Photocatalyst

As a wide-bandgap anti-ferromagnetic semiconductor, ilmenite is known as a titanium–iron oxide mineral with the idealized chemical formula $FeTiO_3$, containing around 40–60% of TiO_2. Generally, pure ilmenite has a rhombohedral crystal structure with the hexagonal packing of the oxygen atoms with cations occupying two-thirds of the octahedral positions, where Fe and Ti occupy alternating layers, as illustrated in Figure 11A,B [267]. Due to its chemical composition and unique properties, ilmenite is always considered the most suitable natural precursor of photocatalyst TiO_2. A. Simpraditpan et al. explored the effect of calcination temperature on the properties of titanate nanofibers originated from natural ilmenite minerals and concluded that the temperature increase could result in the phase transformation from thermodynamically metastable anatase phase to the most stable rutile phase with increasing the crystallite size [268]. They found that the nanofibers calcined at high temperatures of 600–1000 °C were mixtures of three crystalline phases, e.g., anatase, rutile, and Fe_2O_3. Moreover, increasing the calcination temperature induces the increase of crystallite sizes, therefore leading to the absorption edge of the as-synthesized sample shifts to the visible light region. Among these samples, the nanofibers calcined at 400 °C for 2 h exhibited the best photocatalytic activity, even higher than the commercial TiO_2. Shao et al. synthesized iron-doped TiO_2 nanorods from raw ilmenite ore via a direct acid leaching method. They found that the band gap energy decreased from 2.94 eV to 2.49 eV with higher iron concentration, as compared with 3.02 eV of bare rutile TiO_2 [269]. The optimal amount of iron dopant was reported to be 1.69%, leading to the best photogenerated charge carrier separation efficiency. Another study showed that iron species from natural ilmenite minerals could be converted into Fe_3O_4 in addition to titania phases, providing magnetic recyclability of the photocatalyst under an external magnetic field [270]. This composite was characterized to be composed of face-centered cubic Fe_3O_4 and body-centered tetragonal anatase TiO_2 with superparamagnetic behavior and strong visible-light absorption ability. It could be separated and recycled quickly and easily due to the magnetization effect of Fe_3O_4 core. Moreover, superoxide radicals were proved to be the main active species of the Rhodamine B degradation process. Xia et al. introduced persulfate into the natural ilmenite reaction system to achieve efficient E. coli inactivation under visible light irradiation [271]. They suggested that persulfate could repress the photogenerated electron-hole recombination, and the Fe(II) species from ilmenite can be beneficial for persulfate activation and thus promote reactive radical production like singlet oxygen ($^1O_2$), which was investigated to be the primary bactericidal agent, according to the reaction routes drawn in Figure 11C. Lee et al. investigated the effect of the iron contents in ilmenite on its photocatalytic activity. The acid concentration was able to control the iron content during the acid leaching process [272]. The optimum iron content was found to be 1.62 at% after pre-treatment with 25 *v*/*v*% HCl, and hence, it was able to achieve complete removal of the Reactive Black 5 dye within 30 min of visible light illumination owing to obvious surface area increase and low photogenerated electron-hole recombination rate. In addition, natural ilmenite also was applied as a photocatalyst for selective reduction of nitrate using oxalic acid as a reducing agent and hole scavenger, enabling the complete removal of N_2 from the nitrate solution [273]. At the present stage, ilmenite is regarded as the most suitable and promising candidate to realize the cost-effective production of TiO_2 and its commercialized application.

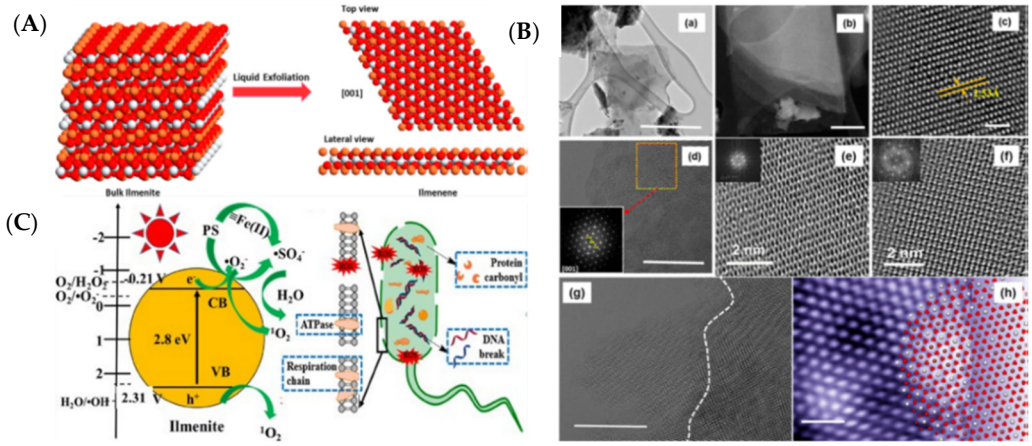

Figure 11. (**A**) Liquid exfoliation of bulk ilmenite (left) into the most stable [001] oriented 2D monolayers (right). A planar view (right top) and a cross-sectional view (bottom right) of the monolayer are shown. White, brown, and red colors denote Ti, Fe, and O atoms, respectively; (**B**) 2D morphology: (**a**) bright-field TEM images (scale bar of 0.5 μm) showcasing monolayer and bilayer ilmenene sheets; (**b**) dark-field TEM images (scale bar of 0.2 μm) of a multilayer stack of ilmenene sheets; (**c**) HRTEM image (scale bar of 1 nm). Interplanar spacing of 2.53 Å, corresponding to the (112–0) and (2–110) lattice spacing of the ilmenite structure signifying the (001) plane; (**d**) HRTEM image (scale bar of 10 nm) with a Fourier transform in the inset; (**e**,**f**) HRTEM image (scale bar of 2 nm) of the (001) ilmenene plane with corresponding Fourier transforms in the inset; (**g**) TEM image (scale bar of 10 nm) showing misaligned stacks of ilmenene sheets; (**h**) HRSTEM image (1 nm) showing individual constituent atoms at (001) ilmenene sheets (brown for Fe, white for Ti, and red for O); (**C**) Plausible mechanism of photocatalytic inactivation of *E. coli* On the ilmenite/persulfate (PS) composite under visible light irradiation. Adapted with permission from Ref. [267]. Copyright 2018, American Chemical Society; Adapted with permission from Ref. [271]. Copyright 2018, Elsevier B.V.

6.2. Monazite-Supported Photocatalyst

A monazite is a group of monoclinic phosphate and arsenate minerals that contains one or several kinds of rare-earth metals. Monazite (Ce), as a thorium-bearing mineral, was selected as TiO_2 substrate for its minor radioactivity and its interior framework of a composite on which TiO_2 grew by forming Ti–O–Ce microstructure [274]. TiO_2 embedded in monazite became a kind of radiation-sensitive photocatalyst, and the degradation principle was similar to photocatalysis in that the band gap of TiO_2 is activated by γ-ray irradiation. It was revealed that the radiations of thorium nuclides in TiO_2/monazite composite endowed energy to trigger TiO_2 excitation, existent cerium ions in monazite served as energy absorber with charge separator, and the TiO_2/CeO_2 structure could provide a unique electron transfer process which is beneficial to separate the charge-carriers more efficiently and thus improve catalytic activity in dark conditions. Furthermore, radioluminescence (RL) is the phenomenon by which luminescence is produced in a material by the bombardment of α-particles, γ-rays, or β-particles. It was proposed that radio-sensitive Ce could produce interior UV because of RL and TiO_2 were excited by RL. This self-activated photocatalytic behavior was similar to the heterojunction reaction mechanism and inner electric field established within TiO_2 semiconductor and CeO_2 due to Fermi level equilibrium and could transfer electron-hole pairs more effectively.

7. Summary and Outlook

To face the challenges of worldwide pollution in 21st century, scientific research and progress in photocatalysis are of great concern all over the world. The widely applied surface modification methods of bare photocatalysts are impurity doping, noble-metal deposition, heterojunction design, and mineral support combination. Among these approaches, the mineral support combination approach is widely considered to be the promising treatment to realize large-scale industrial production owing to the low cost, chemical

stability, and specific structure of natural minerals. However, due to regional limitations and wide chemical composition variations, the related research lacks systematism and the potential to pioneer further research. This review aims to sort the current research, point out the commonness of these studies, and propose all possible mineral support modification mechanisms. The proposed mineral support modification mechanisms are listed below according to different mineral groups:

As a major part of natural minerals, silicate minerals are divided into 1D, 2D, 3D, and porous minerals. Owing to their advantages in structure and adsorption capacity, silicate minerals could not only effectively suppress the self-aggregation of photocatalyst particles but also enhance the specific surface area and expose more reactive sites. Moreover, the synergistic effect between clay support and photocatalyst could efficiently promote the photo-induced charge carrier separation and hence improve the photocatalytic activity, which is ascribed to the fact that the introduction of clay mineral can enrich the pollutant concentration near the photocatalyst composite and accelerate the photogenerated electron transfer.

The presence of carbonate minerals could retard the photogenerated electron-hole pair recombination and thus reach higher photocatalytic performance. The other carbon materials can provide a stable electron reservoir and an effective electron transfer route. Therefore, they can efficiently mitigate the photogenerated electron-hole recombination with their morphology and electric conductivity.

Photocatalysts act as natural gypsum additives to endow building materials with photocatalytic activity. Under this circumstance, natural gypsum only functions as a photocatalyst substrate, making it easy to recycle, and natural pyrite belongs to the n-type semiconductor itself and could be applied as a low-cost photocatalyst after some proper treatment.

Natural ilmenite, as an anti-ferromagnetic semiconductor, is regarded as TiO_2 precursor and produces iron-doped titania or iron-oxide/titania composites with excellent photocatalytic activity by controlling treatment parameters. Due to its minor radioactivity, natural monazite as photocatalyst support enhances the photosensitivity and photocatalytic activity of composite photocatalysts.

Additionally, some active ion species sometimes exist in the natural mineral structure and therefore can act as doping species when the mineral is combined with one specific photocatalyst. Under this circumstance, the band gap structure of the photocatalyst composite can also be modified, and the photocatalyst composite could obtain a wider light absorption range and higher photocatalytic efficiency. This work intends to provide a comprehensive description of present mineral-supported photocatalytic applications and modification mechanisms based on the existing research and hopes to lay a solid foundation for future research. The combination of natural minerals and photocatalysts is believed to be the most promising method to realize the industrial production and wide applications of photocatalysis.

Last but not least, although we focus on natural minerals in this work, other mineral supports (artificial) are also worth noting. In particular, how to construct lower-cost, higher-efficiency "artificial" minerals is also a direction that can be further expanded in the future.

Author Contributions: X.L.: conceptualization, investigation, data curation, visualization, writing—original draft; U.S.: supervision, writing—review and editing; M.F.B.: supervision, writing—review and editing, project administration; A.G.: supervision, resources, writing—review and editing. All authors have read and agreed to the published version of the manuscript.

Funding: This research received no external funding.

Institutional Review Board Statement: Not applicable.

Informed Consent Statement: Not applicable.

Acknowledgments: X.L. would like to thank the China Scholarship Council for financial support.

Conflicts of Interest: The authors declare no conflicts of interest.

Abbreviation

Abbreviation	Name
OH	Hydroxide radicals
2,6-DCP	2,6-dichlorophenol
4-NP	4-nitrophenol
AS	Acidized sepiolite
ATP	Attapulgite
BF	Basalt fiber
BPA	Bisphenol A
BPB	Bromophenol blue
CB	Conduction band
CIP	Ciprofloxacin
Cit-Eu	Citrate–europium
CR	Congo red
CTC•HCl	Chlortetracycline hydrochloride
DET	Density functional theory
DRM	Dry reforming of methane
e^-	Electron
E. coli	*Escherichia coli*
EDS	Energy dispersive spectrometer
ESR	Electron spin resonance spectroscopy
EY	Eosin Y dye
FESEM	Field emission scanning electron microscope
G-MeCHO	Gaseous acetaldehyde
h^+	Hole
HCHO	Formaldehyde
HNTs	Halloysite nanotubes
IBP	Ibuprofen
IUGS	International Union of Geological Sciences
MB	Methylene blue
MBT	2-Mercaptobenzothiazole
MG	Malachite green
MMT	Montmorillonite
MO	Methyl orange
O^{2-}.	Superoxide radical
OTC	Oxytetracycline
P25	Degussa P25 TiO_2
PEG6000	Polyethylene glycol 6000
PMS	Peroxymonosulfate
PNA	Poly-naphthylamine
POPD	Poly-o-phenylenediamine
PVP	Polyvinyl pyrrolidone
RhB	Rhodamine B
S. aureus	*Staphylococcus aureus*
SDS	Sodium dodecyl sulfate
SMX	Sulfamethoxazole
TBBPA	Tetrabromobisphenol A
TC	Tetracycline
TCS	Triclosan
TH	Tetracycline hydrochloride
TMP	Trimethoprim
UV-vis DRS	UV-vis diffuse reflectance spectrophotometry
VB	Valence band
XPS	X-ray photoelectron spectroscopy

References

1. Fujishima, A.; Rao, T.N.; Tryk, D.A. Titanium dioxide photocatalysis. *J. Photochem. Photobiol. C Photochem. Rev.* **2000**, *1*, 1–21. https://doi.org/10.1016/S1389-5567(00)00002-2.
2. Lu, Y.; Zhao, K.; Zhao, Y.; Zhu, S.; Yuan, X.; Huo, M.; Zhang, Y.; Qiu, Y. Bi2WO6/TiO2/Pt nanojunction system: A UV–vis light responsive photocatalyst with high photocatalytic performance. *Colloids Surf. A Physicochem. Eng. Asp.* **2015**, *481*, 252–260. https://doi.org/10.1016/j.colsurfa.2015.05.037.
3. Rimoldi, L.; Meroni, D.; Cappelletti, G.; Ardizzone, S. Green and low cost tetracycline degradation processes by nanometric and immobilized TiO2 systems. *Catal. Today* **2017**, *281*, 38–44. https://doi.org/10.1016/j.cattod.2016.08.015.
4. Zhang, G.; Sun, Z.; Duan, Y.; Ma, R.; Zheng, S. Synthesis of nano-TiO2/diatomite composite and its photocatalytic degradation of gaseous formaldehyde. *Appl. Surf. Sci.* **2017**, *412*, 105–112. https://doi.org/10.1016/j.apsusc.2017.03.198.
5. Li, C.; Sun, Z.; Zhang, W.; Yu, C.; Zheng, S. Highly efficient g-C3N4/TiO2/kaolinite composite with novel three-dimensional structure and enhanced visible light responding ability towards ciprofloxacin and S. aureus. *Appl. Catal. B Environ.* **2018**, *220*, 272–282. https://doi.org/10.1016/j.apcatb.2017.08.044.
6. Fu, L.; Guo, Y.; Pan, S.; Huang, J.; Wang, L. Core-shell type Tourmaline@ZnO composites equipped with carbon dots for high efficiency photocatalyst. *Surf. Coat. Technol.* **2019**, *359*, 190–196. https://doi.org/10.1016/j.surfcoat.2018.12.020.
7. Nada, A.A.; Orimolade, B.O.; El-Maghrabi, H.H.; Koiki, B.A.; Rivallin, M.; Bekheet, M.F.; Viter, R.; Damberga, D.; Lesage, G.; Iatsunskyi, I.; et al. Photoelectrocatalysis of paracetamol on Pd–ZnO/ N-doped carbon nanofibers electrode. *Appl. Mater. Today* **2021**, *24*, 101129. https://doi.org/10.1016/j.apmt.2021.101129.
8. Bu, X.; Wu, B.; Long, T.; Hu, M. Preparation, characterization and enhancement of the visible-light photocatalytic activity of In2O3/rectorite composite. *J. Alloy. Compd.* **2014**, *586*, 202–207. https://doi.org/10.1016/j.jallcom.2013.10.003.
9. Li, P.; Huang, L.; Li, Y.; Xu, Y.; Huang, S.; Yuan, D.; Xu, H.; Li, H. Synthesis of dark orange montmorillonite/g-C3N4 composites and their applications in the environment. *J. Phys. Chem. Solids* **2017**, *107*, 131–139. https://doi.org/10.1016/j.jpcs.2017.03.023.
10. Liu, K.; Tong, Z.; Muhammad, Y.; Huang, G.; Zhang, H.; Wang, Z.; Zhu, Y.; Tang, R. Synthesis of sodium dodecyl sulfate modified BiOBr/magnetic bentonite photocatalyst with Three-dimensional parterre like structure for the enhanced photodegradation of tetracycline and ciprofloxacin. *Chem. Eng. J.* **2020**, *388*, 124374. https://doi.org/10.1016/j.cej.2020.124374.
11. Xu, H.-Q.; Yang, S.; Ma, X.; Huang, J.; Jiang, H.-L. Unveiling Charge-Separation Dynamics in CdS/Metal–Organic Framework Composites for Enhanced Photocatalysis. *ACS Catal.* **2018**, *8*, 11615–11621. https://doi.org/10.1021/acscatal.8b03233.
12. Fatimah, I.; Nurillahi, R.; Sahroni, I.; Muraza, O. TiO2-pillared saponite and photosensitization using a ruthenium complex for photocatalytic enhancement of the photodegradation of bromophenol blue. *Appl. Clay Sci.* **2019**, *183*, 105302. https://doi.org/10.1016/j.clay.2019.105302.
13. Kumar, S.G.; Devi, L.G. Review on modified TiO2 photocatalysis under UV/visible light: Selected results and related mechanisms on interfacial charge carrier transfer dynamics. *J. Phys. Chem. A* **2011**, *115*, 13211–13241. https://doi.org/10.1021/jp204364a.
14. Wenderich, K.; Mul, G. Methods, mechanism, and applications of photodeposition in photocatalysis: A review. *Chem. Rev.* **2016**, *116*, 14587–14619.
15. Jiang, L.; Yuan, X.; Pan, Y.; Liang, J.; Zeng, G.; Wu, Z.; Wang, H. Doping of graphitic carbon nitride for photocatalysis: A reveiw. *Appl. Catal. B Environ.* **2017**, *217*, 388–406.
16. Liu, J.; Zhang, G. Recent advances in synthesis and applications of clay-based photocatalysts: A review. *Phys. Chem. Chem. Phys.* **2014**, *16*, 8178–8192. https://doi.org/10.1039/C3CP54146K.
17. Szczepanik, B. Photocatalytic degradation of organic contaminants over clay-TiO2 nanocomposites: A review. *Appl. Clay Sci.* **2017**, *141*, 227–239. https://doi.org/10.1016/j.clay.2017.02.029.
18. Mishra, A.; Mehta, A.; Basu, S. Clay supported TiO2 nanoparticles for photocatalytic degradation of environmental pollutants: A review. *J. Environ. Chem. Eng.* **2018**, *6*, 6088–6107. https://doi.org/10.1016/j.jece.2018.09.029.
19. Serwicka, E.M. Titania-Clay Mineral Composites for Environmental Catalysis and Photocatalysis. *Catalysts* **2021**, *11*, 1087, ISBN 2073-4344.
20. Papoulis, D. Halloysite based nanocomposites and photocatalysis: A Review. *Appl. Clay Sci.* **2019**, *168*, 164–174. https://doi.org/10.1016/j.clay.2018.11.009.
21. Li, C.; Zhu, N.; Yang, S.; He, X.; Zheng, S.; Sun, Z.; Dionysiou, D.D. A review of clay based photocatalysts: Role of phyllosilicate mineral in interfacial assembly, microstructure control and performance regulation. *Chemosphere* **2021**, *273*, 129723. https://doi.org/10.1016/j.chemosphere.2021.129723.
22. Zhao, B.; Liu, L.; Cheng, H. Rational design of kaolinite-based photocatalytic materials for environment decontamination. *Appl. Clay Sci.* **2021**, *208*, 106098. https://doi.org/10.1016/j.clay.2021.106098.
23. Zou, Y.; Hu, Y.; Shen, Z.; Yao, L.; Tang, D.; Zhang, S.; Wang, S.; Hu, B.; Zhao, G.; Wang, X. Application of aluminosilicate clay mineral-based composites in photocatalysis. *J. Environ. Sci.* **2022**, *115*, 190–214. https://doi.org/10.1016/j.jes.2021.07.015.
24. Mustapha, S.; Ndamitso, M.M.; Abdulkareem, A.S.; Tijani, J.O.; Shuaib, D.T.; Ajala, A.O.; Mohammed, A.K. Application of TiO2 and ZnO nanoparticles immobilized on clay in wastewater treatment: A review. *Appl. Water Sci.* **2020**, *10*, 49. https://doi.org/10.1007/s13201-019-1138-y.
25. Tang, X.; Tang, R.; Xiong, S.; Zheng, J.; Li, L.; Zhou, Z.; Gong, D.; Deng, Y.; Su, L.; Liao, C. Application of natural minerals in photocatalytic degradation of organic pollutants: A review. *Sci. Total Environ.* **2022**, *812*, 152434. https://doi.org/10.1016/j.scitotenv.2021.152434.

26. Luo, Q.; Peng, H.; Tian, X.; Guo, J. Facile synthesis and characterization of Chrysotile/SnO 2 nanocomposite for enhanced photocatalytic properties. *Appl. Organometal Chem.* **2020**, *34*, e5356. https://doi.org/10.1002/aoc.5356.
27. Liu, Q.; Peng, H.; Tian, X.; Guo, J. Synthesis of chrysotile based nanocomposites for tuning band gap and photocatalytic property. *Appl. Clay Sci.* **2020**, *199*, 105885. https://doi.org/10.1016/j.clay.2020.105885.
28. Tang, X.; Feng, Q.; Liu, K.; Luo, X.; Huang, J.; Li, Z. A simple and innovative route to remarkably enhance the photocatalytic performance of TiO2: Using micro-meso porous silica nanofibers as carrier to support highly-dispersed TiO2 nanoparticles. *Microporous Mesoporous Mater.* **2018**, *258*, 251–261. https://doi.org/10.1016/j.micromeso.2017.09.024.
29. Shawky, A.; El-Sheikh, S.M.; Rashed, M.N.; Abdo, S.M.; El-Dosoqy, T.I. Exfoliated kaolinite nanolayers as an alternative photocatalyst with superb activity. *J. Environ. Chem. Eng.* **2019**, *7*, 103174. https://doi.org/10.1016/j.jece.2019.103174.
30. Sia, T.H.; Dai, S.; Jin, B.; Biggs, M.; Chong, M.N. Hybridising nitrogen doped titania with kaolinite: A feasible catalyst for a semi-continuous photo-degradation reactor system. *Chem. Eng. J.* **2015**, *279*, 939–947. https://doi.org/10.1016/j.cej.2015.05.101.
31. Fida, H.; Guo, S.; Zhang, G. Preparation and characterization of bifunctional Ti–Fe kaolinite composite for Cr(VI) removal. *J. Colloid Interface Sci.* **2015**, *442*, 30–38. https://doi.org/10.1016/j.jcis.2014.11.023.
32. Sun, Z.; Zhang, X.; Dong, X.; Liu, X.; Tan, Y.; Yuan, F.; Zheng, S.; Li, C. Hierarchical assembly of highly efficient visible-light-driven Ag/g-C3N4/kaolinite composite photocatalyst for the degradation of ibuprofen. *J. Mater.* **2020**, *6*, 582–592. https://doi.org/10.1016/j.jmat.2020.04.008.
33. Oliveira, C.R.S. de; Batistella, M.A.; Ulson de Souza, Antônio Augusto; Ulson de Souza, Selene Maria de Arruda Guelli. Synthesis of superacid sulfated TiO2 prepared by sol-gel method and its use as a titania precursor in obtaining a kaolinite/TiO2 nano-hybrid composite. *Powder Technol.* **2021**, *381*, 366–380. https://doi.org/10.1016/j.powtec.2020.11.063.
34. Fang, X.; Lu, G.; Mahmood, A.; Tang, Z.; Liu, Z.; Zhang, L.; Wang, Y.; Sun, J. A novel ternary Mica/TiO2/Fe2O3 composite pearlescent pigment for the photocatalytic degradation of acetaldehyde. *J. Photochem. Photobiol. A Chem.* **2020**, *400*, 112617. https://doi.org/10.1016/j.jphotochem.2020.112617.
35. Zuo, S.; Cao, X.; Wang, P.; Li, X.; Liu, W.; Xu, R.; Yao, C.; Fu, Y.; Liu, X. Synthesis of ultrathin-layered MoS2/conductive mica composites with enhanced visible photocatalytic activity. *Mater. Sci. Semicond. Processing* **2021**, *121*, 105457. https://doi.org/10.1016/j.mssp.2020.105457.
36. Touaa, N.D.; Bouberka, Z.; Gherdaoui, C.E.; Supiot, P.; Roussel, P.; Pierlot, C.; Maschke, U. Titanium and iron-modified delaminated muscovite as photocatalyst for enhanced degradation of Tetrabromobisphenol A by visible light. *Funct. Mater. Lett.* **2020**, *13*, 2051008. https://doi.org/10.1142/S179360472051008X.
37. Dong, Z.; Ling, M.; Jiang, Y.; Han, M.; Ren, G.; Zhang, J.; Ren, X.; Li, F.; Xue, B. Preparation and properties of TiO2/illite composites synthesized at different hydrothermal pH values. *Chem. Phys.* **2019**, *525*, 110394. https://doi.org/10.1016/j.chemphys.2019.110394.
38. Wang, Y.; Kong, X.; Tian, W.; Lei, D.; Lei, X. Three-dimensional potassium niobate nanoarray on vermiculite for high-performance photocatalyst fabricated by an in situ hydrothermal process. *RSC Adv.* **2016**, *6*, 58401–58408. https://doi.org/10.1039/C6RA06959B.
39. Zhu, P.; Wang, R.; Duan, M.; Chen, Y.; Hu, M.; Luo, X.; Teng, H. Efficient Adsorption and Photocatalytic Degradation of Dyes by AgI-Bi2MoO6/Vermiculite Composite under Visible Light. *ChemistrySelect* **2019**, *4*, 12022–12031. https://doi.org/10.1002/slct.201901873.
40. Sohrabnezhad, S.; Zanjanchi, M.A.; Razavi, M. Plasmon-assisted degradation of methylene blue with Ag/AgCl/montmorillonite nanocomposite under visible light. *Spectrochim. Acta Part A Mol. Biomol. Spectrosc.* **2014**, *130*, 129–135. https://doi.org/10.1016/j.saa.2014.02.188.
41. Belhouchet, N.; Hamdi, B.; Chenchouni, H.; Bessekhouad, Y. Photocatalytic degradation of tetracycline antibiotic using new calcite/titania nanocomposites. *J. Photochem. Photobiol. A Chem.* **2019**, *372*, 196–205. https://doi.org/10.1016/j.jphotochem.2018.12.016.
42. Freitas, W.A.; Soares, B.E.C.F.; Rodrigues, M.S.; Trigueiro, P.; Honorio, L.M.C.; Peña-Garcia, R.; Alcântara, A.C.S.; Silva-Filho, E.C.; Fonseca, M.G.; Furtini, M.B.; et al. Facile synthesis of ZnO-clay minerals composites using an ultrasonic approach for photocatalytic performance. *J. Photochem. Photobiol. A Chem.* **2022**, *429*, 113934. https://doi.org/10.1016/j.jphotochem.2022.113934.
43. Zhang, L.; Chuaicham, C.; Balakumar, V.; Sasaki, K. Effect of ionic Fe(III) doping on montmorillonite for photocatalytic reduction of Cr(VI) in wastewater. *J. Photochem. Photobiol. A Chem.* **2022**, *429*, 113909. https://doi.org/10.1016/j.jphotochem.2022.113909.
44. Liu, K.; Zhang, H.; Fu, T.; Wang, L.; Tang, R.; Tong, Z.; Huang, X. Construction of BiOBr/Ti3C2/exfoliated montmorillonite Schottky junction: New insights into exfoliated montmorillonite for inducing MXene oxygen functionalization and enhancing photocatalytic activity. *Chem. Eng. J.* **2022**, *438*, 135609. https://doi.org/10.1016/j.cej.2022.135609.
45. Fatimah, I.; Purwiandono, G.; Hidayat, A.; Sagadevan, S.; Kamari, A. Mechanistic insight into the adsorption and photocatalytic activity of a magnetically separable γ-Fe2O3/Montmorillonite nanocomposite for rhodamine B removal. *Chem. Phys. Lett.* **2022**, *792*, 139410. https://doi.org/10.1016/j.cplett.2022.139410.
46. Yue, Y.; Shen, S.; Cheng, W.; Han, G.; Wu, Q.; Jiang, J. Construction of mechanically robust and recyclable photocatalytic hydrogel based on nanocellulose-supported CdS/MoS2/Montmorillonite hybrid for antibiotic degradation. *Colloids Surf. A Physicochem. Eng. Asp.* **2022**, *636*, 128035. https://doi.org/10.1016/j.colsurfa.2021.128035.
47. Zhao, Y.; Cao, Z.; Chen, Y.; Jia, Y.; Wang, Q.; Cheng, H. Heterostructure coal-bearing strata kaolinite/MnFe2O4 composite for activation of peroxydisulfate to efficiently degrade chlortetracycline hydrochloride. *Colloids Surf. A Physicochem. Eng. Asp.* **2022**, *643*, 128789. https://doi.org/10.1016/j.colsurfa.2022.128789.

48. Fufa, P.A.; Feysia, G.B.; Gultom, N.S.; Kuo, D.-H.; Chen, X.; Kabtamu, D.M.; Zelekew, O.A. Visible light-driven photocatalytic activity of Cu_2O/ZnO/Kaolinite-based composite catalyst for the degradation of organic pollutant. *Nanotechnology* **2022**, *33*, 315601. https://doi.org/10.1088/1361-6528/ac69f9.
49. Golmohammadi, M.; Honarmand, M.; Esmaeili, A. Biosynthesis of ZnO nanoparticles supported on bentonite and the evaluation of its photocatalytic activity. *Mater. Res. Bull.* **2022**, *149*, 111714. https://doi.org/10.1016/j.materresbull.2021.111714.
50. Kamali, M.; Xue, Y.; Khalaj, M.; Laats, B.; Teunckens, R.; Verbist, M.; Costa, M.E.V.; Capela, I.; Appels, L.; Dewil, R. ZnO/γ-Fe2O3/Bentonite: An Efficient Solar-Light Active Magnetic Photocatalyst for the Degradation of Pharmaceutical Active Compounds. *Molecules* **2022**, *27*, 3050, ISBN 1420-3049.
51. El Gaidoumi, A.; Doña Rodríguez, J.M.; Pulido Melián, E.; González-Díaz, O.M.; Navío Santos, J.A.; El Bali, B.; Kherbeche, A. Synthesis of sol-gel pyrophyllite/TiO2 heterostructures: Effect of calcination temperature and methanol washing on photocatalytic activity. *Surf. Interfaces* **2019**, *14*, 19–25. https://doi.org/10.1016/j.surfin.2018.10.003.
52. Hao, R.; Wang, G.; Tang, H.; Sun, L.; Xu, C.; Han, D. Template-free preparation of macro/mesoporous g-C3N4/TiO2 heterojunction photocatalysts with enhanced visible light photocatalytic activity. *Appl. Catal. B Environ.* **2016**, *187*, 47–58. https://doi.org/10.1016/j.apcatb.2016.01.026.
53. Shayegan, Z.; Lee, C.-S.; Haghighat, F. TiO2 photocatalyst for removal of volatile organic compounds in gas phase – A review. *Chem. Eng. J.* **2018**, *334*, 2408–2439. https://doi.org/10.1016/j.cej.2017.09.153.
54. Nada, A.A.; Bekheet, M.F.; Viter, R.; Miele, P.; Roualdes, S.; Bechelany, M. BN/GdxTi(1-x)O(4-x)/2 nanofibers for enhanced photocatalytic hydrogen production under visible light. *Appl. Catal. B Environ.* **2019**, *251*, 76–86. https://doi.org/10.1016/j.apcatb.2019.03.043.
55. Nada, A.A.; Bekheet, M.F.; Roualdes, S.; Gurlo, A.; Ayral, A. Functionalization of MCM-41 with titanium oxynitride deposited via PECVD for enhanced removal of methylene blue. *J. Mol. Liq.* **2019**, *274*, 505–515. https://doi.org/10.1016/j.molliq.2018.10.154.
56. Nada, A.A.; El Rouby, W.M.A.; Bekheet, M.F.; Antuch, M.; Weber, M.; Miele, P.; Viter, R.; Roualdes, S.; Millet, P.; Bechelany, M. Highly textured boron/nitrogen co-doped TiO2 with honeycomb structure showing enhanced visible-light photoelectrocatalytic activity. *Appl. Surf. Sci.* **2020**, *505*, 144419. https://doi.org/10.1016/j.apsusc.2019.144419.
57. Jiang, P.; Xiang, W.; Kuang, J.; Liu, W.; Cao, W. Effect of cobalt doping on the electronic, optical and photocatalytic properties of TiO2. *Solid State Sci.* **2015**, *46*, 27–32. https://doi.org/10.1016/j.solidstatesciences.2015.05.007.
58. Jia, T.; Fu, F.; Yu, D.; Cao, J.; Sun, G. Facile synthesis and characterization of N-doped TiO2/C nanocomposites with enhanced visible-light photocatalytic performance. *Appl. Surf. Sci.* **2018**, *430*, 438–447. https://doi.org/10.1016/j.apsusc.2017.07.024.
59. Tamai, K.; Hosokawa, S.; Asakura, H.; Teramura, K.; Tanaka, T. Low-temperature NOx trapping on alkali or alkaline earth metal modified TiO2 photocatalyst. *Catal. Today* **2019**, *332*, 76–82. https://doi.org/10.1016/j.cattod.2018.07.045.
60. Ben Saber, N.; Mezni, A.; Alrooqi, A.; Altalhi, T. A review of ternary nanostructures based noble metal/semiconductor for environmental and renewable energy applications. *J. Mater. Res. Technol.* **2020**, *9*, 15233–15262. https://doi.org/10.1016/j.jmrt.2020.10.090.
61. Diak, M.; Grabowska, E.; Zaleska, A. Synthesis, characterization and photocatalytic activity of noble metal-modified TiO2 nanosheets with exposed {001} facets. *Appl. Surf. Sci.* **2015**, *347*, 275–285. https://doi.org/10.1016/j.apsusc.2015.04.103.
62. Low, J.; Cheng, B.; Yu, J. Surface modification and enhanced photocatalytic CO2 reduction performance of TiO2: A review. *Appl. Surf. Sci.* **2017**, *392*, 658–686. https://doi.org/10.1016/j.apsusc.2016.09.093.
63. El-Maghrabi, H.H.; Nada, A.A.; Roualdes, S.; Bekheet, M.F. Design of Ni/NiO–TiO2/rGO nanocomposites on carbon cloth conductors via PECVD for electrocatalytic water splitting. *Int. J. Hydrog. Energy* **2020**, *45*, 32000–32011. https://doi.org/10.1016/j.ijhydene.2020.08.259.
64. Ghorbanloo, M.; Nada, A.A.; El-Maghrabi, H.H.; Bekheet, M.F.; Riedel, W.; Djamel, B.; Viter, R.; Roualdes, S.; Soliman, F.S.; Moustafa, Y.M.; et al. Superior efficiency of BN/Ce2O3/TiO2 nanofibers for photocatalytic hydrogen generation reactions. *Appl. Surf. Sci.* **2022**, *594*, 153438. https://doi.org/10.1016/j.apsusc.2022.153438.
65. Avcıoğlu, C.; Avcıoğlu, S.; Bekheet, M.F.; Gurlo, A. Solar hydrogen generation using niobium-based photocatalysts: Design strategies, progress, and challenges. *Mater. Today Energy* **2022**, *24*, 100936. https://doi.org/10.1016/j.mtener.2021.100936.
66. Alcudia-Ramos, M.A.; Fuentez-Torres, M.O.; Ortiz-Chi, F.; Espinosa-González, C.G.; Hernández-Como, N.; García-Zaleta, D.S.; Kesarla, M.K.; Torres-Torres, J.G.; Collins-Martínez, V.; Godavarthi, S. Fabrication of g-C3N4/TiO2 heterojunction composite for enhanced photocatalytic hydrogen production. *Ceram. Int.* **2020**, *46*, 38–45. https://doi.org/10.1016/j.ceramint.2019.08.228.
67. Li, B.; Chen, X.; Zhang, T.; Jiang, S.; Zhang, G.; Wu, W.; Ma, X. Photocatalytic selective hydroxylation of phenol to dihydroxybenzene by BiOI/TiO2 p-n heterojunction photocatalysts for enhanced photocatalytic activity. *Appl. Surf. Sci.* **2018**, *439*, 1047–1056. https://doi.org/10.1016/j.apsusc.2017.12.220.
68. Carriazo, J.G.; Moreno-Forero, M.; Molina, R.A.; Moreno, S. Incorporation of titanium and titanium–iron species inside a smectite-type mineral for photocatalysis. *Appl. Clay Sci.* **2010**, *50*, 401–408.
69. Dong, G.; Zhao, L.; Wu, X.; Zhu, M.; Wang, F. Photocatalysis removing of NO based on modified carbon nitride: The effect of celestite mineral particles. *Appl. Catal. B Environ.* **2019**, *245*, 459–468.
70. Cao, Y.-C.; Fu, Z.; Wei, W.; Zou, L.; Mi, T.; He, D.; Yan, C.; Liu, X.; Zhu, Y.; Chen, L.; et al. Reduced graphene oxide supported titanium dioxide nanomaterials for the photocatalysis with long cycling life. *Appl. Surf. Sci.* **2015**, *355*, 1289–1294. https://doi.org/10.1016/j.apsusc.2015.08.036.
71. Padmanabhan, S.K.; Pal, S.; Licciulli, A. Diatomite/silver phosphate composite for efficient degradation of organic dyes under solar radiation. *Bull. Mater. Sci.* **2020**, *43*, 295. https://doi.org/10.1007/s12034-020-02269-2.

72. Zhang, L.; Zhang, J.; Zhang, W.; Liu, J.; Zhong, H.; Zhao, Y. Photocatalytic activity of attapulgite–BiOCl–TiO2 toward degradation of methyl orange under UV and visible light irradiation. *Mater. Res. Bull.* **2015**, *66*, 109–114. https://doi.org/10.1016/j.materresbull.2015.02.029.
73. Xu, Y.; Zhang, L.; Chen, J.; Fu, Y.; Li, Q.; Yin, J.; Cheng, Z.; Kan, W.; Zhao, P.; Zhong, H.; et al. Synthesis of nano-Ag-assisted attapulgite/g-C3N4 composites with superior visible light photocatalytic performance. *Mater. Chem. Phys.* **2019**, *221*, 447–456. https://doi.org/10.1016/j.matchemphys.2018.09.065.
74. Tan, Y.; Yin, C.; Zheng, S.; Di, Y.; Sun, Z.; Li, C. Design and controllable preparation of Bi2MoO6/attapulgite photocatalyst for the removal of tetracycline and formaldehyde. *Appl. Clay Sci.* **2021**, *215*, 106319. https://doi.org/10.1016/j.clay.2021.106319.
75. Zhu, Z.; Yu, Y.; Dong, H.; Liu, Z.; Li, C.; Huo, P.; Yan, Y. Intercalation Effect of Attapulgite in g-C3N4 Modified with Fe3O4 Quantum Dots to Enhance Photocatalytic Activity for Removing 2-Mercaptobenzothiazole under Visible Light. *ACS Sustain. Chem. Eng.* **2017**, *5*, 10614–10623. https://doi.org/10.1021/acssuschemeng.7b02595.
76. Zuo, S.; Chen, Y.; Liu, W.; Yao, C.; Li, X.; Li, Z.; Ni, C.; Liu, X. A facile and novel construction of attapulgite/Cu2O/Cu/g-C3N4 with enhanced photocatalytic activity for antibiotic degradation. *Ceram. Int.* **2017**, *43*, 3324–3329. https://doi.org/10.1016/j.ceramint.2016.11.173.
77. Zheng, J.; Zhu, Z.; Gao, G.; Liu, Z.; Wang, Q.; Yan, Y. Construction of spindle structured CeO2 modified with rod-like attapulgite as a high-performance photocatalyst for CO2 reduction. *Catal. Sci. Technol.* **2019**, *9*, 3788–3799. https://doi.org/10.1039/C9CY00824A.
78. Guan, J.; Wang, H.; Li, J.; Ma, C.; Huo, P. Enhanced photocatalytic reduction of CO2 by fabricating In2O3/CeO2/HATP hybrid multi-junction photocatalyst. *J. Taiwan Inst. Chem. Eng.* **2019**, *99*, 93–103. https://doi.org/10.1016/j.jtice.2019.03.007.
79. Li, X.; Zhu, W.; Lu, X.; Zuo, S.; Yao, C.; Ni, C. Integrated nanostructures of CeO2/attapulgite/g-C3N4 as efficient catalyst for photocatalytic desulfurization: Mechanism, kinetics and influencing factors. *Chem. Eng. J.* **2017**, *326*, 87–98. https://doi.org/10.1016/j.cej.2017.05.131.
80. Ma, J.; Zou, J.; Li, L.; Yao, C.; Kong, Y.; Cui, B.; Zhu, R.; Li, D. Nanocomposite of attapulgite–Ag3PO4 for Orange II photodegradation. *Appl. Catal. B Environ.* **2014**, *144*, 36–40. https://doi.org/10.1016/j.apcatb.2013.06.029.
81. Zhang, J.; Liu, X. Photocatalytic hydrogen production from water under visible light irradiation using a dye-sensitized attapulgite nanocrystal photocatalyst. *Phys. Chem. Chem. Phys.* **2014**, *16*, 8655–8660. https://doi.org/10.1039/C4CP00084F.
82. Zhang, J.; Chen, A.; Wang, L.; Li, X.'a.; Huang, W. Striving Toward Visible Light Photocatalytic Water Splitting Based on Natural Silicate Clay Mineral: The Interface Modification of Attapulgite at the Atomic-Molecular Level. *ACS Sustain. Chem. Eng.* **2016**, *4*, 4601–4607. https://doi.org/10.1021/acssuschemeng.6b00716.
83. Yang, Y.; Liu, R.; Zhang, G.; Gao, L.; Zhang, W. Preparation and photocatalytic properties of visible light driven Ag–AgCl–TiO2/palygorskite composite. *J. Alloy. Compd.* **2016**, *657*, 801–808. https://doi.org/10.1016/j.jallcom.2015.10.078.
84. Bouna, L.; Rhouta, B.; Amjoud, M.; Maury, F.; Lafont, M.-C.; Jada, A.; Senocq, F.; Daoudi, L. Synthesis, characterization and photocatalytic activity of TiO2 supported natural palygorskite microfibers. *Appl. Clay Sci.* **2011**, *52*, 301–311. https://doi.org/10.1016/j.clay.2011.03.009.
85. Stathatos, E.; Papoulis, D.; Aggelopoulos, C.A.; Panagiotaras, D.; Nikolopoulou, A. TiO2/palygorskite composite nanocrystalline films prepared by surfactant templating route: Synergistic effect to the photocatalytic degradation of an azo-dye in water. *J. Hazard. Mater.* **2012**, *211-212*, 68–76. https://doi.org/10.1016/j.jhazmat.2011.11.055.
86. Kuang, M.; Zhang, J.; Wang, W.; Chen, J.; Cao, Y.; Wang, J.; Ji, Z. Ternary Ag-deposited TiO2/palygorskite composites with synergistic effect for enhanced photocatalytic activity. *Solid State Sci.* **2019**, *97*, 106015. https://doi.org/10.1016/j.solidstatesciences.2019.106015.
87. Zhang, J.; Gao, N.; Chen, F.; Zhang, T.; Zhang, G.; Wang, D.; Xie, X.; Cai, D.; Ma, X.; Wu, L.; et al. Improvement of Cr (VI) photoreduction under visible-light by g-C3N4 modified by nano-network structured palygorskite. *Chem. Eng. J.* **2019**, *358*, 398–407. https://doi.org/10.1016/j.cej.2018.10.083.
88. Luo, Y.; Zhang, M.; Yin, H.; Yao, J.; Chen, S.-m.; Liu, X. One pot controllable synthesis of palygorskite/bismuth oxyiodide hierarchical microspheres for improved visible-light photocatalytic performance. *Colloids Surf. A Physicochem. Eng. Asp.* **2019**, *578*, 123573. https://doi.org/10.1016/j.colsurfa.2019.06.038.
89. He, C.; Li, X.; Chen, X.; Ma, S.; Yan, X.; Zhang, Y.; Zuo, S.; Yao, C. Palygorskite supported rare earth fluoride for photocatalytic nitrogen fixation under full spectrum. *Appl. Clay Sci.* **2020**, *184*, 105398. https://doi.org/10.1016/j.clay.2019.105398.
90. Yuan, Z.; Lan, Y.; Chen, S.; Chen, D. Preparation of magnetically recyclable palygorskite Fe-octacarboxylic acid phthalocyanine nano-composites and their photocatalytic behavior for degradation of Rhodamine B. *Appl. Clay Sci.* **2017**, *147*, 153–159. https://doi.org/10.1016/j.clay.2017.07.029.
91. Zhang, X.; Jin, Z.; Li, Y.; Li, S.; Lu, G. Photosensitized reduction of water to hydrogen using novel Maya blue-like organic–inorganic hybrid material. *J. Colloid Interface Sci.* **2009**, *333*, 285–293. https://doi.org/10.1016/j.jcis.2009.01.013.
92. Jiang, L.; Huang, Y.; Liu, T. Enhanced visible-light photocatalytic performance of electrospun carbon-doped TiO2/halloysite nanotube hybrid nanofibers. *J. Colloid Interface Sci.* **2015**, *439*, 62–68. https://doi.org/10.1016/j.jcis.2014.10.026.
93. Wang, R.; Jiang, G.; Ding, Y.; Wang, Y.; Sun, X.; Wang, X.; Chen, W. Photocatalytic Activity of Heterostructures Based on TiO2 and Halloysite Nanotubes. *ACS Appl. Mater. Interfaces* **2011**, *3*, 4154–4158. https://doi.org/10.1021/am201020q.
94. Yu, X.; Lu, Z.; Si, N.; Zhou, W.; Chen, T.; Gao, X.; Song, M.; Yan, Y.; Huo, P.; Yan, C. Preparation of rare earth metal ion/TiO2Halconducting polymers by ions imprinting technique and its photodegradation property on tetracycline. *Appl. Clay Sci.* **2014**, *99*, 125–130. https://doi.org/10.1016/j.clay.2014.06.021.

95. Szczepanik, B.; Rogala, P.; Słomkiewicz, P.M.; Banaś, D.; Kubala-Kukuś, A.; Stabrawa, I. Synthesis, characterization and photocatalytic activity of TiO2-halloysite and Fe2O3-halloysite nanocomposites for photodegradation of chloroanilines in water. *Appl. Clay Sci.* **2017**, *149*, 118–126. https://doi.org/10.1016/j.clay.2017.08.016.
96. Papoulis, D.; Komarneni, S.; Panagiotaras, D.; Stathatos, E.; Toli, D.; Christoforidis, K.C.; Fernández-García, M.; Li, H.; Yin, S.; Sato, T.; et al. Halloysite–TiO2 nanocomposites: Synthesis, characterization and photocatalytic activity. *Appl. Catal. B Environ.* **2013**, *132-133*, 416–422. https://doi.org/10.1016/j.apcatb.2012.12.012.
97. Hojamberdiev, M.; Khan, M.M.; Kadirova, Z.; Kawashima, K.; Yubuta, K.; Teshima, K.; Riedel, R.; Hasegawa, M. Synergistic effect of g-C3N4, Ni(OH)2 and halloysite in nanocomposite photocatalyst on efficient photocatalytic hydrogen generation. *Renew. Energy* **2019**, *138*, 434–444. https://doi.org/10.1016/j.renene.2019.01.103.
98. Wu, D.; Li, J.; Guan, J.; Liu, C.; Zhao, X.; Zhu, Z.; Ma, C.; Huo, P.; Li, C.; Yan, Y. Improved photoelectric performance via fabricated heterojunction g-C3N4/TiO2/HNTs loaded photocatalysts for photodegradation of ciprofloxacin. *J. Ind. Eng. Chem.* **2018**, *64*, 206–218. https://doi.org/10.1016/j.jiec.2018.03.017.
99. Gao, X.; Tang, F.; Jin, Z. Pt–Cu Bimetallic Nanoparticles Loaded in the Lumen of Halloysite Nanotubes. *Langmuir* **2019**, *35*, 14651–14658. https://doi.org/10.1021/acs.langmuir.9b02645.
100. Das, S.; Samanta, A.; Jana, S. Light-Assisted Synthesis of Hierarchical Flower-Like MnO2 Nanocomposites with Solar Light Induced Enhanced Photocatalytic Activity. *ACS Sustain. Chem. Eng.* **2017**, *5*, 9086–9094. https://doi.org/10.1021/acssuschemeng.7b02003.
101. Xu, J.; Zhang, B.; Jia, L.; Bi, N.; Zhao, T. Metal-enhanced fluorescence detection and degradation of tetracycline by silver nanoparticle-encapsulated halloysite nano-lumen. *J. Hazard. Mater.* **2020**, *386*, 121630. https://doi.org/10.1016/j.jhazmat.2019.121630.
102. Bielska, D.; Karewicz, A.; Lachowicz, T.; Berent, K.; Szczubiałka, K.; Nowakowska, M. Hybrid photosensitizer based on halloysite nanotubes for phenol-based pesticide photodegradation. *Chem. Eng. J.* **2015**, *262*, 125–132. https://doi.org/10.1016/j.cej.2014.09.081.
103. Li, F.; Dai, Y.; Gong, M.; Yu, T.; Chen, X. Synthesis, characterization of magnetic-sepiolite supported with TiO2, and the photocatalytic performance over Cr(VI) and 2,4-dichlorophenol co-existed wastewater. *J. Alloy. Compd.* **2015**, *638*, 435–442. https://doi.org/10.1016/j.jallcom.2015.03.070.
104. Karamanis, D.; Ökte, A.N.; Vardoulakis, E.; Vaimakis, T. Water vapor adsorption and photocatalytic pollutant degradation with TiO2–sepiolite nanocomposites. *Appl. Clay Sci.* **2011**, *53*, 181–187. https://doi.org/10.1016/j.clay.2010.12.012.
105. Papoulis, D.; Somalakidi, K.; Todorova, N.; Trapalis, C.; Panagiotaras, D.; Sygkridou, D.; Stathatos, E.; Gianni, E.; Mavrikos, A.; Komarneni, S. Sepiolite/TiO2 and metal ion modified sepiolite/TiO2 nanocomposites: Synthesis, characterization and photocatalytic activity in abatement of NOx gases. *Appl. Clay Sci.* **2019**, *179*, 105156. https://doi.org/10.1016/j.clay.2019.105156.
106. Hu, X.; Li, C.; Sun, Z.; Song, J.; Zheng, S. Enhanced photocatalytic removal of indoor formaldehyde by ternary heterogeneous BiOCl/TiO2/sepiolite composite under solar and visible light. *Build. Environ.* **2020**, *168*, 106481. https://doi.org/10.1016/j.buildenv.2019.106481.
107. Wang, Y.; Yang, Q.; Wang, X.; Yang, J.; Dai, Y.; He, Y.; Chen, W.; Zhang, W. Photocatalytic degradation of rhodamin B and diclofenac sodium on hollow hierarchical microspheres of BiOBr modified with sepiolite and polyvinyl pyrrolidone (PVP). *Mater. Sci. Eng. B* **2019**, *244*, 12–22. https://doi.org/10.1016/j.mseb.2019.04.005.
108. Wang, P.; Qi, C.; Hao, L.; Wen, P.; Xu, X. Sepiolite/Cu2O/Cu photocatalyst: Preparation and high performance for degradation of organic dye. *J. Mater. Sci. Technol.* **2019**, *35*, 285–291. https://doi.org/10.1016/j.jmst.2018.03.023.
109. Akkari, M.; Aranda, P.; Belver, C.; Bedia, J.; Ben Haj Amara, A.; Ruiz-Hitzky, E. Reprint of ZnO/sepiolite heterostructured materials for solar photocatalytic degradation of pharmaceuticals in wastewater. *Appl. Clay Sci.* **2018**, *160*, 3–8. https://doi.org/10.1016/j.clay.2018.02.027.
110. Akkari, M.; Aranda, P.; Mayoral, A.; García-Hernández, M.; Ben Haj Amara, A.; Ruiz-Hitzky, E. Sepiolite nanoplatform for the simultaneous assembly of magnetite and zinc oxide nanoparticles as photocatalyst for improving removal of organic pollutants. *J. Hazard. Mater.* **2017**, *340*, 281–290. https://doi.org/10.1016/j.jhazmat.2017.06.067.
111. Chuaicham, C.; Pawar, R.; Sasaki, K. Dye-sensitized Photocatalyst of Sepiolite for Organic Dye Degradation. *Catalysts* **2019**, *9*, 235, ISBN 2073-4344.
112. Paineau, E. Imogolite Nanotubes: A Flexible Nanoplatform with Multipurpose Applications. *Appl. Sci.* **2018**, *8*, 1921, ISBN 2076-3417.
113. Bottero, I.; Bonelli, B.; Ashbrook, S.E.; Wright, P.A.; Zhou, W.; Tagliabue, M.; Armandi, M.; Garrone, E. Synthesis and characterization of hybrid organic/inorganic nanotubes of the imogolite type and their behaviour towards methane adsorption. *Phys. Chem. Chem. Phys.* **2011**, *13*, 744–750. https://doi.org/10.1039/C0CP00438C.
114. Bahadori, E.; Vaiano, V.; Esposito, S.; Armandi, M.; Sannino, D.; Bonelli, B. Photo-activated degradation of tartrazine by H2O2 as catalyzed by both bare and Fe-doped methyl-imogolite nanotubes. *Catal. Today* **2018**, *304*, 199–207. https://doi.org/10.1016/j.cattod.2017.08.003.
115. Olson, N.; Deshpande, N.; Gunduz, S.; Ozkan, U.S.; Brunelli, N.A. Utilizing imogolite nanotubes as a tunable catalytic material for the selective isomerization of glucose to fructose. *Catal. Today* **2019**, *323*, 69–75. https://doi.org/10.1016/j.cattod.2018.07.059.
116. Kuroda, Y.; Fukumoto, K.; Kuroda, K. Uniform and high dispersion of gold nanoparticles on imogolite nanotubes and assembly into morphologically controlled materials. *Appl. Clay Sci.* **2012**, *55*, 10–17. https://doi.org/10.1016/j.clay.2011.07.004.

117. Katsumata, K.-I.; Hou, X.; Sakai, M.; Nakajima, A.; Fujishima, A.; Matsushita, N.; MacKenzie, K.J.D.; Okada, K. Visible-light-driven photodegradation of acetaldehyde gas catalyzed by aluminosilicate nanotubes and Cu(II)-grafted TiO2 composites. *Appl. Catal. B Environ.* **2013**, *138-139*, 243–252. https://doi.org/10.1016/j.apcatb.2013.03.004.
118. Yao, G.; Sun, Z.; Zheng, S. Synthesis and enhanced visible-light photocatalytic activity of wollastonite/g-C3N4 composite. *Mater. Res. Bull.* **2017**, *86*, 186–193. https://doi.org/10.1016/j.materresbull.2016.10.028.
119. Ren, S.; Zhao, X.; Zhao, L.; Yuan, M.; Yu, Y.; Guo, Y.; Wang, Z. Preparation of porous TiO2/silica composites without any surfactants. *J. Solid State Chem.* **2009**, *182*, 312–316. https://doi.org/10.1016/j.jssc.2008.10.027.
120. Hou, X.; Zhang, Y.; Ding, H.; Chu, P.K. Environmentally friendly wollastonite@TiO2 composite particles prepared by a mechano-chemical method. *Particuology* **2018**, *40*, 105–112. https://doi.org/10.1016/j.partic.2017.10.010.
121. Kwak, B.S.; Kim, K.M.; Park, S.-M.; Kang, M. Synthesis of basalt fiber@Zn1-xMgxO core/shell nanostructures for selective photoreduction of CO2 to CO. *Appl. Surf. Sci.* **2017**, *407*, 109–116. https://doi.org/10.1016/j.apsusc.2017.02.178.
122. Rakitskaya, T.L.; Kiose, T.A.; Oleksenko, L.P.; Lutsenko, L.V.; Dlubovskii, R.M.; Volkova, V.J. Influence of water content in the Pd(II)-Cu(II) catalyst fixed on acid-modified basalt tuff on its activity in the carbon monoxide oxidation by oxygen. *Russ. J. Appl. Chem.* **2012**, *85*, 1339–1344. https://doi.org/10.1134/S1070427212090078.
123. Qiu, L.; Chu, Z.; Yang, S.; Chen, Y.; Song, L.; Du, P.; Xiong, J. Microwave Hydrothermal Synthesis of Basalt Fibers/Titanium Dioxide and Their Photocatalytic Activity for the Degradation of Rhodamine B. *J. Nanosci. Nanotechnol.* **2019**, *19*, 5723–5728. https://doi.org/10.1166/jnn.2019.16557.
124. Do, J.Y.; Im, Y.; Kwak, B.S.; Park, S.-M.; Kang, M. Preparation of basalt fiber@perovskite $PbTiO_3$ core–shell composites and their effects on CH_4 production from CO_2 photoreduction. *Ceram. Int.* **2016**, *42*, 5942–5951. https://doi.org/10.1016/j.ceramint.2015.12.142.
125. Jun Wang; Xiaoping Liang; Peng Chen; Di Zhang; Shanmin Yang; Zhifeng Liu. Microstructure and photocatalytic properties of Ag/Ce4+/La3+ co-modified TiO_2/Basalt fiber for ammonianitrogen removal from synthetic wastewater. *J. Sol-Gel Sci. Technol.* **2016**, *82*, 289–298.
126. Yu, L.; Wang, C.; Chen, F.; Zhang, J.; Ruan, Y.; Xu, J. Investigating the synergistic effects in tourmaline/TiO2-based heterogeneous photocatalysis: Underlying mechanism insights. *J. Mol. Catal. A Chem.* **2016**, *411*, 1–8. https://doi.org/10.1016/j.molcata.2015.10.006.
127. Zhang, G.; Qin, X. Efficient photocatalytic degradation of gaseous formaldehyde by the TiO_2/tourmaline composites. *Mater. Res. Bull.* **2013**, *48*, 3743–3749. https://doi.org/10.1016/j.materresbull.2013.05.112.
128. Tzeng, J.-H.; Weng, C.-H.; Lin, Y.-H.; Huang, S.-M.; Yen, L.-T.; Anotai, J.; Lin, Y.-T. Synthesis, characterization, and visible light induced photoactivity of tourmaline-N-TiO2 composite for photooxidation of ethylene. *J. Ind. Eng. Chem.* **2019**, *80*, 376–384. https://doi.org/10.1016/j.jiec.2019.08.017.
129. Baeissa, E.S. Green synthesis of methanol by photocatalytic reduction of CO_2 under visible light using a graphene and tourmaline co-doped titania nanocomposites. *Ceram. Int.* **2014**, *40*, 12431–12438.
130. Li, Y.; Xing, X.; Pei, J.; Li, R.; Wen, Y.; Cui, S.; Liu, T. Automobile exhaust gas purification material based on physical adsorption of tourmaline powder and visible light catalytic decomposition of g-C3N4/BiVO4. *Ceram. Int.* **2020**, *46*, 12637–12647. https://doi.org/10.1016/j.ceramint.2020.02.029.
131. Bian, X.; Chen, J.; Ji, R. Degradation of methyl blue using Fe-tourmaline as a novel photocatalyst. *Molecules* **2013**, *18*, 1457–1463. https://doi.org/10.3390/molecules18021457.
132. Tang, X.; Feng, Q.; Liu, K.; Tan, Y. Synthesis and characterization of a novel nanofibrous TiO_2/SiO_2 composite with enhanced photocatalytic activity. *Mater. Lett.* **2016**, *183*, 175–178.
133. Zhang, H.; Duan, T.; Zhu, W.; Yao, W.-T. Natural Chrysotile-Based Nanowires Decorated with Monodispersed Ag Nanoparticles as a Highly Active and Reusable Hydrogenation Catalyst. *J. Phys. Chem. C* **2015**, *119*, 21465–21472. https://doi.org/10.1021/acs.jpcc.5b05450.
134. Lou, J.P.; Xue, G.X.; Li, S.Z.; Wang, J. Particle Coating of Talc with TiO_2: Synthesis, Characterization and Photo Catalytic Degradation of Methylene Blue. *Adv. Mater. Res.* **2013**, *781-784*, 157–162. https://doi.org/10.4028/www.scientific.net/AMR.781-784.157.
135. Ai, M.; Qin, W.; Xia, T.; Ye, Y.; Chen, X.; Zhang, P.; Justin Thomas, K.R. Photocatalytic Degradation of 2,4-Dichlorophenol by TiO_2 Intercalated Talc Nanocomposite. *Int. J. Photoenergy* **2019**, *2019*, 1540271. https://doi.org/10.1155/2019/1540271.
136. Wang, Q.; Rhimi, B.; Wang, H.; Wang, C. Efficient photocatalytic degradation of gaseous toluene over F-doped TiO2/exfoliated bentonite. *Appl. Surf. Sci.* **2020**, *530*, 147286. https://doi.org/10.1016/j.apsusc.2020.147286.
137. Krishnan, B.; Mahalingam, S. Ag/TiO2/bentonite nanocomposite for biological applications: Synthesis, characterization, antibacterial and cytotoxic investigations. *Adv. Powder Technol.* **2017**, *28*, 2265–2280. https://doi.org/10.1016/j.apt.2017.06.007.
138. Li, J.; Suyoulema; Wang, W.; Sarina. A study of photodegradation of sulforhodamine B on Au–TiO_2/bentonite under UV and visible light irradiation. *Solid State Sci.* **2009**, *11*, 2037–2043. https://doi.org/10.1016/j.solidstatesciences.2009.09.012.
139. WANG, S.-q.; LI, J.-m.; LIU, W.-b. Effect of F, V and Mn co-doping on the catalytic performance of TiO_2-pillared bentonite in the photocatalytic denitration. *J. Fuel Chem. Technol.* **2020**, *48*, 1131–1139. https://doi.org/10.1016/S1872-5813(20)30076-1.
140. Mishra, A.; Mehta, A.; Kainth, S.; Basu, S. Effect of g-C3N4 loading on TiO_2/Bentonite nanocomposites for efficient heterogeneous photocatalytic degradation of industrial dye under visible light. *J. Alloy. Compd.* **2018**, *764*, 406–415. https://doi.org/10.1016/j.jallcom.2018.06.089.

141. Yang, S.; Liang, G.; Gu, A.; Mao, H. Synthesis of TiO2 pillared montmorillonite with ordered interlayer mesoporous structure and high photocatalytic activity by an intra-gallery templating method. *Mater. Res. Bull.* **2013**, *48*, 3948–3954. https://doi.org/10.1016/j.materresbull.2013.06.019.
142. Tahir, M.; Amin, N.S. Photocatalytic reduction of carbon dioxide with water vapors over montmorillonite modified TiO_2 nanocomposites. *Appl. Catal. B Environ.* **2013**, *142-143*, 512–522. https://doi.org/10.1016/j.apcatb.2013.05.054.
143. Tahir, M.; Tahir, B.; Zakaria, Z.Y.; Muhammad, A. Enhanced photocatalytic carbon dioxide reforming of methane to fuels over nickel and montmorillonite supported TiO_2 nanocomposite under UV-light using monolith photoreactor. *J. Clean. Prod.* **2019**, *213*, 451–461. https://doi.org/10.1016/j.jclepro.2018.12.169.
144. Umer, M.; Tahir, M.; Azam, M.U.; Tahir, B.; Jaffar, M.M.; Alias, H. Montmorillonite dispersed single wall carbon nanotubes (SWCNTs)/TiO_2 heterojunction composite for enhanced dynamic photocatalytic H2 production under visible light. *Appl. Clay Sci.* **2019**, *174*, 110–119. https://doi.org/10.1016/j.clay.2019.03.029.
145. Yang, L.; Ma, X.; Zhang, W.; Gen, W. Ag@AgCl-TiO_2/organic rectorite/quaternized chitosan microspheres: An efficient and environmental photocatalyst. *J. Appl. Polym. Sci.* **2017**, *134*. https://doi.org/10.1002/app.44601.
146. Yang, Y.; Zhang, G.; Xu, W. Facile synthesis and photocatalytic properties of AgAgClTiO_2/rectorite composite. *J. Colloid Interface Sci.* **2012**, *376*, 217–223. https://doi.org/10.1016/j.jcis.2012.03.003.
147. Zhang, Y.; Deng, L.; Zhang, G.; Gan, H. Facile synthesis and photocatalytic property of bicrystalline TiO_2/rectorite composites. *Colloids Surf. A Physicochem. Eng. Asp.* **2011**, *384*, 137–144. https://doi.org/10.1016/j.colsurfa.2011.03.043.
148. Zhang, Y.; Miao, B.; Chen, Q.; Bai, Z.; Cao, Y.; Davaa, B. Synthesis, Structure, and Photocatalytic Activity of TiO_2-Montmorillonite Composites. *Catalysts* **2022**, *12*, 486, ISBN 2073-4344.
149. Cardona, Y.; Węgrzyn, A.; Miśkowiec, P.; Korili, S.A.; Gil, A. Catalytic photodegradation of organic compounds using TiO_2/pillared clays synthesized using a nonconventional aluminum source. *Chem. Eng. J.* **2022**, *446*, 136908. https://doi.org/10.1016/j.cej.2022.136908.
150. Hu, X.; Song, J.; Zheng, S.; Sun, Z.; Li, C. Insight into the defective sites of TiO_2/sepiolite composite on formaldehyde removal and H2 evolution. *Mater. Today Energy* **2022**, *24*, 100932. https://doi.org/10.1016/j.mtener.2021.100932.
151. Hu, X.; Li, C.; Song, J.; Zheng, S.; Sun, Z. Hierarchical assembly of visible-light-driven Bi2MoO6/TiO2/sepiolite composite for effective formaldehyde removal. *Appl. Clay Sci.* **2022**, *227*, 106590. https://doi.org/10.1016/j.clay.2022.106590.
152. Dlamini, M.C.; Dlamini, M.L.; Mente, P.; Tlhaole, B.; Erasmus, R.; Maubane-Nkadimeng, M.S.; Moma, J.A. Photocatalytic abatement of phenol on amorphous TiO2-BiOBr-bentonite heterostructures under visible light irradiation. *J. Ind. Eng. Chem.* **2022**, *111*, 419–436. https://doi.org/10.1016/j.jiec.2022.04.023.
153. Venu Sreekala, S.; Vayalveettil, A.; Kazhuthuttil Kochu, J.; Thoppil Ramakrishnan, R.; Puthenveedu Sadasivan Pillai, H. Bentonite-titanium dioxide functional nanocomposites suitable for wastewater treatment: an integrated photocatalyst-adsorbent system. *N. J. Chem.* **2022**, *46*, 4772–4783. https://doi.org/10.1039/D1NJ05472D.
154. Ardani, M.; Imani, M.; Tadjarodi, A. Core shell Fe3O4@TiO2/silica aerogel nanocomposite; synthesis and study of structural, magnetic and photocatalytic properties. *Microporous Mesoporous Mater.* **2022**, *338*, 111757. https://doi.org/10.1016/j.micromeso.2022.111757.
155. Ma, J.; Liu, Q.; Zhu, L.; Zou, J.; Wang, K.; Yang, M.; Komarneni, S. Visible light photocatalytic activity enhancement of Ag3PO4 dispersed on exfoliated bentonite for degradation of rhodamine B. *Appl. Catal. B Environ.* **2016**, *182*, 26–32. https://doi.org/10.1016/j.apcatb.2015.09.004.
156. Nguyen, D.B.; Nguyen, T.D.C.; Dao, T.P.; Tran, H.T.; van Nguyen, N.; Ahn, D.H. Preparation, characterization and evaluation of catalytic activity of titania modified with silver and bentonite. *J. Ind. Eng. Chem.* **2012**, *18*, 1764–1767. https://doi.org/10.1016/j.jiec.2012.04.004.
157. Ma, J.; Huang, D.; Zhang, W.; Zou, J.; Kong, Y.; Zhu, J.; Komarneni, S. Nanocomposite of exfoliated bentonite/g-C3N4/Ag3PO4 for enhanced visible-light photocatalytic decomposition of Rhodamine B. *Chemosphere* **2016**, *162*, 269–276. https://doi.org/10.1016/j.chemosphere.2016.07.089.
158. Thiruppathi, M.; Selvakumar, K.; Arunpandian, M.; Thirumalai, K.; Ramalingan, C.; Swaminathan, M.; Nagarajan, E.R. An affordable photocatalyst for pharmaceuticals and superior electrocatalyst for methanol oxidation—A dual role by CuWO4 anchored bentonite clay. *Colloids Surf. A Physicochem. Eng. Asp.* **2019**, *563*, 148–159. https://doi.org/10.1016/j.colsurfa.2018.12.006.
159. Tahir, B.; Tahir, M.; Mohd Nawawi, M.G. Well-Designed 3D/2D/2D WO3/Bt/g-C3N4 Z-Scheme Heterojunction for Tailoring Photocatalytic CO2 Methanation with 2D-Layered Bentonite-Clay as the Electron Moderator under Visible Light. *Energy Fuels* **2020**, *34*, 14400–14418. https://doi.org/10.1021/acs.energyfuels.0c02637.
160. Riaz, U.; Ashraf, S.M.; Ruhela, A. Catalytic degradation of orange G under microwave irradiation with a novel nanohybrid catalyst. *J. Environ. Chem. Eng.* **2015**, *3*, 20–29. https://doi.org/10.1016/j.jece.2014.06.010.
161. Bentouami, A.; Ouali, M.S.; Menorval, L.-C. de. Photocatalytic decolourization of indigo carmine on 1,10-phenanthrolinium intercalated bentonite under UV-B and solar irradiation. *J. Photochem. Photobiol. A Chem.* **2010**, *212*, 101–106. https://doi.org/10.1016/j.jphotochem.2010.04.002.
162. Huang, S.; Lu, X.; Li, Z.; Ravishankar, H.; Wang, J.; Wang, X. A biomimetic approach towards the synthesis of TiO_2/carbon-clay as a highly recoverable photocatalyst. *J. Photochem. Photobiol. A Chem.* **2018**, *351*, 131–138. https://doi.org/10.1016/j.jphotochem.2017.10.017.
163. Peng, K.; Fu, L.; Ouyang, J.; Yang, H. Emerging Parallel Dual 2D Composites: Natural Clay Mineral Hybridizing MoS 2 and Interfacial Structure. *Adv. Funct. Mater.* **2016**, *26*, 2666–2675. https://doi.org/10.1002/adfm.201504942.

164. Obalová, L.; Šihor, M.; Praus, P.; Reli, M.; Kočí, K. Photocatalytic and photochemical decomposition of N2O on ZnS-MMT catalyst. *Catal. Today* **2014**, *230*, 61–66. https://doi.org/10.1016/j.cattod.2013.09.047.
165. Gu, N.; Gao, J.; Li, H.; Wu, Y.; Ma, Y.; Wang, K. Montmorillonite-supported with Cu_2O nanoparticles for damage and removal of Microcystis aeruginosa under visible light. *Appl. Clay Sci.* **2016**, *132-133*, 79–89. https://doi.org/10.1016/j.clay.2016.05.017.
166. Zhang, C.; Yu, Y.; Wei, H.; Li, K. In situ growth of cube-like AgCl on montmorillonite as an efficient photocatalyst for dye (Acid Red 18) degradation. *Appl. Surf. Sci.* **2018**, *456*, 577–585. https://doi.org/10.1016/j.apsusc.2018.06.009.
167. Xu, J.; Qi, Y.; Wang, W.; Wang, L. Montmorillonite-hybridized g-C3N4 composite modified by NiCoP cocatalyst for efficient visible-light-driven photocatalytic hydrogen evolution by dye-sensitization. *Int. J. Hydrog. Energy* **2019**, *44*, 4114–4122. https://doi.org/10.1016/j.ijhydene.2018.12.167.
168. Pastorková, K.; Jesenák, K.; Kadlečíková, M.; Breza, J.; Kolmačka, M.; Čaplovičová, M.; Lazišťan, F.; Michalka, M. The growth of multi-walled carbon nanotubes on natural clay minerals (kaolinite, nontronite and sepiolite). *Appl. Surf. Sci.* **2012**, *258*, 2661–2666. https://doi.org/10.1016/j.apsusc.2011.10.114.
169. Liu, X.; Dong, H.; Zeng, Q.; Yang, X.; Zhang, D. Synergistic Effects of Reduced Nontronite and Organic Ligands on Cr(VI) Reduction. *Environ. Sci. Technol.* **2019**, *53*, 13732–13741. https://doi.org/10.1021/acs.est.9b04769.
170. Xia, Q.; Wang, X.; Zeng, Q.; Guo, D.; Zhu, Z.; Chen, H.; Dong, H. Mechanisms of Enhanced Antibacterial Activity by Reduced Chitosan-Intercalated Nontronite. *Environ. Sci. Technol.* **2020**, *54*, 5207–5217. https://doi.org/10.1021/acs.est.9b07185.
171. Li, S.-Q.; Zhou, P.-J.; Zhang, W.-S.; Chen, S.; Peng, H. Effective photocatalytic decolorization of methylene blue utilizing ZnO/rectorite nanocomposite under simulated solar irradiation. *J. Alloy. Compd.* **2014**, *616*, 227–234. https://doi.org/10.1016/j.jallcom.2014.07.102.
172. Wu, S.; Fang, J.; Xu, W.; Cen, C. Bismuth-modified rectorite with high visible light photocatalytic activity. *J. Mol. Catal. A Chem.* **2013**, *373*, 114–120. https://doi.org/10.1016/j.molcata.2013.03.012.
173. Guo, Y.; Yu, W.; Chen, J.; Wang, X.; Gao, B.; Wang, G. Ag_3PO_4/rectorite nanocomposites: Ultrasound-assisted preparation, characterization and enhancement of stability and visible-light photocatalytic activity. *Ultrason. Sonochemistry* **2017**, *34*, 831–838. https://doi.org/10.1016/j.ultsonch.2016.07.017.
174. Naing, H.H.; Wang, K.; Tun, P.P.; Zhang, G. Enhanced broad spectrum (vis-NIR) responsive photocatalytic performance of Ag2O/rectorite nanoarchitectures. *Appl. Surf. Sci.* **2019**, *491*, 216–224. https://doi.org/10.1016/j.apsusc.2019.06.079.
175. Chen, Y.; Fang, J.; Lu, S.; Wu, Y.; Chen, D.; Huang, L.; Xu, W.; Zhu, X.; Fang, Z. Fabrication, characterization and photocatalytic properties of Ag/AgI/BiOI heteronanostructures supported on rectorite via a cation-exchange method. *Mater. Res. Bull.* **2015**, *64*, 97–105. https://doi.org/10.1016/j.materresbull.2014.12.040.
176. Bu, X.; Wang, Y.; Li, J.; Zhang, C. Improving the visible light photocatalytic activity of TiO_2 by combining sulfur doping and rectorite carrier. *J. Alloy. Compd.* **2015**, *628*, 20–26. https://doi.org/10.1016/j.jallcom.2014.12.171.
177. Zhao, X.; Zhu, L.; Zhang, Y.; Yan, J.; Lu, X.; Huang, Y.; Tang, H. Removing organic contaminants with bifunctional iron modified rectorite as efficient adsorbent and visible light photo-Fenton catalyst. *J. Hazard. Mater.* **2012**, *215–216*, 57–64. https://doi.org/10.1016/j.jhazmat.2012.02.030.
178. Guo, S.; Yang, W.; You, L.; Li, J.; Chen, J.; Zhou, K. Simultaneous reduction of Cr(VI) and degradation of tetracycline hydrochloride by a novel iron-modified rectorite composite through heterogeneous photo-Fenton processes. *Chem. Eng. J.* **2020**, *393*, 124758. https://doi.org/10.1016/j.cej.2020.124758.
179. Nikolopoulou, A.; Papoulis, D.; Komarneni, S.; Tsolis-Katagas, P.; Panagiotaras, D.; Kacandes, G.H.; Zhang, P.; Yin, S.; Sato, T. Solvothermal preparation of TiO2/saponite nanocomposites and photocatalytic activity. *Appl. Clay Sci.* **2009**, *46*, 363–368. https://doi.org/10.1016/j.clay.2009.09.007.
180. David, C.; Arivazhagan, M.; Ibrahim, M. Spent wash decolourization using nano-Al_2O_3/kaolin photocatalyst: Taguchi and ANN approach. *J. Saudi Chem. Soc.* **2015**, *19*, 537–548. https://doi.org/10.1016/j.jscs.2015.05.012.
181. Kočí, K.; Matějka, V.; Kovář, P.; Lacný, Z.; Obalová, L. Comparison of the pure TiO_2 and kaolinite/TiO_2 composite as catalyst for CO2 photocatalytic reduction. *Catal. Today* **2011**, *161*, 105–109. https://doi.org/10.1016/j.cattod.2010.08.026.
182. Li, C.; Dong, X.; Zhu, N.; Zhang, X.; Yang, S.; Sun, Z.; Liu, Y.; Zheng, S.; Dionysiou, D.D. Rational design of efficient visible-light driven photocatalyst through 0D/2D structural assembly: Natural kaolinite supported monodispersed TiO_2 with carbon regulation. *Chem. Eng. J.* **2020**, *396*, 125311. https://doi.org/10.1016/j.cej.2020.125311.
183. Zhang, Z.; Lu, L.; Lv, Z.; Chen, Y.; Jin, H.; Hou, S.; Qiu, L.; Duan, L.; Liu, J.; Dai, K. Porous carbon nitride with defect mediated interfacial oxidation for improving visible light photocatalytic hydrogen evolution. *Appl. Catal. B Environ.* **2018**, *232*, 384–390. https://doi.org/10.1016/j.apcatb.2018.03.086.
184. Jiang, D.; Liu, Z.; Fu, L.; Yang, H. Interfacial Chemical-Bond-Modulated Charge Transfer of Heterostructures for Improving Photocatalytic Performance. *ACS Appl. Mater. Interfaces* **2020**, *12*, 9872–9880. https://doi.org/10.1021/acsami.9b17183.
185. Xue, B.; Yang, K.; Wang, X.; Chi, Q.; Jiang, Y. The role of potassium chlorate on expansion of dickite layers and the preparation of a novel TiO2 impregnated dickite photocatalyst using expanded dickite as carrier. *RSC Adv.* **2016**, *6*, 9803–9811. https://doi.org/10.1039/C5RA23615K.
186. Wang, N.; Zhao, Z.; Liu, L.; Xing, J. Preparation of muscovite/tungsten-doped TiO_2 composites for the efficient photocatalytic degradation of methyl orange under simulated solar light irradiation. *Inorg. Chem. Commun.* **2022**, *138*, 109285, doi:10.1016/j.inoche.2022.109285.

187. Shimizu, K.-i.; Murayama, H.; Nagai, A.; Shimada, A.; Hatamachi, T.; Kodama, T.; Kitayama, Y. Degradation of hydrophobic organic pollutants by titania pillared fluorine mica as a substrate specific photocatalyst. *Appl. Catal. B Environ.* **2005**, *55*, 141–148. https://doi.org/10.1016/j.apcatb.2004.08.005.
188. Fang, X.; Lu, G.; Mahmood, A.; Wang, Y.; Wang, X.; Xie, X.; Tang, Z.; Sun, J. A novel ternary mica-titania@rGO composite pearlescent pigment for the photocatalytic degradation of gaseous acetaldehyde. *Chem. Eng. J.* **2020**, *396*, 125312. https://doi.org/10.1016/j.cej.2020.125312.
189. Zhou, S.; Lv, J.; Guo, L.K.; Xu, G.Q.; Wang, D.M.; Zheng, Z.X.; Wu, Y.C. Preparation and photocatalytic properties of N-doped nano-TiO2/muscovite composites. *Appl. Surf. Sci.* **2012**, *258*, 6136–6141. https://doi.org/10.1016/j.apsusc.2012.03.018.
190. Li, Y.; Sun, H.; Peng, T.; You, H.; Qin, Y.; Zeng, L. Effects of muscovite matrix on photocatalytic degradation in TiO2/muscovite nanocomposites. *Appl. Clay Sci.* **2019**, *179*, 105155. https://doi.org/10.1016/j.clay.2019.105155.
191. Senthilnathan, A.; Dissanayake, D.M.S.N.; Chandrakumara, G.T.D.; Mantilaka, M.M.M.G.P.G.; Rajapakse, R.M.G.; Pitawala, H.M.T.G.A.; Nalin de Silva, K.M. Akaganeite nanorices deposited muscovite mica surfaces as sunlight active green photocatalyst. *R. Soc. Open Sci.* **2019**, *6*, 182212. https://doi.org/10.1098/rsos.182212.
192. Peng, F.; Ni, Y.; Zhou, Q.; Kou, J.; Lu, C.; Xu, Z. New g-C3N4 based photocatalytic cement with enhanced visible-light photocatalytic activity by constructing muscovite sheet/SnO2 structures. *Constr. Build. Mater.* **2018**, *179*, 315–325. https://doi.org/10.1016/j.conbuildmat.2018.05.146.
193. Bao, T.; Damtie, M.M.; Hosseinzadeh, A.; Frost, R.L.; Yu, Z.M.; Jin, J.; Wu, K. Catalytic degradation of P-chlorophenol by muscovite-supported nano zero valent iron composite: Synthesis, characterization, and mechanism studies. *Appl. Clay Sci.* **2020**, *195*, 105735. https://doi.org/10.1016/j.clay.2020.105735.
194. Mantilaka, M.; Senthilnathan, A.; Ekanayake, U.M.; Dissanayake, D. In-Situ Synthesis of Zinc Oxide Nano-Seeds on Muscovite Mica Sheets as A Highly Active Photocatalyst. *J. Nanosci. Res.* **2020**, *1*, 5–14.
195. Sun, Z.; Li, C.; Du, X.; Zheng, S.; Wang, G. Facile synthesis of two clay minerals supported graphitic carbon nitride composites as highly efficient visible-light-driven photocatalysts. *J. Colloid Interface Sci.* **2018**, *511*, 268–276. https://doi.org/10.1016/j.jcis.2017.10.005.
196. Akri, M.; Pronier, S.; Chafik, T.; Achak, O.; Granger, P.; Simon, P.; Trentesaux, M.; Batiot-Dupeyrat, C. Development of nickel supported La and Ce-natural illite clay for autothermal dry reforming of methane: Toward a better resistance to deactivation. *Appl. Catal. B Environ.* **2017**, *205*, 519–531. https://doi.org/10.1016/j.apcatb.2016.12.050.
197. Akri, M.; Chafik, T.; Granger, P.; Ayrault, P.; Batiot-Dupeyrat, C. Novel nickel promoted illite clay based catalyst for autothermal dry reforming of methane. *Fuel* **2016**, *178*, 139–147. https://doi.org/10.1016/j.fuel.2016.03.018.
198. Gili, A.; Schlicker, L.; Bekheet, M.F.; Görke, O.; Penner, S.; Grünbacher, M.; Götsch, T.; Littlewood, P.; Marks, T.J.; Stair, P.C.; et al. Surface Carbon as a Reactive Intermediate in Dry Reforming of Methane to Syngas on a 5% Ni/MnO Catalyst. *ACS Catal.* **2018**, *8*, 8739–8750. https://doi.org/10.1021/acscatal.8b01820.
199. Dong, X.; Duan, X.; Sun, Z.; Zhang, X.; Li, C.; Yang, S.; Ren, B.; Zheng, S.; Dionysiou, D.D. Natural illite-based ultrafine cobalt oxide with abundant oxygen-vacancies for highly efficient Fenton-like catalysis. *Appl. Catal. B Environ.* **2020**, *261*, 118214. https://doi.org/10.1016/j.apcatb.2019.118214.
200. Zhao, X.; Li, J.; Zhang, Y.; Dong, H.; Qu, J.; Qi, T. Preparation of nanosized anatase TiO2-coated illite composite pigments by Ti(SO4)2 hydrolysis. *Powder Technol.* **2015**, *271*, 262–269. https://doi.org/10.1016/j.powtec.2014.10.021.
201. Li, X.; Dong, G.; Guo, F.; Zhu, P.; Huang, Y.; Wang, C. Enhancement of photocatalytic NO removal activity of g-C3N4 by modification with illite particles. *Environ. Sci. Nano* **2020**, *7*, 1990–1998. https://doi.org/10.1039/D0EN00415D.
202. Zhang, J.; Zhu, W.; Liu, X. Stable hydrogen generation from vermiculite sensitized by CdS quantum dot photocatalytic splitting of water under visible-light irradiation. *Dalton Trans.* **2014**, *43*, 9296–9302. https://doi.org/10.1039/C4DT00897A.
203. Martínez-Costa, J.I.; Rivera-Utrilla, J.; Leyva-Ramos, R.; Sánchez-Polo, M.; Velo-Gala, I. Individual and simultaneous degradation of antibiotics sulfamethoxazole and trimethoprim by UV and solar radiation in aqueous solution using bentonite and vermiculite as photocatalysts. *Appl. Clay Sci.* **2018**, *160*, 217–225. https://doi.org/10.1016/j.clay.2017.12.026.
204. Hojamberdiev, M.; Katsumata, K.-i.; Matsushita, N.; Okada, K. Preparation of Bi2WO6– and BiOI–allophane composites for efficient photodegradation of gaseous acetaldehyde under visible light. *Appl. Clay Sci.* **2014**, *101*, 38–43. https://doi.org/10.1016/j.clay.2014.07.007.
205. Nishikiori, H.; Furuichi, N.; Teshima, K.; Yamashita, H. Reaction Kinetics on Allophane–Titania Nanocomposite Electrodes for Photofuel Cells. *Chem. Lett.* **2017**, *46*, 659–661. https://doi.org/10.1246/cl.170064.
206. Nishikiori, H.; Furukawa, M.; Fujii, T. Degradation of trichloroethylene using highly adsorptive allophane–TiO2 nanocomposite. *Appl. Catal. B Environ.* **2011**, *102*, 470–474. https://doi.org/10.1016/j.apcatb.2010.12.028.
207. Ono, Y.; Katsumata, K.-I. Enhanced photocatalytic activity of titanium dioxide/allophane mixed powder by acid treatment. *Appl. Clay Sci.* **2014**, *90*, 61–66. https://doi.org/10.1016/j.clay.2013.12.018.
208. Hojamberdiev, M.; Kadirova, Z.C.; Makinose, Y.; Zhu, G.; Emin, S.; Matsushita, N.; Hasegawa, M.; Okada, K. Involving CeVO4 in improving the photocatalytic activity of a Bi2WO6/allophane composite for the degradation of gaseous acetaldehyde under visible light. *Colloids Surf. A Physicochem. Eng. Asp.* **2017**, *529*, 600–612. https://doi.org/10.1016/j.colsurfa.2017.06.047.
209. El Gaidoumi, A.; Doña-Rodríguez, J.M.; Pulido Melián, E.; González-Díaz, O.M.; El Bali, B.; Navío, J.A.; Kherbeche, A. Mesoporous pyrophyllite–titania nanocomposites: Synthesis and activity in phenol photocatalytic degradation. *Res. Chem. Intermed.* **2019**, *45*, 333–353. https://doi.org/10.1007/s11164-018-3605-8.

210. El Gaidoumi, A.; Doña-Rodríguez, J.M.; Pulido Melián, E.; González-Díaz, O.M.; Navío, J.A.; El Bali, B.; Kherbeche, A. Catalytic Efficiency of Cu-Supported Pyrophyllite in Heterogeneous Catalytic Oxidation of Phenol. *Arab. J. Sci. Eng.* **2019**, *44*, 6313–6325. https://doi.org/10.1007/s13369-019-03757-2.
211. Rabbani, M.; Haghverdi, M.; Heidari-Golafzani, M.; Rahimi, R.; Javaheri Kachousangi, M. Preparation of a new adsorbent expanded perlite@ZnO@reduced graphene oxide for the synergistic photocatalytic–adsorption removal of organic pollutants. *N. J. Chem.* **2017**, *41*, 8011–8015. https://doi.org/10.1039/C7NJ00482F.
212. Długosz, M.; Waś, J.; Szczubiałka, K.; Nowakowska, M. TiO2-coated EP as a floating photocatalyst for water purification. *J. Mater. Chem. A* **2014**, *2*, 6931–6938. https://doi.org/10.1039/C3TA14951J.
213. Xue, H.; Jiang, Y.; Yuan, K.; Yang, T.; Hou, J.; Cao, C.; Feng, K.; Wang, X. Floating photocatalyst of B–N–TiO2/expanded perlite: A sol–gel synthesis with optimized mesoporous and high photocatalytic activity. *Sci. Rep.* **2016**, *6*, 29902. https://doi.org/10.1038/srep29902.
214. Song, J.; Wang, X.; Ma, J.; Wang, X.; Wang, J.; Zhao, J. Visible-light-driven in situ inactivation of Microcystis aeruginosa with the use of floating g-C3N4 heterojunction photocatalyst: Performance, mechanisms and implications. *Appl. Catal. B Environ.* **2018**, *226*, 83–92. https://doi.org/10.1016/j.apcatb.2017.12.034.
215. Khan, U.A.; Liu, J.; Pan, J.; Ma, H.; Zuo, S.; Yu, Y.; Ahmad, A.; Iqbal, M.; Ullah, S.; Li, B. One-Pot Fabrication of Hierarchical Floating Bi–Bi2S3–Bi2WO6/Expanded Perlite Photocatalysts for Efficient Photocatalysis of Organic Contaminants Utilized Sun-like Illumination. *Ind. Eng. Chem. Res.* **2019**, *58*, 9286–9299. https://doi.org/10.1021/acs.iecr.9b01067.
216. Darkhosh, F.; Lashanizadegan, M.; Mahjoub, A.R.; Cheshme Khavar, A.H. One pot synthesis of CuFeO2 @ expanding perlite as a novel efficient floating catalyst for rapid degradation of methylene blue under visible light illumination. *Solid State Sci.* **2019**, *91*, 61–72. https://doi.org/10.1016/j.solidstatesciences.2019.03.009.
217. Qiu, H.; Hu, J.; Zhang, R.; Gong, W.; Yu, Y.; Gao, H. The photocatalytic degradation of diesel by solar light-driven floating BiOI/EP composites. *Colloids Surf. A Physicochem. Eng. Asp.* **2019**, *583*, 123996. https://doi.org/10.1016/j.colsurfa.2019.123996.
218. Eddy, D.R.; Puri, F.N.; Noviyanti, A.R. Synthesis and Photocatalytic Activity of Silica-based Sand Quartz as the Supporting TiO2 Photocatalyst. *Procedia Chem.* **2015**, *17*, 55–58. https://doi.org/10.1016/j.proche.2015.12.132.
219. Okemoto, A.; Kishishita, K.; Maeda, S.; Gohda, S.; Misaki, M.; Koshiba, Y.; Ishida, K.; Horie, T.; Taniya, K.; Ichihashi, Y.; et al. Application of picene thin-film semiconductor as a photocatalyst for photocatalytic hydrogen formation from water. *Appl. Catal. B Environ.* **2016**, *192*, 88–92. https://doi.org/10.1016/j.apcatb.2016.03.028.
220. Misawa, K.; Sekine, Y.; Kusukubo, Y.; Sohara, K. Photocatalytic degradation of atmospheric fine particulate matter (PM2.5) collected on TiO2 supporting quartz fibre filter. *Environ. Technol.* **2020**, *41*, 1266–1274. https://doi.org/10.1080/09593330.2018.1530696.
221. Zhang, W.; Liu, Y.; Li, C. Photocatalytic degradation of ofloxacin on Gd2Ti2O7 supported on quartz spheres. *J. Phys. Chem. Solids* **2018**, *118*, 144–149. https://doi.org/10.1016/j.jpcs.2018.03.019.
222. Li, R.; Wang, X.; Jin, S.; Zhou, X.; Feng, Z.; Li, Z.; Shi, J.; Zhang, Q.; Li, C. Photo-induced H2 production from a CH3OH-H2O solution at insulator surface. *Sci. Rep.* **2015**, *5*, 13475. https://doi.org/10.1038/srep13475.
223. Zhang, W.; Tao, Y.; Li, C. Sol-gel synthesize and characterization of χGd2Ti2O7/SiO2 photocatalyst for ofloxacin decomposition. *Mater. Res. Bull.* **2018**, *105*, 55–62. https://doi.org/10.1016/j.materresbull.2018.04.032.
224. Li, D.; Zhu, Q.; Han, C.; Yang, Y.; Jiang, W.; Zhang, Z. Photocatalytic degradation of recalcitrant organic pollutants in water using a novel cylindrical multi-column photoreactor packed with TiO2-coated silica gel beads. *J. Hazard. Mater.* **2015**, *285*, 398–408. https://doi.org/10.1016/j.jhazmat.2014.12.024.
225. Ismail, N.; Othman, M.H.; Kamaludin, R.; Esham, M.; Ali, N.; Rahman, M.; Jaafar, J.; Bakar, S. Characterization of Bauxite as a Potential Natural Photocatalyst for Photodegradation of Textile Dye. *Arab. J. Sci. Eng.* **2019**, *44*, 10031–10040. https://doi.org/10.1007/s13369-019-04029-9.
226. Du, Y.; Wang, X.; Wu, J.; Qi, C.; Li, Y. Adsorption and photoreduction of Cr(VI) via diatomite modified by Nb2O5 nanorods. *Particuology* **2018**, *40*, 123–130. https://doi.org/10.1016/j.partic.2017.11.005.
227. Padmanabhan, S.K.; Pal, S.; Ul Haq, E.; Licciulli, A. Nanocrystalline TiO2–diatomite composite catalysts: Effect of crystallization on the photocatalytic degradation of rhodamine B. *Appl. Catal. A Gen.* **2014**, *485*, 157–162. https://doi.org/10.1016/j.apcata.2014.08.002.
228. Xia, Y.; Li, F.; Jiang, Y.; Xia, M.; Xue, B.; Li, Y. Interface actions between TiO2 and porous diatomite on the structure and photocatalytic activity of TiO2-diatomite. *Appl. Surf. Sci.* **2014**, *303*, 290–296. https://doi.org/10.1016/j.apsusc.2014.02.169.
229. Zhang, G.; Peyravi, A.; Hashisho, Z.; Sun, Z.; Liu, Y.; Zheng, S.; Zhong, L. Integrated adsorption and photocatalytic degradation of VOCs using a TiO2/diatomite composite: Effects of relative humidity and reaction atmosphere. *Catal. Sci. Technol.* **2020**, *10*, 2378–2388. https://doi.org/10.1039/D0CY00168F.
230. Wu, Z.; Zhu, Z.; Hao, X.; Zhou, W.; Han, J.; Tang, X.; Yao, S.; Zhang, X. Enhanced oxidation of naphthalene using plasma activation of TiO2/diatomite catalyst. *J. Hazard. Mater.* **2018**, *347*, 48–57. https://doi.org/10.1016/j.jhazmat.2017.12.052.
231. Barbosa, I.A.; Zanatta, L.D.; Espimpolo, D.M.; da Silva, D.L.; Nascimento, L.F.; Zanardi, F.B.; Sousa Filho, P.C. de; Serra, O.A.; Iamamoto, Y. Magnetic diatomite(Kieselguhr)/Fe2O3/TiO2 composite as an efficient photo-Fenton system for dye degradation. *Solid State Sci.* **2017**, *72*, 14–20. https://doi.org/10.1016/j.solidstatesciences.2017.08.007.
232. He, H.; Luo, Z.; Yu, C. Diatomite-anchored g-C3N4 nanosheets for selective removal of organic dyes. *J. Alloy. Compd.* **2020**, *816*, 152652. https://doi.org/10.1016/j.jallcom.2019.152652.

233. Liu, G.; Abukhadra, M.R.; El-Sherbeeny, A.M.; Mostafa, A.M.; Elmeligy, M.A. Insight into the photocatalytic properties of diatomite@Ni/NiO composite for effective photo-degradation of malachite green dye and photo-reduction of Cr (VI) under visible light. *J. Environ. Manag.* **2020**, *254*, 109799. https://doi.org/10.1016/j.jenvman.2019.109799.
234. Tajmiri, S.; Hosseini, M.R.; Azimi, E. Combined photocatalytic-adsorptive removal of water contaminants using a biologically prepared CdS-diatomite nanocomposite. *Mater. Chem. Phys.* **2021**, *258*, 123913. https://doi.org/10.1016/j.matchemphys.2020.123913.
235. Hua, C.; Liu, X.; Ren, S.; Zhang, C.; Liu, W. Preparation of visible light-responsive photocatalytic paper containing BiVO4@diatomite/MCC/PVBCFs for degradation of organic pollutants. *Ecotoxicol. Environ. Saf.* **2020**, *202*, 110897. https://doi.org/10.1016/j.ecoenv.2020.110897.
236. Liu, M.Y.; Zheng, L.; Lin, G.L.; Ni, L.F.; Song, X.C. Synthesis and photocatalytic activity of BiOCl/diatomite composite photocatalysts: Natural porous diatomite as photocatalyst support and dominant facets regulator. *Adv. Powder Technol.* **2020**, *31*, 339–350. https://doi.org/10.1016/j.apt.2019.10.026.
237. Jia, Z.; Li, T.; Zheng, Z.; Zhang, J.; Liu, J.; Li, R.; Wang, Y.; Zhang, X.; Wang, Y.; Fan, C. The BiOCl/diatomite composites for rapid photocatalytic degradation of ciprofloxacin: Efficiency, toxicity evaluation, mechanisms and pathways. *Chem. Eng. J.* **2020**, *380*, 122422. https://doi.org/10.1016/j.cej.2019.122422.
238. Xiong, C.; Ren, Q.; Liu, X.; Jin, Z.; Ding, Y.; Zhu, H.; Li, J.; Chen, R. Fenton activity on RhB degradation of magnetic g-C3N4/diatomite/Fe3O4 composites. *Appl. Surf. Sci.* **2021**, *543*, 148844. https://doi.org/10.1016/j.apsusc.2020.148844.
239. Xiong, C.; Ren, Q.; Chen, S.; Liu, X.; Jin, Z.; Ding, Y. A multifunctional Ag3PO4/Fe3O4/Diatomite composites: Photocatalysis, adsorption and sterilization. *Mater. Today Commun.* **2021**, *28*, 102695. https://doi.org/10.1016/j.mtcomm.2021.102695.
240. Yang, B.; Ma, Z.; Wang, Q.; Yang, J. Synthesis and Photoelectrocatalytic Applications of TiO2/ZnO/Diatomite Composites. *Catalysts* **2022**, *12*, 268, ISBN 2073-4344.
241. Yuan, F.; Yang, R.; Li, C.; Zhang, X.; Sun, Z. Enhanced visible-light properties of TiO2/diatomite composite over varied bismuth semiconductors modification for formaldehyde photodegradation: A comparative study. *Sep. Purif. Technol.* **2022**, *297*, 121477. https://doi.org/10.1016/j.seppur.2022.121477.
242. Xue, L.; Liang, E.; Wang, J. Fabrication of magnetic ZnO/ZnFe2O4/diatomite composites: Improved photocatalytic efficiency under visible light irradiation. *J. Mater. Sci. Mater. Electron.* **2022**, *33*, 1405–1424. https://doi.org/10.1007/s10854-021-07568-w.
243. Zhang, X.; Duan, J.; Tan, Y.; Deng, Y.; Li, C.; Sun, Z. Insight into peroxymonosulfate assisted photocatalysis over Fe2O3 modified TiO2/diatomite composite for highly efficient removal of ciprofloxacin. *Sep. Purif. Technol.* **2022**, *293*, 121123. https://doi.org/10.1016/j.seppur.2022.121123.
244. Zhang, Y.; Chen, X.; Cui, M.-S.; Guo, Z.; Chen, Y.-H.; Cui, K.-P.; Ding, Z.-G.; Weerasooriya, R. Binding Fe-doped g-C3N4 on the porous diatomite for efficient degradation of tetracycline via photo-Fenton process. *J. Environ. Chem. Eng.* **2022**, *10*, 107406. https://doi.org/10.1016/j.jece.2022.107406.
245. Jiang, Z.; Zhu, H.; Guo, W.; Ren, Q.; Ding, Y.; Chen, S.; Chen, J.; Jia, X. Ag3VO4/g-C3N4/diatomite ternary compound reduces Cr(vi) ion in aqueous solution effectively under visible light. *RSC Adv.* **2022**, *12*, 7671–7679. https://doi.org/10.1039/D1RA09295B.
246. Zhang, X.; Shen, J.; Sun, H.; Gong, Y.; Zhang, S. Room Temperature Oxidation of Formaldehyde Using TiO2/Recycled Diatomite Composite. *JOM* **2022**, *74*, 2716–2723. https://doi.org/10.1007/s11837-022-05224-0.
247. Nezamzadeh-Ejhieh, A.; Amiri, M. CuO supported Clinoptilolite towards solar photocatalytic degradation of p-aminophenol. *Powder Technol.* **2013**, *235*, 279–288. https://doi.org/10.1016/j.powtec.2012.10.017.
248. Nassar, M.Y.; Abdelrahman, E.A. Hydrothermal tuning of the morphology and crystallite size of zeolite nanostructures for simultaneous adsorption and photocatalytic degradation of methylene blue dye. *J. Mol. Liq.* **2017**, *242*, 364–374. https://doi.org/10.1016/j.molliq.2017.07.033.
249. Takeuchi, M.; Hidaka, M.; Anpo, M. Efficient removal of toluene and benzene in gas phase by the TiO2/Y-zeolite hybrid photocatalyst. *J. Hazard. Mater.* **2012**, *237-238*, 133–139. https://doi.org/10.1016/j.jhazmat.2012.08.011.
250. Kovalevskiy, N.S.; Lyulyukin, M.N.; Selishchev, D.S.; Kozlov, D.V. Analysis of air photocatalytic purification using a total hazard index: Effect of the composite TiO2/zeolite photocatalyst. *J. Hazard. Mater.* **2018**, *358*, 302–309. https://doi.org/10.1016/j.jhazmat.2018.06.035.
251. Rahmani-Aliabadi, A.; Nezamzadeh-Ejhieh, A. A visible light FeS/Fe2S3/zeolite photocatalyst towards photodegradation of ciprofloxacin. *J. Photochem. Photobiol. A Chem.* **2018**, *357*, 1–10. https://doi.org/10.1016/j.jphotochem.2018.02.006.
252. Rajabi, S.K.; Sohrabnezhad, S. Synthesis and characterization of magnetic core with two shells: Mordenite zeolite and CuO to form Fe3O4@MOR@CuO core-shell: As a visible light driven photocatalyst. *Microporous Mesoporous Mater.* **2017**, *242*, 136–143. https://doi.org/10.1016/j.micromeso.2017.01.024.
253. Yusuff, A.S.; Taofeek Popoola, L.; Aderibigbe, E.I. Solar photocatalytic degradation of organic pollutants in textile industry wastewater by ZnO/pumice composite photocatalyst. *J. Environ. Chem. Eng.* **2020**, *8*, 103907. https://doi.org/10.1016/j.jece.2020.103907.
254. Taheri-Ledari, R.; Valadi, K.; Gharibi, S.; Maleki, A. Synergistic photocatalytic effect between green LED light and Fe3O4/ZnO-modified natural pumice: A novel cleaner product for degradation of methylene blue. *Mater. Res. Bull.* **2020**, *130*, 110946. https://doi.org/10.1016/j.materresbull.2020.110946.
255. Colangiuli, D.; Lettieri, M.; Masieri, M.; Calia, A. Field study in an urban environment of simultaneous self-cleaning and hydrophobic nanosized TiO2-based coatings on stone for the protection of building surface. *Sci. Total Environ.* **2019**, *650*, 2919–2930. https://doi.org/10.1016/j.scitotenv.2018.10.044.

256. Fadhilah, N.; Etruly, N.; Muharja, M.; Sawitri, D. Self-Cleaning Limestone Paint Modified by Nanoparticles TiO_2 Synthesized from TiCl3 as Precursors and PEG6000 as Dispersant. *Bull. Chem. React. Eng. Catal.* **2017**, *12*. https://doi.org/10.9767/bcrec.12.3.800.351-356.
257. Mostafa, M.M.; El saied, M.; Morshedy, A.S. Novel Calcium Carbonate-titania nanocomposites for enhanced sun light photo catalytic desulfurization process. *J. Environ. Manag.* **2019**, *250*, 109462. https://doi.org/10.1016/j.jenvman.2019.109462.
258. Belarbi, I.; Çoruh, A.; Hamacha, R.; Marouf-Khelifa, K.; Khelifa, A. Development and characterization of a new dolomite-based catalyst: Application to the photocatalytic degradation of pentachlorophenol. *Water Sci. Technol.* **2019**, *79*, 741–752. https://doi.org/10.2166/wst.2019.094.
259. Yi, H.; Huang, D.; Qin, L.; Zeng, G.; Lai, C.; Cheng, M.; Ye, S.; Song, B.; Ren, X.; Guo, X. Selective prepared carbon nanomaterials for advanced photocatalytic application in environmental pollutant treatment and hydrogen production. *Appl. Catal. B Environ.* **2018**, *239*, 408–424. https://doi.org/10.1016/j.apcatb.2018.07.068.
260. Xu, Y.-J.; Zhuang, Y.; Fu, X. New Insight for Enhanced Photocatalytic Activity of TiO_2 by Doping Carbon Nanotubes: A Case Study on Degradation of Benzene and Methyl Orange. *J. Phys. Chem. C* **2010**, *114*, 2669–2676. https://doi.org/10.1021/jp909855p.
261. Gnayem, H.; Uvarov, V.; Lahad, O.; Sasson, Y. Hybrid bismuth oxyhalides@gypsum as self-cleaning composites: Novel aspects of a sustainable photocatalytic technology for solar environmental cleanup. *RSC Adv.* **2015**, *5*, 66650–66656. https://doi.org/10.1039/C5RA09993E.
262. Janus, M.; Zatorska, J.; Zając, K.; Kusiak-Nejman, E.; Czyżewski, A.; Morawski, A.W. The mechanical and photocatalytic properties of modified gypsum materials. *Mater. Sci. Eng. B* **2018**, *236*, 1–9. https://doi.org/10.1016/j.mseb.2018.11.015.
263. Binas, V.; Papadaki, D.; Maggos, T.; Katsanaki, A.; Kiriakidis, G. Study of innovative photocatalytic cement based coatings: The effect of supporting materials. *Constr. Build. Mater.* **2018**, *168*, 923–930. https://doi.org/10.1016/j.conbuildmat.2018.02.106.
264. Diao, Z.-H.; Xu, X.-R.; Liu, F.-M.; Sun, Y.-X.; Zhang, Z.-W.; Sun, K.-F.; Wang, S.-Z.; Cheng, H. Photocatalytic degradation of malachite green by pyrite and its synergism with Cr(VI) reduction: Performance and reaction mechanism. *Sep. Purif. Technol.* **2015**, *154*, 168–175. https://doi.org/10.1016/j.seppur.2015.09.027.
265. Kalantary, R.R.; Moradi, M.; Pirsaheb, M.; Esrafili, A.; Jafari, A.J.; Gholami, M.; Vasseghian, Y.; Antolini, E.; Dragoi, E.-N. Enhanced photocatalytic inactivation of E. coli by natural pyrite in presence of citrate and EDTA as effective chelating agents: Experimental evaluation and kinetic and ANN models. *J. Environ. Chem. Eng.* **2019**, *7*, 102906. https://doi.org/10.1016/j.jece.2019.102906.
266. Guo, Q.; Tang, G.; Zhu, W.; Luo, Y.; Gao, X. In situ construction of Z-scheme FeS_2/Fe_2O_3 photocatalyst via structural transformation of pyrite for photocatalytic degradation of carbamazepine and the synergistic reduction of Cr(VI). *J. Environ. Sci.* **2021**, *101*, 351–360. https://doi.org/10.1016/j.jes.2020.08.029.
267. Puthirath Balan, A.; Radhakrishnan, S.; Kumar, R.; Neupane, R.; Sinha, S.K.; Deng, L.; los Reyes, C.A. de; Apte, A.; Rao, B.M.; Paulose, M.; et al. A Non-van der Waals Two-Dimensional Material from Natural Titanium Mineral Ore Ilmenite. *Chem. Mater.* **2018**, *30*, 5923–5931. https://doi.org/10.1021/acs.chemmater.8b01935.
268. Simpraditpan, A.; Wirunmongkol, T.; Pavasupree, S.; Pecharapa, W. Effect of calcination temperature on structural and photocatalyst properties of nanofibers prepared from low-cost natural ilmenite mineral by simple hydrothermal method. *Mater. Res. Bull.* **2013**, *48*, 3211–3217. https://doi.org/10.1016/j.materresbull.2013.04.083.
269. Shao, S.; Yu, J.; Love, J.B.; Fan, X. An economic approach to produce iron doped TiO_2 nanorods from ilmenite for photocatalytic applications. *J. Alloy. Compd.* **2021**, *858*, 158388. https://doi.org/10.1016/j.jallcom.2020.158388.
270. Hong, T.; Mao, J.; Tao, F.; Lan, M. Recyclable Magnetic Titania Nanocomposite from Ilmenite with Enhanced Photocatalytic Activity. *Molecules* **2017**, *22*. https://doi.org/10.3390/molecules22122044.
271. Xia, D.; He, H.; Liu, H.; Wang, Y.; Zhang, Q.; Li, Y.; Lu, A.; He, C.; Wong, P.K. Persulfate-mediated catalytic and photocatalytic bacterial inactivation by magnetic natural ilmenite. *Appl. Catal. B Environ.* **2018**, *238*, 70–81. https://doi.org/10.1016/j.apcatb.2018.07.003.
272. Lee, R.B.; Lee, K.M.; Lai, C.W.; Pan, G.-T.; Yang, T.C.K.; Juan, J.C. The relationship between iron and Ilmenite for photocatalyst degradation. *Adv. Powder Technol.* **2018**, *29*, 1779–1786. https://doi.org/10.1016/j.apt.2018.04.013.
273. Zazo, J.A.; García-Muñoz, P.; Pliego, G.; Silveira, J.E.; Jaffe, P.; Casas, J.A. Selective reduction of nitrate to N2 using ilmenite as a low cost photo-catalyst. *Appl. Catal. B Environ.* **2020**, *273*, 118930. https://doi.org/10.1016/j.apcatb.2020.118930.
274. Yu, C.; Wang, C.-F.; Chen, T.; Chang, Y. Synthesis and characterization of radiation sensitive TiO_2/monazite photocatalyst. *J. Radioanal. Nucl. Chem.* **2008**, *277*, 337–345. https://doi.org/10.1007/s10967-007-7099-x.